Muon-spin relaxation and its application in the study of molecular quantum magnets

Johannes S. Möller
Merton College, University of Oxford

A thesis submitted for the Degree of
Doctor of Philosophy in Condensed Matter Physics

Trinity Term 2013

Abstract

Muon-spin relaxation and its application in the study of molecular quantum magnets

Johannes S. Möller, Merton College, University of Oxford

A thesis submitted for the Degree of Doctor of Philosophy in Condensed Matter Physics, Trinity Term 2013

This thesis is concerned with the muon-spin relaxation (μ^+SR) technique and its application in the study of a number of molecular magnetic systems that may be driven through a quantum phase transition at low temperatures through the application of a magnetic field or hydrostatic pressure.

μ^+SR is a highly sensitive probe of magnetism, but its utility can be severely limited by the lack of knowledge of the muon implantation site and the extent to which the muon perturbs its host. In a system of ionic fluorides, where partial information about the muon site is experimentally available, I demonstrate systematically that these problems can be addressed accurately using electronic-structure calculations. The F–μ–F complex formed by muons in many fluorides can be understood as an exotic molecule-in-a-crystal defect with a zero-point energy larger than that of any naturally-occurring triatomic molecule.

I demonstrate the interesting possibility of controlling the magnetic dimensionality in a molecular magnet using applied pressure. μ^+SR and high-field magnetisation experiments under applied pressure on the coordination polymer $CuF_2(H_2O)_2$(pyrazine) show a transition from a quasi-two-dimensional to a quasi-one-dimensional antiferromagnetic phase. Density-functional theory calculations and calculations of the dipolar anisotropy complement the experiments.

I describe how subtle differences in chemical composition can lead to starkly different structural and magnetic properties. $[Cu(pyz)(H_2O)(gly)_2](ClO_4)_2$ may be considered an antiferromagnetic chain that orders below 50 mK while the related compound $[Cu(pyz)(gly)](ClO_4)$ is formed from Cu^{2+} dimers and remains disordered down to 30 mK in zero field, but displays a field-temperature phase diagram consistent with the Bose-Einstein condensation of triplons. I also describe μ^+SR measurements on the strong-leg spin ladder DIMPY and on the molecular nanomagnets Cr_8Cd and Cr_8Mn which highlight some of the remaining challenges for longitudinal-field μ^+SR experiments.

Acknowledgements

I am greatly indebted to my supervisors Steve Blundell and Tom Lancaster. Throughout the years during which this research was conducted they have been a constant source of encouragement, insightful advice, fruitful ideas, humorous anecdotes, and good common sense.

My experiments were performed in the friendly environments of the ISIS pulsed muon source and the Paul Scherrer Institut in Switzerland. I am particularly grateful to Peter Baker and Francis Pratt for their kindness, outstanding support as instrument scientists, fruitful collaboration and good company during long experiments at ISIS and PSI. Part of the experimental muon data presented here was analyzed with the WiMDA program, written and kindly provided by Francis Pratt. I would like to thank Chris Baines for his heroic efforts on LTF and Alexander Maisuradze and Rustem Khasanov for their fearless help with the pressure cell on GPD, despite one disintegrating in front of us.

My experimental work using muons has benefitted greatly from collaborations employing complementary techniques. I am particularly grateful to Saman Ghannadzadeh and Paul Goddard for collaborations on many projects, especially on $CuF_2(H_2O)_2(pyz)$.

None of the experiments would have been possible without the high-quality samples provided by John Schlueter, Jamie Manson, Grigore Timco, Richard Winpenny, Gonca Seber, Paul Lahti, Chris Landee, and Prabhakaran.

My work using density-functional theory would not have been possible without the expert advice from Davide Ceresoli and Nicola Marzari, who I also thank for their hospitality while visiting them. DFT calculations were performed on computers of the E-Infrastructure South Initiative (UK), Très Grand Centre de calcul (France), CINECA (Italy), EPFL (Switzerland), and MIT (USA). I thank Andrew Steele for providing mμcalc.

I thank all members of the Clarendon for the friendly environment, in particular my office mates Ben, despite the monthly punches, Saman, Katie, Sam as well as Jack and Francesca and all other members of the Quantum Matter group. I thank Bill Hayes for friendly tea-time chat, interesting anecdotes, useful comments on this work at various stages, and for reading through this thesis.

I am grateful to Merton College and the IOP for financial support to attend two international conferences, and EPSRC for the provision of a studentship.

My friends have enriched my life outside physics, special mention to Clemens, Vikaran, Emanuele, Anna, Christian, Giulio, and Chris, who I am greatly indebted to for friendly advice on many occasions over now seven years in Oxford. I thank my brother Julian and my sister-in-law Maike. I thank Charlotte for deciding that I was not so boring after all. Finally, I am grateful to my parents Rüdiger and Hannelore for their unfailing support throughout.

To my family

Contents

Abstract i

Acknowledgements iii

1 Introduction 1
- 1.1 Transition-metal coordination polymers . . . 2
- 1.2 Low-dimensional magnetism . . . 3
  - 1.2.1 A quantum zoo of exotic ground states and excitations . . 5
  - 1.2.2 Experimental realisations . . . 7
- 1.3 Thesis outline . . . 8

2 Muon-spin relaxation 11
- 2.1 Production of spin-polarised muons . . . 12
- 2.2 Muon stopping process . . . 16
- 2.3 Muon decay . . . 17
- 2.4 Experimental considerations . . . 18
- 2.5 Magnetic coupling of the muon . . . 21
- 2.6 Polarisation functions . . . 25
  - 2.6.1 Transverse geometry . . . 26
  - 2.6.2 Longitudinal geometry . . . 27
- 2.7 Conclusion . . . 31

3 Density-functional theory 33
- 3.1 The correlated many-body problem . . . 34
- 3.2 The Hohenberg-Kohn principle and the Kohn-Sham equations . . 35
  - 3.2.1 The exchange-correlation energy . . . 36
- 3.3 Computational details . . . 37
  - 3.3.1 Structural optimisations . . . 37
  - 3.3.2 Practical considerations . . . 38

4 The quantum states of muons in fluorides 41
- 4.1 Introduction . . . 42
- 4.2 Muon-fluorine entanglement . . . 44

4.3 Computational details . . . 45
4.4 Diamagnetic states . . . 46
4.4.1 Equilibrium geometries . . . 46
4.4.2 The perturbation caused by the muon . . . 49
4.4.3 Quantum effects . . . 53
4.4.4 Comparison with other work . . . 56
4.5 Muonium . . . 58
4.5.1 Equilibrium geometries . . . 58
4.5.2 The perturbation caused by the muon . . . 59
4.5.3 Quantum effects . . . 61
4.6 Comparison with electrostatic potential . . . 65
4.7 Conclusions and outlook . . . 67

5 A pressure-operated magnetic dimensionality switch 69
5.1 Introduction . . . 70
5.2 Previous work on $CuF_2(H_2O)_2(pyz)$ . . . 71
5.3 Muon measurements . . . 74
5.3.1 Experimental details . . . 74
5.3.2 Experimental results . . . 76
5.4 Density-functional theory calculations . . . 80
5.4.1 DFT computational details . . . 84
5.4.2 DFT results . . . 85
5.5 Magnetisation results . . . 98
5.6 Further discussion . . . 100
5.7 Conclusions and outlook . . . 103

6 Quantum magnetism in applied fields 105
6.1 Introduction . . . 106
6.2 An antiferromagnetic chain: $[Cu(pyz)(H_2O)(gly)_2](ClO_4)_2$ . . . 107
6.3 A dimer system: $[Cu(pyz)(gly)](ClO_4)$ . . . 110
6.3.1 Structure . . . 110
6.3.2 Zero-field ground state . . . 110
6.3.3 Triplon condensation in applied field . . . 113
6.3.4 Discussion . . . 119
6.4 Conclusions . . . 124
6.5 Further LF μ^+SR measurements . . . 125
6.5.1 A spin ladder in the strong-leg regime . . . 125
6.5.2 Level-crossings in molecular nanomagnets . . . 131

Bibliography 139

List of publications 153

Chapter 1

Introduction

> *What phenomenon is more astonishing? Where has Nature shown greater audacity? For iron, the tamer of all substances, is drawn to the magnet, follows some intangible attraction, and, as it comes nearer, leaps to meet the magnet, is held, and clings fast in its embrace.*
> Plinius (AD 23-79)

Since the first mention of the mysterious properties of magnets by Thales of Miletus in the sixth century BC, humans have been fascinated by magnetism. From the discovery of the invisible force exhibited by lodestone[1] on iron more than 2000 years ago until very recently magnetism has usually been associated with relatively simple inorganic materials; lodestone, or magnetite (Fe_3O_4), being the first example. Even modern research into magnetism has long focussed on these compounds as it was believed that these would most easily provide information on the fundamental physical processes. More recently it was realised that magnetic systems built on molecules offer enormous benefits. Purely organic molecules containing only s and p electrons were long thought to be incapable of supporting any

[1] From 'lode' meaning 'way', 'course', or 'guide', indicating the use of lodestone as a compass.

type of magnetic order since they lack unpaired spins. Organic radical systems, however, do contain unpaired spins, which frequently align antiferromagnetically forming bonding orbitals consisting of the singly-occupied molecular orbitals of neighbouring molecules. The first example of a purely organic ferromagnet was reported in 1991 by a Japanese group [1]. The system, which orders below a temperature of 0.65 K, is based on a nitronyl nitroxide group which hosts the radical electron. While this does represent an important proof of principle, the usefulness of purely organic magnets remains limited; in part this is due to the difficulty of chemically stabilising radicals into crystalline structures.

1.1 Transition-metal coordination polymers

An alternative, and far more useful strategy, is to embed magnetic transition metal ions (such as Cu^{2+}) into a molecular framework [2]. The organic ligands which coordinate the metal ions frequently provide the superexchange pathways that define the magnetic dimensionality of the system. One of the first known magnetic transition metal coordination polymers of this type is Prussian blue, $Fe_4^{3+}[Fe^{2+}CN_6]_3{\cdot}15H_2O$, which was first synthesised around 1704 by the colour-maker Diesbach as one of the first synthetic pigments. Its magnetic properties were only discovered in the 1950s when it was found to order ferromagnetically below approximately 5.5 K [3; 4]. Many related Prussian blue compounds exist, some of which undergo ordering at very high temperatures. One of the most spectacular examples is that of $V[Cr(CN)_6]_{0.86}{\cdot}2.8H_2O$ which has a Curie temperature of 315 K [5]. However, unlike for the superconductivity community, a high transition temperature is not of primary interest in the field of molecular magnetism. Indeed the most interesting physics is usually found at the lowest

temperatures, where quantum effects are dominant, and often in systems that do not order at any finite temperature.

It is the vast tunability afforded by coordination chemistry that is the foremost, albeit not only, advantage of molecular systems over inorganic ones[2]. In particular it is possible to grow molecular magnets with different structural motifs and magnetic dimensionalities ranging from three to zero dimensions. Furthermore, to a first approximation, for most of the systems considered here the spins do not favour any one direction over another. The resulting magnetic Hamiltonian is the Heisenberg Hamiltonian[3]

$$\hat{\mathcal{H}} = \sum_{\langle ij \rangle} J_{ij} \hat{\mathbf{S}}_i \cdot \hat{\mathbf{S}}_j, \tag{1.1}$$

where the sum is over nearest neighbour spins $\hat{\mathbf{S}}_i$ and $\hat{\mathbf{S}}_j$, and J_{ij} is the exchange constant which can be such that exchange takes place in all three dimensions, confined to a plane or a chain, or confined to a single molecule (the zero dimensional case).

1.2 Low-dimensional magnetism

Magnetic systems with low-dimensional structural motifs are a particularly rich playground for the exploration of exotic quantum effects [6]. This is to a large extent because there is no long-range order at any finite temperature in any isotropic Heisenberg system in less than three dimensions. This is known as

[2]While the metal-organic complexes referred to here are strictly also in the realm of inorganic chemistry, the term inorganic system here will be used to denote anything not made from molecules.

[3]For the rest of this thesis, operators such as $\hat{\mathbf{S}}$ will be indicated without the hat to avoid clutter.

Mermin-Wagner theorem and was proven around the same time (using different methods) by Mermin and Wagner [7], Hohenberg [8], Berezinsky [9; 10], and Coleman [11]. The most obvious way that long-range order can still occur in a real one or two-dimensional system is if there is a weak interchain or interplane coupling. Such systems are referred to as quasi one-dimensional and quasi two-dimensional, respectively, and will be studied in quite some detail here. Significant effort has been devoted over the last 50 years using sophisticated theoretical techniques to understand the implications of other modifications to the Hamiltonian in Eq. 1.1. Some of the earliest examples include the work of Berezinsky [9; 10] and Kosterlitz and Thouless [12; 13] (BKT) on two-dimensional systems in which spins are confined to a plane (the so-called XY-model). Much of the interest in low-dimensional systems centres on the types of excitations they permit. The XY model allows the existence of *vortex* excitations, which – while not stable on their own – can be stabilised through the formation of bound vortex-antivortex pairs. These vortex-antivortex pairs exhibit a different type of order, coined *topological order*, because it does not involve symmetry-breaking, below a certain temperature T_{BKT} above which vortices are stabilised by thermal fluctuations. While indirect observations of BKT physics have been made, for example in a molecular magnet [14] (briefly discussed in Chapter 6), a direct observation of the BKT transition remains elusive to date. A more complicated topological object called a *meron* can form in two-dimensional systems if the interaction *is* isotropic, allowing the spins to tilt out of the xy plane. A meron-antimeron pair with opposite spins is called a *skyrmion* [15] and has received considerable attention recently in the context of spintronic applications [16].

1.2.1 A quantum zoo of exotic ground states and excitations

A wealth of states is revealed when the Hamiltonian in Eq. 1.1, and modifications thereof, are studied in detail. Let's consider a one-dimensional system with zero interchain coupling. A particularly useful model is the so-called J_1-J_2 model which allows both nearest-neighbour (J_1) and next nearest-neighbour (J_2) interactions, as well as an anisotropy parameter α which tunes between the XY ($\alpha = 0$), isotropic ($\alpha = 1$), and Ising ($\alpha \gg 1$) cases:

$$\mathcal{H} = J_1 \sum_{\langle ij \rangle} (S_i^x S_j^y + S_i^y S_j^y + \alpha S_i^z S_j^z) + J_2 \sum_{ik} (S_i^x S_k^y + S_i^y S_k^y + \alpha S_i^z S_k^z), \qquad (1.2)$$

where the first sum is over nearest neighbours and the second sum is over next-nearest neighbours along the chain. For $\alpha \leq 1$ and J_2/J_1 below a critical value this leads to the prediction of a gapless state[4] with linearly-dispersing excitations, which remains disordered at $T = 0$, called a *Tomonaga-Luttinger liquid* [17; 18]. If, instead, the system was Ising-like (i.e. $\alpha \gg 1$), a Néel-ordered state with gapped spinon excitations is realised at zero temperature. Note that while it may seem a purely academic discussion whether or not a system may order at zero temperature since it is not possible to cool any system down to that temperature, there is an important distinction whether it is classical (thermal), or quantum-mechanical fluctuations[5] that destroy magnetic order. For J_2/J_1 above a critical value the system undergoes formation of a spin-Peierls (or valence-bond) state below a transition temperature T_{SP} which is characterised by antiferromagnetically

[4] In particle physics terminology these gapless excitations are massless Goldstone modes.

[5] Meaning a time-dependence of the wavefunction. These quantum fluctuations are analogous to the vacuum fluctuations that renormalise the values of mass and charge of elementary particles that we observe.

coupled dimers along the chain and possesses gapped spinon excitations [19].

Note that the above is only valid for half-integer spin chains. For integer-spin chains the situation is somewhat more complicated and less is known about their phase diagram [20]. A topological difference between integer and half-integer spins leads to a qualitative difference in their excitation spectrum [21]. Driven by nonlinear zero-point fluctuations (called *instantons*), a process known as *dynamical mass generation* gives rise to a gap in the excitation spectrum for sufficiently small anisotropy (of easy-plane or easy-axis type), the famous *Haldane gap* [22; 23].

The physics of two-dimensional magnetism is no less extraordinary. For the case of spin-1/2 this is of course the low-energy model that describes the Mott-insulating parent phase of the high-T_c cuprate superconductors [24]. While a two-dimensional isotropic Heisenberg magnet does not order at any finite temperature by the Mermin-Wagner theorem, it is thought to order at zero temperature, albeit with a heavily renormalised moment [25]. In two-dimensional systems a lot of interest centres around *quantum phase transitions*. These are phase transitions that are driven not by temperature, but by a different variable, usually applied pressure, magnetic field, or doping. Since it is not temperature that is driving these transitions, they can be said to be zero-temperature phase transitions at a critical point known as *quantum critical point* (QCP). A QCP represents a singularity in the phase diagram with very unusual physics in the quantum critical region. For this reason QCPs have been the cause for substantial theoretical and experimental interest [26; 27]. Finally, it is worth noting that specific crystal geometries (for example a two-dimensional triangular lattice) prevent the competing interactions in an antiferromagnet to be satisfied simultaneously which can lead to a ground state known as a (quantum) spin liquid [28]. A quantum

spin liquid can be considered quantum disordered, so that quantum, rather than thermal fluctuations, prevent the condensation of magnetic order and for this reason they too have attracted considerable experimental and theoretical interest recently.

1.2.2 Experimental realisations

As Richard Feynman put it "Experiment is the sole judge of scientific truth". But experimental tests of any of the exotic and fascinating states briefly introduced above rely crucially on the existence of real materials with suitable properties. The tunability of molecular magnets has allowed a number of successful experimental realisations. These include a Tomonaga-Luttinger liquid phase [29] in a strong-rung spin-ladder[6], the Bose-Einstein condensation of triplons by driving a dimerised system through a quantum critical point under an applied magnetic field [31], zero-dimensional single molecular magnets, most recently studied in anticipation of their deployment as elements of a quantum computer [32], as well as a two-dimensional quantum spin liquid on a triangular lattice [33]. The properties of these systems frequently involve small magnetic moments, phase separations, or correlations that mask the magnetic transition. For this reason the primary experimental technique employed in this thesis, muon-spin relaxation, has proven particularly useful.

The study of low-dimensional magnetism has borne fruit outside of academia. It was the pure scientific curiosity to understand the magnetism in thin films that has lead to the discovery of the giant magnetoresistance effect by groups lead by Peter Grünberg and Albert Fert in 1988. Their discovery lies at the heart of all

[6]In a spin ladder the topology of the magnetic interactions is that of a ladder [30]. A discussion is given in Chapter 6.

modern hard drives; a business worth an estimated US$ 37 billion annually in 2012 [34].

Scientific discovery is not always driven by theory but frequently it is led by serendipity. From the discovery of the Cosmic Microwave Background by Arno Penzias and Robert Wilson using the antenna they had intended to use for radio-astronomy observations [35], to the discovery of the inhibition of cell-division in E. coli bacteria by the transition metal complex cisplatin[7], today one of the most commonly used chemotherapy drugs, by Rosenberg, Van Camp, and Krigas in experiments investigating the effect of electric fields on the growth of bacteria [36]. What is luck to the cynic, would not have been possible without extreme diligence and systematic scientific methodology. The possibility of performing systematic studies of fundamental magnetic properties by varying the geometry and composition of molecular magnets is another one of their benefits. For example, on a far more humble scale, this has led to the discovery of the dimerisation in the gly-based molecular magnet discussed in Sec. 6.3 which we originally studied in the context of BKT physics.

1.3 Thesis outline

The plan for this thesis is as follows:

Chapter 2 introduces the primary experimental technique employed in this thesis: muon-spin relaxation.

Chapter 3 contains an introduction to density-functional theory, which I have used to address one of the most fundamental limitations of the muon-spin

[7] The ineffectiveness of its *trans* isomer is but one example of the versatility of organic chemistry and the biological selectivity of Nature.

relaxation technique, which concerns the lack of knowledge about where muons implant in a material and how they perturb it locally.

Chapter 4 describes theoretical work on the quantum states of muons in a series of fluorides where, unusually, information on their site is available experimentally, enabling a direct comparison with density-functional theory calculations.

Chapter 5 contains a combination of experimental and computational work on the coordination polymer $CuF_2(H_2O)_2$(pyrazine) which may be driven from a quasi-two-dimensional to a quasi-one-dimensional phase through a pressure-induced quantum critical point.

Chapter 6 details a number of measurements on molecular magnets in applied fields. Two molecular magnets were synthesised using the same method and starting compounds. One displays quasi-one-dimensional magnetism and orders at low temperatures in zero-field due to weak interchain interactions. The other is found to dimerise and remains disordered down to zero temperature. However, in an applied magnetic field the dimer system may be driven into an ordered phase *via* a field-induced quantum critical point in a process that could be described as the Bose-Einstein condensation of triplons. Furthermore the field-induced zero-temperature cross-over into a Tomonaga-Luttinger liquid regime is studied in the strong-leg spin ladder system DIMPY. Also presented is a study of field-induced level crossings in zero-dimensional molecular nanomagnets.

The introduction to muon-spin relaxation and density-functional theory is kept relatively brief as both are documented extensively in the literature. Further experimental and computational details are given in some of the later chapters.

Chapter 2

Muon-spin relaxation

> *I don't think that God is a weak left-hander, and I am ready to make a substantial bet that the experiment will give a symmetrical result.*
> Wolfang Pauli (1900-1958)

The experiment that Pauli was referring to above was that of Wu *et al.* [37] to test the Lee-Yang proposal of parity violation by the weak interaction in an experiment studying the angular distribution of decay electrons from the beta decay of polarised Co^{60} nuclei. Pauli was wrong. The distribution of decay electrons *was* asymmetric, confirming parity violation by the weak interaction and won Lee and Yang the Nobel Prize in the same year. However, on learning of Wu *et al.*'s result, Pauli did prove a good sense of humour by saying "God is indeed a weak left-hander [...] The laughter is rightly with the others." [38]. Published on the next page in the same issue of what was to become Physical Review Letters (though begun after preliminary results of Wu *et al.*'s experiment became known) is an experiment by Garwin, Lederman and Weinrich [39]. They too set out to investigate the Lee-Yang proposal, albeit not in spin-polarised Co^{60} nuclei but in the decay of the positive pion to a positive muon (and a neutrino) and the

subsequent decay of the muon. If parity was indeed violated the positron resulting from muon decay should have an asymmetric spatial distribution with respect to the original momentum of the muon. Their experiment may be described as the first muon-spin rotation experiment and, needless to say, it too was a success.

2.1 Production of spin-polarised muons

The basic principle of a muon-spin rotation/relaxation/resonance (μ^+SR) experiment is to observe the time-evolution of the spin of an ensemble of muons implanted into a sample. The spin may rotate in an applied field, it may relax due to a spatial or temporal distribution of fields at the muon site, or it may be made to resonate in an applied radio-frequency field (the latter will not be discussed in this thesis). While originating from fundamental particle physics, it was quickly realised that the experiment by Garwin, Lederman, and Weinrich could be utilised in the study of condensed matter physics systems. In principle one could use either positive or negative muons for this purpose. However, for condensed matter physics research, positive muons have been found to be much more useful because they tend to implant at interstitial sites close to the electron density or bond with electronegative atoms. Negative muons on the other hand can undergo capture by nuclei (for example in the reaction $C^{12} + \mu^- \rightarrow B^{12} + \nu_\mu$) and are less useful for condensed matter experiments. This thesis is only concerned with the use of positive muons, whose properties are summarised in Table 2.1.

In a μ^+SR experiment, positive pions are produced by colliding protons (of

	e	μ	p
Charge	e	e	e
Spin	1/2	1/2	1/2
Mass	m_e	207 m_e	1836 m_e
	0.0054 m_p	0.11 m_p	m_p
Gyromag. ratio $\gamma/2\pi$ (MHz/T)	28025	135.5	42.58
Lifetime	$> 4.6 \times 10^{26}$ yr	2.197 μs	$> 2.1 \times 10^{29}$ yr

Table 2.1: Summary of properties of the electron, the muon, and the proton. All data are from Refs. 40 and 41.

energy between 600 and 800 MeV) with a target[1]

$$p + p \rightarrow p + n + \pi^+ \tag{2.1}$$

$$p + n \rightarrow n + n + \pi^+. \tag{2.2}$$

The π^+ (spin 0) decay with a mean lifetime of 2.6×10^{-8} s and with a branching ratio of nearly 100% [40] *via*

$$\pi^+ \rightarrow \mu^+ + \nu_\mu. \tag{2.3}$$

The most common mode of μ^+ production utilises pions decaying at rest from the surface layer of the target. The muons produced this way are therefore coined *surface muons*. In the pion rest frame these muons emerge with a kinetic energy E_k and momentum p_μ

$$E_\mathrm{k} = \frac{(m_{\pi^+} - m_\mu)^2 c^2}{2m_{\pi^+}} = 4.1 \text{ MeV}, \tag{2.4}$$

$$p_\mu = \frac{m_{\pi^+}^2 - m_\mu^2}{2m_{\pi^+}} c = 29.8 \text{ MeV/c}, \tag{2.5}$$

[1]Usually carbon; heavier nuclei cause more scattering of the proton beam and showers of other particles. This is not desirable since muon beam lines are often placed 'parasitically' on neutron beam lines. At the ISIS muon source the carbon target is 10 mm thick and the muon target uses 2-3% of the proton beam.

where m_{π^+} is the mass of the positive pion and c is the speed of light. It is also possible to utilise the muons from the in-flight decay of pions to boost the muon momentum. This is useful if the muons need to penetrate the walls of a pressure cell as discussed in Chapter 5. Due to the maximal violation of parity by the weak interaction, the neutrino (spin 1/2) only exists in a negative helicity state (its spin is antiparallel to its momentum). As process 2.3 is a two-body decay, the restrictions imposed by conservation of linear and angular momentum are absolute and the μ^+ (spin 1/2) is 100% polarized with its spin antiparallel to its momentum. The resulting muons are guided to the sample by dipole guiding magnets and quadrupole focussing magnets. As the muon has a g-factor of 2 (apart from a small anomalous correction) the dipole magnets rotate muon spin and momentum at the same rate, maintaining their relative orientation and the spin-polarisation of the beam. Some filtering of the beam is already achieved this way since the radius of the bending beam in a magnetic field B is given $r = p/(qB)$, where p is the particle momentum and q is the particle charge and so only particles with a certain p/q ratio are guided towards the sample. However, some contamination (particularly by positrons) remains. To further filter the beam a *Wien filter* is used. A Wien filter consists of perpendicular electric E_x and magnetic fields B_y. A particle of charge e travelling with momentum p_z and velocity v_z along the z-direction will experience a force

$$\mathbf{F} = (ev_zB_y - eE_x)\hat{\mathbf{x}} \tag{2.6}$$

along the x-direction. This force is zero if $v_z = E_x/B_y$ and so allows particles of a particular mass to be selected (after dipole magnets have selected a particular momentum). In addition to allowing contaminant particles to be filtered (which

only depends on the ratio E_x/B_y) it is possible to rotate the initial muon spin using a Wien filter since the spin is rotated only by the magnetic field but not by the electric field. The extent to which this is possible depends on technical details of the beam line like the power supply available to beam line magnets. Rotating the initial muon spin is particularly useful at continuous muon sources (see below) since it allows experiments in high transverse magnetic fields that would otherwise be prohibited by the longitudinal geometry of superconducting magnets on a muon beam line. A schematic of the muon beamline at the European muon facility at ISIS is shown in Fig. 2.1.

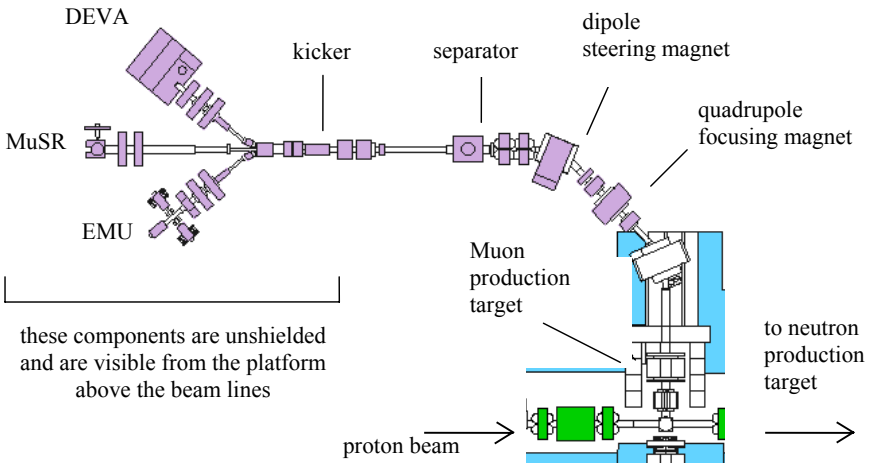

Figure 2.1: Schematic of the European muon facility at ISIS from Ref. 42. MuSR and EMU are two of the currently operational instruments. DEVA has now been replaced with the high-field spectrometer HiFi. The separator is a Wien filter and the kicker splits every other pulse between HiFI and EMU, the other pulse going exclusively to MuSR (the pulse at ISIS is a double pulse with two 80 ns wide pulses separated by 300 ns).

The proton beam (and hence the muon beam) can be either pulsed (where protons are accelerated in bunches in a synchrotron) or continuous (where protons are accelerated in a cyclotron and spiral outwards continuously). An example of a continuous muon source is the Swiss muon source (SμS) at the Paul Scherrer

Institut, Switzerland. The ISIS neutron and muon source at the STFC Rutherford Appleton Laboratory in Oxfordshire is an example of a pulsed muon source[2]. The main advantage of continuous sources over pulsed sources is their higher time resolution. For pulsed sources the time resolution is ultimately limited by the temporal width of the muon pulse (about 80 ns at ISIS [42]). For this reason, oscillations or relaxations faster than approximately 10 MHz cannot be observed at ISIS and the amplitude of the response decreases for higher frequencies even below this limit (in a way that is determined primarily by the Fourier transform of the pulse). At PSI on the other hand the time resolution is determined only by the time resolution of the detectors which allows oscillations even extending into the GHz range to be resolved. However, because each pulse at a pulsed source contains thousands of muons, the counting rates at which data can be measured are significantly higher than at continuous sources.

2.2 Muon stopping process

A muon impinging on a sample loses energy through ionisation of atoms and scattering off electrons succeeded by electron capture and loss (muonium formation) and muonium atom collisions and finally thermalises as interstitial diamagnetic μ^+ or as neutral muonium (a muon-electron bound state). However, in particular concerning the formation of muonium there are some additional complications. There is now good experimental evidence that different types of muonium states form at different stages during the stopping process. The so-called normal muo-

[2]More specifically the cyclotron at PSI operates at a frequency of 50 MHz producing anything between zero and a few muons in each instrument in a 10 μs time window, while the synchrotron at ISIS operates at 50 Hz producing approximately 4000 muons 50 times a second in the MuSR muon spectrometer (and about half as many in the other two European muon instruments, EMU and HiFi).

nium in silicon forms *epithermally*, i.e. prior to final thermalisation while the so-called anomalous muonium forms *via* electron transport to a thermalised positive muon [43; 44]. The stopping range of surface muons is typically about 110 mg cm^{-2} with a width of approximately 20% [45]. For most samples this is within 1 mm from the sample surface (less if there are many or particularly thick beam windows degrading the muon momentum prior to implantation) and the whole process usually takes less than 1 ns [45]. In any case the stopping process has two important characteristics: (i) any appreciable radiation damage (vacancy production) caused by the muon lies in the early part of the muon trajectory and sufficiently far (several μm) from the final stopping site [46], (ii) the muon retains almost 100% of its polarization [47].

2.3 Muon decay

After stopping in an interstitial site, the μ^+ spin will precess in the local magnetic field[3] $\mathbf{B}$ with angular frequency $\omega = \gamma_\mu |\mathbf{B}|$, where $\gamma_\mu = 2\pi \times 135.5$ MHz/T is the muon gyromagnetic ratio [47]. After a mean lifetime of 2.2 μs the muon decays *via*

$$\mu^+ \rightarrow e^+ + \nu_e + \bar{\nu}_\mu. \tag{2.7}$$

Since this is a three-body decay, the constraints imposed by parity violation and conservation of linear and angular momentum are not as strict as for the decay of the π^+. In particular, there is a distribution of possible energies for the positron ranging from 0 to 52.8 MeV (in the muon rest frame). Nonetheless an asymmetry in the direction of emission of the decay positrons is maintained. The number $N(\theta)$ of positrons emitted at an angle θ with the muon spin direction at the time

[3] Details of the magnetic coupling of the muon are discussed in Sec. 2.5.

of decay is given by

$$N(\theta) = N_0[1 + a(E_{e^+})\cos\theta], \tag{2.8}$$

where $a(E_{e^+}) = 1$ for the maximum possible positron energy of 52.8 MeV and $a(E_{e^+}) = 1/3$ averaged over all positron emission energies [39; 48]. This distribution is shown in Fig. 2.2.

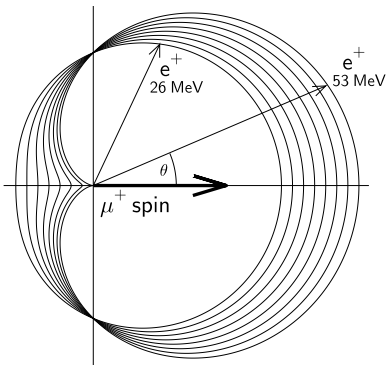

Figure 2.2: Positron decay asymmetry for different positron energies, from Ref 49. The maximum positron energy in the muon rest frame is 52.8 MeV.

2.4 Experimental considerations

The positron decay asymmetry is sampled experimentally through a set of detectors placed in front of and behind the initial muon spin polarisation (see Fig. 2.3). Given sufficient statistics, it is therefore possible to follow the time evolution of the muon spin by measuring

$$A(t) = \frac{N_{\mathrm{F}}(t) - \alpha_{\mathrm{exp}} N_{\mathrm{B}}(t)}{N_{\mathrm{F}}(t) + \alpha_{\mathrm{exp}} N_{\mathrm{B}}(t)}\,, \tag{2.9}$$

where α_{exp} is an experimental calibration constant accounting for different detector efficiencies, and N_{F} and N_{B} are the positron counts detected in a set of forward and backward detectors. α can be calibrated in an experiment in an

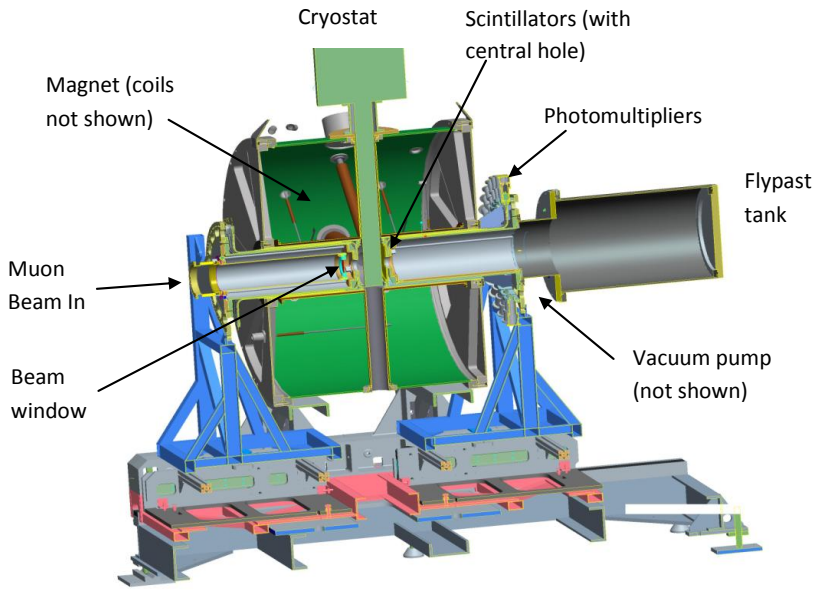

Figure 2.3: Schematic of the HiFi spectrometer at ISIS, from Ref 50. The scintillators are the primary detector element that allows the time evolution of the muon spin to be followed.

applied transverse field, typically 2 or 5 mT (which will lead to precession of the muon spin). If α is calibrated correctly, the time-integrated asymmetry in a transverse field experiment should be zero outside of any magnetic phase in the sample. By construction the asymmetry $A(t)$ is proportional to the spin polarisation of the muon ensemble.

There are a number of practical considerations that will only be briefly discussed here. The time t is measured by starting a clock either when a muon passes through a scintillator placed at the entrance of the instrument (as is the case for example for the GPS instrument at PSI) or through a signal from the proton accelerator (as is the case at ISIS). The experimental time $t = 0$ then needs to be determined through calibration to account for delays due to the muon flight time, pulse width, and to exclude noise at early times (for example due to positrons from muons decaying in flight in the beamline). At a continuous source it needs

to be ensured that no two muons are in the detector at any one time (at PSI the experimental time window is usually 10 μs compared with 30 μs at ISIS) since the time of decay could then not be identified. Therefore, an electronic veto exists that ensures that if a second muon enters the instrument before the first has decayed, any events are disregarded until both muons have decayed. Since it is more likely for a second muon to have entered the instrument after a longer time, this selectively disposes of decays after long times and therefore causes a distortion of the signal that can, however, be corrected for. A similar veto ensures that the muon has actually stopped in the sample. While the pulsed nature of the beam prevents the observation of very fast effects (as discussed above), the long time window at a pulsed source allows the observation of very slow oscillations and dynamics ($\geq$ 0.03 MHz) that could not be studied at a continuous source (which is not sensitive to effects slower than 0.1 MHz).

Each detector consists primarily of a set of scintillators and photomultipliers. Another consideration concerns the finite dead time (typically about 10 ns) of each detector. This causes a more serious problem at pulsed sources since many more muons decay within a short time window than at continuous sources. For this reason, detectors at pulsed sources are highly segmented so that the count rate in each detector remains relatively low. For example, the MuSR instrument at ISIS uses 64 individual detectors (usually grouped into one forward and one backward group) while the GPS instrument at PSI only uses five separate detectors. A distortion of the data would remain in either case since more decays are missed at early times when many muons decay but this can be taken account of by performing a calibration run on a sample that does not depolarise muons strongly (such as silver).

Samples are often mounted on a silver backing plate. Elemental silver is dia-

magnetic and so there is no electronic magnetism that could cause a background to the measurement. Furthermore silver has a very small nuclear magnetic moment[4]. Gold has a similar nuclear moment but a larger atomic radius and so would be even more suitable, but its use in μ^+SR is limited by financial constraints. However, this is not much of a concern since silver is adequate for most measurements. If the background is a major concern (for example in very weakly magnetic samples) then a *fly-past* geometry, where the sample is mounted on a type of fork (usually made from silver), can be a suitable alternative.

2.5 Magnetic coupling of the muon

So far it has only been discussed how the time-evolution of the muon spin may be measured experimentally. In this section I describe the magnetic coupling of the muon that leads to the time-dependence of its polarisation. The magnetic coupling of a muon located at $\mathbf{r}_\mu$ can be described as a sum of the following interactions [48; 51]

- An externally applied field $\mathbf{B}_{\text{ext}}$, usually either parallel (longitudinal) or perpendicular (transverse) to the initial muon spin direction.
- The dipolar coupling with localised electronic or nuclear magnetic moments $\mathbf{m}_i$ located at position $\mathbf{r}_i$ given by

$$\mathbf{B}_{\text{dip}}(\mathbf{r}_\mu) = \frac{\mu_0}{4\pi} \sum_i \frac{3(\mathbf{m}_i \cdot \hat{\mathbf{r}}_{i\mu})\hat{\mathbf{r}}_{i\mu} - \mathbf{m}_i}{|\mathbf{r}_\mu - \mathbf{r}_i|^3}, \tag{2.10}$$

  where μ_0 is the vacuum permeability, $\hat{\mathbf{r}}_{i\mu}$ the normalised vector between the muon and the moment $\mathbf{m}_i$. For a delocalised spin-density due to itinerant

[4]There are two stable isotopes of silver: Ag_{107} and Ag_{109}, both have a nuclear moment of about 0.1 μ_n, compared with 2.8 μ_n for a proton.

moments or muonium formation (see below) Eq. 2.10 needs to be replaced with an analogous integral of the spin density. The dipolar interaction may be evaluated for an infinite sample by calculating the magnetic field given by Eq. 2.10 within a sphere of finite radius r_{L}, the so-called *Lorentz-sphere*. The Lorentz sphere needs to be sufficiently large to reach satisfactory convergence of the calculated field. Usually a Lorentz sphere encompassing a few hundred spins is sufficient to yield results converged to within a few percent (and therefore of similar accuracy as the experimentally-measured coupling). While the dipolar interaction in Eq. 2.10 is generally referred to as long-range (compared primarily to the contact term discussed below), this is a reflection of its relative 'near-sightedness', discussed in more detail in Chapter 4. The dipolar field from all moments outside of the Lorentz sphere is given by a sum of

– The Lorentz field

$$\mathbf{B}_{\mathrm{L}} = \mu_0 \mathbf{M}/3, \tag{2.11}$$

where $\mathbf{M}$ is the magnetisation of the Lorentz sphere. Note that this term vanishes for an antiferromagnet[5].

– The demagnetising field caused by the divergence of the magnetisation $\mathbf{M}$ at the sample's surface $\nabla \cdot \mathbf{H} = -\nabla \cdot \mathbf{M}$, given by

$$\mathbf{B}_{\mathrm{demag}} = -\mu_0 \mathbf{N} \cdot \mathbf{M}, \tag{2.12}$$

where $\mathbf{N}$ is the demagnetising tensor, which depends on the sample

[5]Strictly speaking this term may not be exactly zero due to the way that the Lorentz sphere cuts off the crystal (leaving some unpaired spins even in an antiferromagnet). However, for sufficiently large Lorentz spheres this term is negligible.

shape, and **M** is the net magnetisation of the measured sample. For a spherical sample **N** is diagonal with elements 1/3 and therefore the Lorentz and demagnetisation fields cancel.

- If there is any polarised spin density $\rho(\mathbf{r}_\mu)$ at the muon site there is a Fermi contact interaction

$$A = \frac{2\mu_0}{3}\gamma_e\gamma_n\rho(\mathbf{r}_\mu), \tag{2.13}$$

where γ_μ is the muon gyromagnetic ratio and γ_e is the electron gyromagnetic ratio. The contact coupling distinguishes two fundamentally different types of muon sites in solids:

1. The *diamagnetic* type where the contact coupling is negligible. This state is most commonly utilised in μ^+SR experiments on magnetism since the primary coupling of the muon is with the electronic and nuclear magnetic moments in the solid.

2. The *paramagnetic* state where the contact coupling is significant. This state is often referred to as *muonium* (or Mu), a neutral muon-electron bound state very much like hydrogen in many respects apart from its gyromagnetic ratio and its lower total mass[6]. Muonium can form in a large variety of compounds but surprisingly never in metals. At first sight this seems paradoxical given the abundance of electrons in a metal that a muon could acquire to form μ^+e^-. However, it is the screening afforded by the electron density in a metal that prevents a muon from forming a bound state with any one electron [52]. Note that it is also possible to create negatively charged muonium Mu^-, which

[6]Note that the reduced mass of the electron is nearly identical in muonium and hydrogen, so the energy levels of atomic muonium and hydrogen are nearly identical.

is diamagnetic. The contact hyperfine coupling of vacuum muonium is 4463 MHz [53]. The muonium contact couplings in most solids are between 1000 and 4700 MHz [54] although shallow donors with extremely small contact couplings have been found [54], for example in CdS [55] and in ZnO [56]. There may also be a small superhyperfine interaction due to the overlap of the muonium wavefunction with some of the surrounding nuclei.

The experimental spectroscopy of muonium is not part of this thesis and will therefore not be discussed here. However, some muonium sites and contact couplings were calculated in a series of fluorides and will be discussed in Chapter 4.

- In metals there could be a contact hyperfine coupling of the type described above between the muon and the polarised conduction electrons which, in turn, may be coupled to localised moments *via* the Ruderman-Kittel-Kasuya-Yosida (RKKY) mechanism. This coupling will not be discussed here.

While in general the coupling of the muon is complicated, all of the systems considered here, where couplings were calculated explicitly, are antiferromagnetic insulators and therefore only the dipolar term in Eq. 2.10 and the contact coupling in Eq. 2.13 need to be considered.

A fundamental limitation of the μ^+SR technique is immediately obvious from the discussion above: *the site of implantation of the muon as well as the extent to which it perturbs its environment is not known experimentally.* This is one of the key questions addressed in this thesis and will be discussed in more detail in Chapter 4.

2.6 Polarisation functions

The previous section concerned the magnetic coupling of a muon implanted into a sample. In this section I discuss the consequences of this coupling for the time-evolution of the muon spin in zero-field (ZF), applied longitudinal field (LF) and transverse field (TF). A great variety of polarisation functions exist, each corresponding to a particular physical situation and each using different approximations. This discussion will be kept brief and will concentrate on the physical scenarios discussed in this thesis. A more comprehensive discussion can be found, for example, in Ref. [48].

The simplest case to consider is that of a muon initially polarised along z in a magnetic field $\mathbf{B}$ at an angle θ to the z-axis. This is referred to as the *longitudinal geometry* since the polarisation along the initial direction of muon spin polarisation is measured. The time evolution of the projection of the muon spin onto the z-axis, $P_z(t)$, is then given by

$$P_z(t) = \cos^2\theta + \sin^2\theta \cos\omega t, \tag{2.14}$$

where $\omega = \gamma_\mu |\mathbf{B}|$ (γ_μ is the muon gyromagnetic ratio). This may correspond to the experimental scenario of a muon experiencing a dipolar field in an ordered magnet. In the case of an unaligned polycrystalline sample, a suitable powder average of Eq. 2.14 yields

$$P_z(t) = \frac{1}{3} + \frac{2}{3}\cos\omega t, \tag{2.15}$$

since there are two spatial directions perpendicular to z and only one parallel to it. The spontaneous appearance of oscillations in the asymmetry is usually an

unambiguous sign of magnetic order in the sample[7]. The rise of the baseline due the '1/3 tail' in Eq. 2.15 is an additional piece of evidence that a symmetry has been spontaneously broken. Example experimental data are given in Fig. 2.4 for the coordination polymer $[Cu(pyz)_2(pyO)_2](ClO_4)_2$.

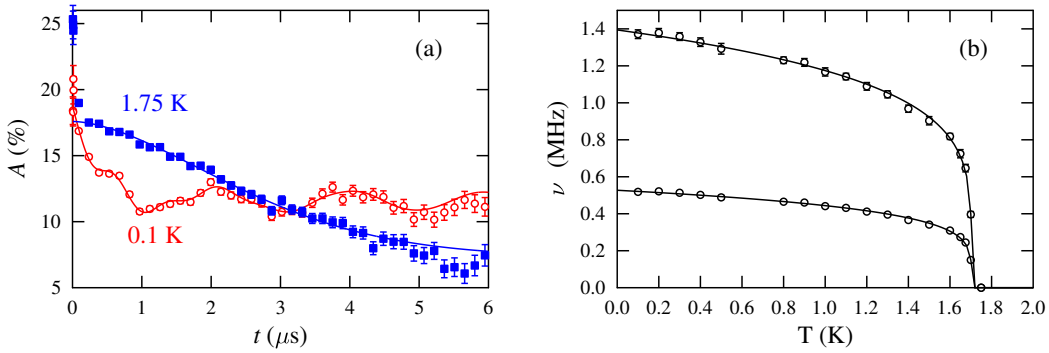

Figure 2.4: Experimental μ^+SR data for the coordination polymer $[Cu(pyz)_2(pyO)_2](ClO_4)_2$. (a) Asymmetry at 0.1 and 1.75 K. Note the rise in the baseline for the 0.1 K data set due to the '1/3-tail'. (b) Plot of fitted oscillation frequencies versus temperature clearly showing the magnetic transition at 1.70(5) K.

However, spatial or temporal variations in the local field will cause these oscillations to dephase and the ensemble spin polarisation to relax. The dephasing can usually be described by a Gaussian envelope $\exp(-\gamma_\mu^2\langle B^2\rangle t^2/2)$ for a *static* mean square field width $\langle B^2\rangle$ while an exponential distribution is more apposite for dynamically fluctuating fields $\exp(-\lambda t)$ (see discussion below).

2.6.1 Transverse geometry

The transverse geometry is well-studied due to its importance in nuclear magnetic resonance (NMR). Here the transverse polarisation P_x is measured instead of the longitudinal polarisation P_z. A magnetic field B_0 is applied along the z-direction.

[7]Although an interesting exception is discussed in Chapter 4.

The general solution for a field fluctuating with correlation time τ_c and of mean square width $\langle B^2 \rangle$ is known as Abragam function [57] and is given by

$$P_x(t) = \exp\left[-\gamma_\mu^2 \langle B^2 \rangle \tau_c^2 (e^{-t/\tau_c} - 1 + t/\tau_c)\right] \cos \omega_0 t, \tag{2.16}$$

where $\omega_0 = \gamma_\mu B_0$[8]. In the static limit when $t/\tau_c \to 0$

$$P_x(t) = \exp\left[-\frac{1}{2}\gamma_\mu^2 \langle B^2 \rangle t^2\right] \cos \omega_0 t, \tag{2.17}$$

while in the *fast-fluctation limit* where $t/\tau_c \to \infty$

$$P_x(t) = \exp\left[-\gamma_\mu^2 \langle B^2 \rangle \tau_c t\right] \cos \omega_0 t. \tag{2.18}$$

Note that in the fast fluctuation limit the relaxation rate $\lambda = \gamma_\mu^2 \langle B^2 \rangle \tau_c$ decreases for faster fluctuations (smaller τ_c). This counter-intuitive effect is known as *motional narrowing* (since the width of the line narrows in the frequency-domain) and is also present in the longitudinal case (see below).

2.6.2 Longitudinal geometry

Consider a statically disordered system in zero field. The magnetic field at any given point will take a random value. By the central limit theorem we may approximate the field distribution with a normal distribution about zero. The resulting longitudinal relaxation function was first found by Ryogo Kubo and

[8] There may be shift of this frequency from the pure diagmagnetic line, for example due to the interaction of the muon with the conduction electrons in metals, which is known as *Knight shift* and will not be considered here.

Toru Toyabe [58; 59] and is given by

$$P_z(t) = \frac{1}{3} + \frac{2}{3}\exp\left(-\frac{1}{2}\gamma_\mu^2\langle B^2\rangle t^2\right)\left(1-\gamma_\mu^2\langle B^2\rangle t^2\right). \tag{2.19}$$

The ZF Kubo-Toyabe function is shown in Fig. 2.5, note that at early times it

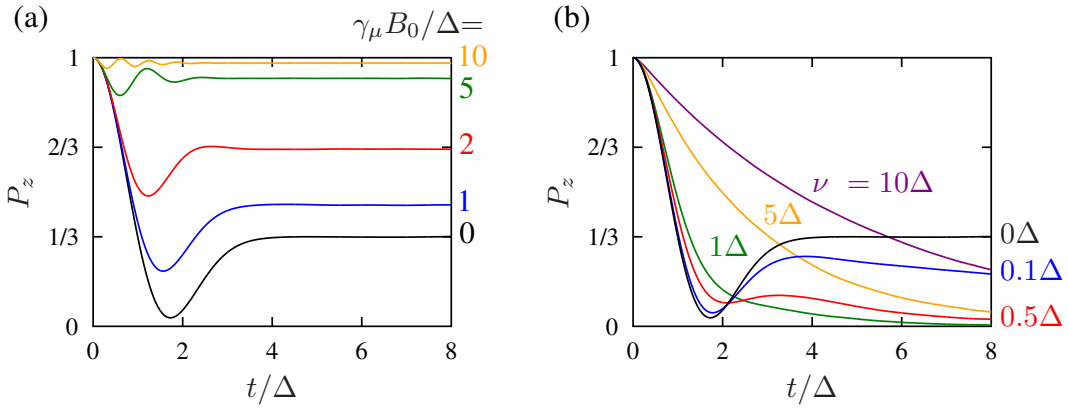

Figure 2.5: Kubo-Toyabe function (a) in an applied longitudinal field B_0 and (b) in the dynamic case. $\Delta = \gamma_\mu\sqrt{\langle B^2\rangle}$ is the second moment of the field distribution, and $\nu = 1/\tau_c$ is the fluctuation rate of the field. In the static case a rapid quenching of the relaxation is observed when $B_0 > \Delta$. The dynamic case illustrates motional narrowing in the fast fluctuation limit as well as the rapid quenching of the '1/3-tail' recovery at large times, that is present in the static limit.

approximates a Gaussian.

Let us now consider what happens in an applied longitudinal field and in case of dynamical fluctuation of the field. While analytic solutions do exist these are quite complicated, in particular for the dynamical case [59]. For this reason, I illustrate a numerical solution based on the density-matrix formalism [60] here. The density operator for a fully spin-polarised ensemble of muons at time $t = 0$ is given by

$$\rho(0) = |\uparrow\rangle\langle\uparrow| = \begin{pmatrix} 1 & 0 \\ 0 & 0 \end{pmatrix}, \tag{2.20}$$

its time evolution is given by

$$\rho(t_2) = U^{\dagger}(t_2, t_1)\rho(t_1)U(t_2, t_1), \tag{2.21}$$

where U is the time evolution operator

$$U(t_2, t_1) = \exp\left(-\frac{i\mathcal{H}(t_2 - t_1)}{\hbar}\right), \tag{2.22}$$

defined by the time-independent Hamiltonian

$$\mathcal{H} = -\mu_{\mathrm{B}}\,\boldsymbol{\sigma} \cdot \mathbf{B}, \tag{2.23}$$

where $\boldsymbol{\sigma} = [\sigma_x \sigma_y \sigma_z]$ represents the Pauli matrices and $\mathbf{B}$ is the field at the muon site. The internal field is taken to be normal distributed. In the case of a static field, the time evolution can be performed up to an arbitrary time t in a single step, even in the presence of an applied field. The calculation is repeated for many muons (here 100,000) with their local field normally distributed and added to the external field. The ensemble average at time t is then found from

$$P_z(t) = [\sigma_z] = tr(\rho(t)\sigma_z), \tag{2.24}$$

where tr is the trace operator. The resulting polarisation $P_z(t)$ is shown for a range of applied longitudinal fields in Fig. 2.5.

The dynamic case is treated within the *strong-collision model* [59]. Here a field fluctuation or, equivalently, a muon hop is described as follows. The field is taken to be constant up to some time t_{hop} when it changes suddenly to a random

normal-distributed value without any correlation[9] with the previous field. This is an example of a *Markov process*. The 'hop' takes place between time t and time $t + dt$ with probability

$$P(t) = \exp(-\nu t), \tag{2.25}$$

where $\nu = 1/\tau_c$ is the muon hop or field fluctuation rate. In the strong-collision model the time-evolution described in Eq. 2.21 is performed up to t_{hop} after which a new normal-distributed internal field value is chosen and the state is iterated until a chosen time t is reached. This process is repeated for a large number of muons (in this calculation 100,000) and the ensemble average given in Eq. 2.24 yields the desired polarisation $P_z(t)$. The results, shown in Fig. 2.5 for a range of fluctuation rates, illustrate motional narrowing in the fast fluctuation limit as well as the rapid quenching of the '1/3-tail' recovery at large times, that is present in the static limit. The latter is the cause why a Kubo-Toyabe relaxation is rarely observed in real systems, where residual magnetic dynamics are frequently present.

A dynamic relaxation is frequently exponential (or Lorentzian in NMR terminology) as illustrated by these calculations. However, in some cases an unusual static field distribution can give rise to a Lorentzian relaxation [61]. A distinction between static and dynamic relaxation is usually possible since the relaxation in the dynamic case is not easily quenched in an applied field unlike in the static case, where an external field of order $\Delta = \gamma_\mu \sqrt{\langle B^2 \rangle}$ rapidly quenches any relaxation. The application of a small longitudinal field therefore allows the nature of the relaxation mechanism to be identified.

[9] In real systems magnetic fluctuations *are* frequently correlated.

2.7 Conclusion

The basic principles of a μ^+SR experiment were introduced. μ^+SR has proven to be an extremely sensitive probe of magnetism, particularly in systems with very small magnetic moments, a recent example being the detailed study of the phase diagram of the quantum spin liquid κ-(BEDT-TTF)$_2$Cu$_2$(CN)$_3$ [33], as well as in low-dimensional systems, where correlations can appear well above the ordering transition that reduce the specific heat response to magnetic order [62], an example here being the detection of magnetic order below 110 mK in the magnetic chain compound copper pyrazine dinitrate using μ^+SR [63], which had remained elusive in specific heat measurements down to 70 mK [64]. μ^+SR has revealed important information about high-T_c superconductors [65], where it can, for example, be used to study the interplay of magnetism and superconductivity [66]. It frequently provides information that is complementary to other probes, such as magnetisation or susceptibility measurements[10], as well as neutron scattering and nuclear magnetic resonance measurements which probe dynamics on very different time scales [67]. One of the most fundamental limitations of the technique concerns the lack of information about the site at which a muon implants into a host and the perturbation it exerts locally on crystal and electronic structure. These are issues that cannot in general be addressed experimentally. A key part of this thesis is to develop and test methods based on density-functional theory to address the muon site problem in realistic scenarios.

[10] As will be illustrated in Chapters 5 and 6.

Chapter 3

Density-functional theory

Chemistry has come to an end.

Paul Dirac (1902-1984)

The quote above is famously attributed to Paul Dirac upon the spectacular spectroscopic validation of the Schrödinger equation for simple systems such as H_2 and He. "Too bad that in almost all cases, this equation is far too complex to allow solution", he is said to have added [68]. In this chapter I introduce *density-functional theory* (DFT) as a method to find approximate, but often very accurate solutions to the many body problem in solids. DFT is applied in Chapters 4 and 5, primarily to determine muon stopping sites from first principles as well as to understand the perturbation caused by the muon locally on the electronic and crystal structure of its host. This chapter is intended as a brief introduction to aspects of the technique that are particularly pertinent to the calculations performed in later chapters. A comprehensive introduction to DFT can be found in Ref. 69.

3.1 The correlated many-body problem

Consider an interacting many particle system described by the non-relativistic Schrödinger equation

$$\left\{ -\frac{\hbar^2}{2m} \sum_j \nabla_j^2 - \sum_{j,l} \frac{Z_l \, e^2}{|\mathbf{r}_j - \mathbf{R}_l|} + \frac{1}{2} \sum_{j \neq j'} \frac{e^2}{|\mathbf{r}_j - \mathbf{r}_{j'}|} - E \right\} \Psi(\mathbf{r}_1, \mathbf{r}_2, ..., \mathbf{r}_{\mathrm{N}}) = 0, \tag{3.1}$$

where $\mathbf{r}_j$ are the positions of the N electrons of mass m, E is the energy of the system, and $\mathbf{R}_l$ and Z_l are the positions and atomic numbers of the nuclei. $\hbar$ and e are the fundamental constants. An excellent simplification is the *Born-Oppenheimer* or *adiabatic* approximation where the nuclear and electronic degrees of freedom decouple due to the large nuclear mass and the nuclear kinetic energy can be neglected. In this approximation the positions of the nuclei are parameters and the nuclear-nuclear repulsion is not pertinent to the problem of electronic structure and has therefore been omitted. The many particle wavefunction Ψ depends on the positions and spins of all electrons (spins will not be indicated explicitly) and must obey the exchange principle $P_{jj'}\Psi = -\Psi$, where $P_{jj'}$ performs an odd permutation of the space and spin coordinates.

Early attempts at solving the Schrödinger equation for simple multielectron systems such as H_2 and He employed a variational approach, parameterizing the wavefunction and were very successful, see for example Ref. 70. Despite their success for sufficiently small systems, wavefunction-based attempts all encounter an "exponential wall" [68]: as the size of the system grows, the number of parameters required grows exponentially. A different approach is needed for systems with more than ~ 10 chemically-active electrons.

3.2 The Hohenberg-Kohn principle and the Kohn-Sham equations

The fundamental principle of DFT is that *any* property of a correlated many particle system can be expressed as a *functional of the ground state density* $n_0(\mathbf{r})$ (a functional turns a function into a scalar, for a example an integral is a functional). This is known as the *Hohenberg-Kohn* principle but though the existence proofs [71] for these functionals are surprisingly simple, they provide no guidance on the construction of such functionals.

The utility of DFT is due to the *ansatz* made by Kohn and Sham to replace the original many-body problem in Eq. 3.1 with an auxiliary independent-particle problem with an interacting density that can be solved more easily. In Hartree units, where $m = \hbar = 4\pi/\epsilon_0 = e = 1$, the self-consistent Kohn-Sham (KS) equations are [72]

$$\left\{-\frac{1}{2}\nabla^2 + V_{\text{ext}}(\mathbf{r}) + V_{\text{H}} + V_{\text{xc}}(\mathbf{r}) - \epsilon_j\right\}\psi_j(\mathbf{r}) = 0, \tag{3.2}$$

with

$$V_{\text{H}} = \int \frac{n(\mathbf{r}')}{|\mathbf{r} - \mathbf{r}'|} d^3\mathbf{r}', \tag{3.3}$$

$$V_{\text{xc}}(\mathbf{r}) = \frac{\delta}{\delta\tilde{n}} E_{\text{xc}}[\tilde{n}(\mathbf{r})]|_{\tilde{n}(\mathbf{r})=n(\mathbf{r})}, \tag{3.4}$$

$$n(\mathbf{r}) = \sum_{j=1}^{N} |\psi_j(\mathbf{r})|^2, \tag{3.5}$$

where $V_{\text{ext}}(\mathbf{r})$ is an external potential (which includes the nuclear Coulomb potential), V_{H} is the Hartree potential, ψ_j are the KS single particle wavefunctions with energies ϵ_j, $n(\mathbf{r})$ is the electron density, $\delta/\delta\tilde{n}$ denotes a functional derivative,

and $E_{\rm xc}[n]$ is the *exchange-correlation functional*.

The KS equations have to be solved self-consistently: one begins with an estimated $n(\mathbf{r})$ and then solves Eqs. 3.2 - 3.5 iteratively. Once convergence has been achieved, the ground-state energy is given by

$$E = \sum_{j=1}^{N} \epsilon_j + E_{\rm xc}[n(\mathbf{r})] - \int V_{\rm xc}\, n(\mathbf{r})\, d^3\mathbf{r} - \frac{1}{2} \int \frac{n(\mathbf{r}) n(\mathbf{r}')}{|\mathbf{r} - \mathbf{r}'|} d^3\mathbf{r} d^3\mathbf{r}'. \tag{3.6}$$

Note that the magnitude of the highest occupied ϵ_j relative to vacuum equals the ionisation energy. Furthermore, if we consider $V_{\rm xc}$ as an approximation to the electron self-energy, then ψ_j and ϵ_j are approximations to the Dyson orbitals and quasiparticle excitation energies, respectively.

3.2.1 The exchange-correlation energy

All many-body effects of exchange and correlation are contained within $E_{\rm xc}[n]$. The KS equations would yield the exact ground state energy and density if $E_{\rm xc}[n]$ were known exactly. Although no exact solutions for $E_{\rm xc}[n]$ are known, a number of approximations exist that are both accurate and sufficiently simple.

The simplest approximation is the *local density approximation* [72] (LDA), where the exchange-correlation energy per particle $\epsilon_{\rm xc}$ is approximated by that of a homogenous electron gas of density n, which can be calculated very accurately [73]

$$E_{\rm xc}^{\rm LDA}[n] = \int d^3\mathbf{r}\; n(\mathbf{r})\; \epsilon_{\rm xc}^{\rm unif}(n). \tag{3.7}$$

Although *a priori* only expected to be useful for electron densities resembling a homogeneous electron gas, the LDA is remarkably successful for a range of applications. Many of the shortfalls of the LDA can be corrected by including local

variations of the density[1]. This is done in the *generalized gradient approximation* (GGA) where

$$E_{\mathrm{xc}}^{\mathrm{GGA}}[n] = \int d^3\mathbf{r}\; n(\mathbf{r})\; \epsilon_{\mathrm{xc}}^{\mathrm{GGA}}(n, \nabla n). \tag{3.8}$$

There are a number of possible choices for $\epsilon_{\mathrm{xc}}^{\mathrm{GGA}}(n, \nabla n)$. The calculations reported here used the GGA functional of Perdew, Burke, and Ernzerhof [74]. Future calculations will employ hybrid functionals such as BLYP [75; 76].

3.3 Computational details

3.3.1 Structural optimisations

Some of the primary quantities of interest are the structural changes upon implantation of a muon in a sample, as well as the muon stopping site. These are ground state properties that can usually be obtained with high accuracy using DFT. Since the ionic positions $\mathbf{R_l}$ only enter the KS equations parametrically, the forces on the ions (and hence the muon) can be calculated efficiently on the basis of the Hellmann-Feynman theorem [77; 78], which states that if $\mathcal{H}$ is the Hamiltonian of a system, which depends on a parameter λ

$$\frac{\partial E_\lambda}{\partial \lambda} = \left\langle \psi_\lambda \left| \frac{\partial \mathcal{H}_\lambda}{\partial \lambda} \right| \psi_\lambda \right\rangle. \tag{3.9}$$

Hence it is not necessary to evaluate the total energy of the system $E_{\mathbf{R}}$ for a number of different $\mathbf{R}$ to calculate $\mathbf{F}$ from $\nabla_{\mathbf{R}} E_{\mathbf{R}}$, instead it is possible to obtain the force directly from a calculation for a single $\mathbf{R}$.

It is possible to treat the dynamical effects of nuclei, such as phonons, within

[1] However, in many cases the LDA is superior to the GGA, a fact that has been at least partially rationalised by the observation that the LDA satisfies a sum rule for the normalisation of a quantity called the exchange-correlation hole (while the GGA does not) [68].

the Born Oppenheimer approximation using a perturbative approach [79]. In Chapter 4 density-functional perturbation theory will be used to study the nuclear quantum effects due to the light mass of the muon.

3.3.2 Practical considerations

In all calculations employed here the wavefunctions and charge density were expanded using plane waves as basis functions. A sufficient plane wave and charge density cutoff up to which wavefunctions are expanded as well as a suitably-dense k-space grid need to be determined in a convergence test (looking for example at the convergence of forces on displaced ions). The k-space grid for efficient integration over the Brillouin zone is chosen as described by Monkhorst and Pack [80].

Calculations on charged cells were performed by applying a uniform background charge to neutralise the charge of the supercell. This is necessary as periodic boundary conditions were used in these calculations and the energy of an infinite lattice of charges diverges.

It is of great practical utility (meaning that the required cutoffs will be lower) to replace the real potential of the nuclei and the inner core electrons by an effective *pseudopotential*. Pseudopotentials are engineered to yield pseudowavefunctions that match their all-electron counterparts outside of a chosen core radius. Within the pseudisation radius the pseudowavefunctions are smoother than the all-electron ones, which greatly reduces the computational cost of the calculation. Pseudopotentials can be *norm-conserving* [81], meaning that the total charge density integrated inside the core radius yields the all-electron value or they can be *ultra-soft* [82], in which case the charge density inside the core radius needs to be augmented. For norm-conserving pseudopotentials the charge density cutoff is exactly four times the plane wave cutoff. Ultrasoft pseudopotentials require a

ratio significantly larger than four. Ultrasoft pseudopotentials can reduce the cost of the calculation significantly but they are not always available or they may not be compatible with certain codes[2]. The muon was modelled as a norm-conserving hydrogen pseudopotential in all calculations since cutoffs were largely dominated by the other atoms in the system.

Some of the calculations required the calculation of contact hyperfine couplings (discussed in Sec. 2.5). Since these require knowledge of the spin density and hence wavefunctions *within* the core region of the pseudopotential, the all-electron wavefunction needs to be reconstructed within the core. This is achieved using the *gauge-including projector augmented wave* (GIPAW) formalism [83; 84] as implemented in the GIPAW package, which forms part of the plane-wave Quantum ESPRESSO code [85] with which all of these calculations were performed.

[2]Often this is because pseudowavefunctions for ultrasoft pseudopotentials are not orthonormal, which leads to computational challenges.

Chapter 4

The quantum states of muons in fluorides

The most fundamental limitations of a muon-spin relaxation experiment can be the lack of knowledge of the implantation site of the muon and the uncertainty about the muon's perturbation of its host. In this chapter it is shown that electronic-structure methods can be used to accurately address these issues. I demonstrate that diamagnetic muons introduce significant short-ranged distortions in ionic insulators that would lead to systematic errors on magnetic moments determined by μ^+SR, and quantify these. Further, I show that the F–μ–F complex formed by muons in many fluorides can be understood as an exotic molecule-in-a-crystal defect with a zero-point energy larger than that of any naturally-occurring triatomic molecule. This demonstrates the importance of quantum effects on muon localization. This chapter is based on work published in Refs. 86 and 87.

4.1 Introduction

The utility of muons as microscopic magnetometers implanted into a sample suffers from two fundamental limitations. The first concerns the lack of knowledge of the site of implantation of the muon, which hinders the measurement of magnetic moments and a distinction between different magnetic structures using μ^+SR. The second unknown of a μ^+SR experiment is the extent to which the muon's charge and magnetic moment locally perturb the electronic structure, whether this is by perturbing the electronic charge density or through structural perturbations of the ions. This has led to increased concern within the muon community and beyond since μ^+SR is frequently employed in the study of systems that lie on the verge of ordering [33; 63; 88; 89] or where doping is a critical parameter [66; 90; 91].

From the very beginning of μ^+SR significant effort has been devoted to the determination of muon sites. In some materials a determination of interstitial muon sites was indeed possible thanks to accurate experimental studies of the muon frequency shift in an applied field [92], level crossing resonances [93; 94], by inspecting relaxation rates as a function of applied field [95; 96], or through the observation of quantum entanglement between the muon spin and a small number of surrounding nuclei (discussed in more detail below) [97; 98]. Nonetheless the number of examples where the muon site can be determined by experimental means alone is limited and even in those cases the experimental information about the muon site and the perturbation caused by the muon is usually incomplete. An improved understanding of the muon state in solids would not only benefit a more complete understanding of the nature of the muon response in a wide number of compounds, it could also enable a determination of magnetic moments and per-

haps even allow a differentiation between different magnetic structures. This information would be particularly valuable in a number of topical compounds where the observation of magnetic neutron scattering is challenging, such as compounds containing nuclei that strongly absorb neutrons, for example in iridates [61], or compounds with particularly small magnetic moments, for example frustrated and low-dimensional systems, where the moments are strongly renormalised by quantum fluctuations [99; 100]. Previous studies of muon states using electronic-structure methods have focussed on the paramagnetic states formed by muons and protons in semiconductors [99–107], for a review see Ref. 53. Electronic-structure methods have also been applied in the study of muoniated molecular radicals, see for example Ref. 108. Diamagnetic muon states (where the contact hyperfine coupling is negligible) have received considerably less attention, in spite of their greater utility in the study of magnetic materials. I present a detailed microscopic study based on density-functional theory (DFT) of the dia- and paramagnetic muon states in a series of fluorides, where detailed information about the geometry of the diamagnetic muon site is experimentally accessible, enabling an accurate comparison with *ab initio* predictions.

I study the series of non-magnetic ionic insulators LiF and NaF (rock-salt structure, $a = 4.03$ Å and 4.78 Å), CaF_2 and BaF_2 (fluorite structure, $a =$ 5.46 Å and 6.20 Å), and the antiferromagnetic (AFM) insulator CoF_2 (rutile-type structure, $a = 4.70$ Å and $c = 3.18$ Å). I show that diamagnetic muons cause significant short-ranged perturbations of the host, not limited to the fluorides bound in the F–μ–F state (indeed the distortion of the neighbouring cations can exceed that of the fluorides). This introduces systematic errors on magnetic moments in ionic insulators determined by μ^+SR, which I quantify. I study the quantum behaviour of the muon and the heavier proton in both charge states.

The research presented in this chapter was performed by myself with input from Davide Ceresoli, Nicola Marzari, Tom Lancaster, and Stephen Blundell.

4.2 Muon-fluorine entanglement

In host compounds containing fluorine, diamagnetic muons can couple strongly to the fluoride ions often forming linear F–μ–F complexes, [97] although bent F–μ–F and F–μ geometries have been shown to exist as well [98]. The magnetic dipolar coupling between muon and fluorine nuclear spins I (both $I = 1/2$) is described by the Hamiltonian

$$\mathcal{H}_{\mathrm{dd}} = \sum_{i>j} \frac{\mu_0 \gamma_i \gamma_j}{4\pi r^3} \left[\mathbf{I}_i \cdot \mathbf{I}_j - 3(\mathbf{I}_i \cdot \hat{\mathbf{r}})(\mathbf{I}_j \cdot \hat{\mathbf{r}}) \right], \tag{4.1}$$

where $\hat{\mathbf{r}}$ is the normalized vector connecting spins i and j, γ_i is the gyromagnetic ratio of spin i, r is the distance between spins i and j and all other symbols take their usual meaning. The observed property of a μ^+SR experiment is the polarization $D_z(t)$ of the muon ensemble along the initial muon spin direction z. Even in the absence of an external field the eigenstates of Eq. (4.1) are generally not eigenstates of the Pauli spin operator σ_q for a given direction q. This causes a time-dependence in the system's state, which is observed as an oscillation in the polarization $D_z(t)$. For a polycrystalline sample, $D_z(t)$ is given by [109]

$$D_z(t) = \frac{1}{N} \left\langle \sum_{m,n} |\langle m|\sigma_q|n\rangle|^2 \exp(i\omega_{mn} t) \right\rangle_q, \tag{4.2}$$

where $N = 2^M$ is the dimensionality of the Hilbert space of a system of M spin-1/2 particles, $|m\rangle$ and $|n\rangle$ are eigenstates of $\mathcal{H}_{\mathrm{dd}}$, and $\langle\rangle_q$ represents a suitable powder

average over all directions. $\mathcal{H}_{\mathrm{dd}}$ can be determined numerically for a given muon-fluorine configuration and the resulting polarization can be fitted to experimental data to determine to the experimental muon site geometry [97; 98].

4.3 Computational details

Unless indicated otherwise, calculations were performed in a supercell containing $2 \times 2 \times 2$ conventional unit cells. The charge state of the muon was determined by the charge of the supercell (+1 for diamagnetic and neutral for paramagnetic states). Total energies were converged to at least 2×10^{-12} Ry/atom (Ry is the Rydberg constant). Structural relaxations, total energies, band structures, and vibrational modes were calculated with wavefunction and charge density cutoffs of 80 and 320 Ry, respectively. A muon was placed in several randomly chosen low-symmetry sites and all ions were allowed to relax until the force on every ion had fallen below 10^{-3} Ry/a_0 (a_0 is the Bohr radius) and the energy change between subsequent steps had dropped below 10^{-4} Ry.

Contact hyperfine couplings were calculated using the projector-augmented wave (PAW) method [83] as implemented in the GIPAW package [85]. The PAW calculation required norm-conserving datasets with wavefunction and charge density cutoffs of 120 Ry and 480 Ry, respectively. The PAW datasets and cutoffs were also used for the calculation of the Löwdin charges used to estimate magnetic moments.

All calculations used a Gaussian broadening of the occupations of 0.01 Ry. Vacuum vibrational modes and hyperfine couplings were calculated in a $20 \times 20 \times 20$ Å^3 cell. No dispersion in k-space will be present for an isolated molecule in vacuum. Since no significant dispersion was observed the size of the unit cell was

sufficient (the values reported below were calculated at the Brillouin zone centre Γ).

To assess the accuracy of the structural relaxations for the chosen pseudopotentials and parameters of the calculation I have calculated the equilibrium lattice parameters and ionic positions for the bulk compounds by relaxing ionic positions and unit cell parameters. The calculated lattice parameters are all within 2% of the experimental values, demonstrating excellent convergence. The experimental values were used for subsequent calculations. By symmetry the ions cannot relax from their experimental positions in the bulk for LiF, NaF, CaF_2 and BaF_2. In CoF_2 the calculations yield a small relaxation of the fluorides by 0.037 Å with respect to their experimental positions [DFT: F site $(0.3024, 0.3024, 0)$, experimental F site: $(0.308, 0.308, 0)$]. Figs. 4.1, 4.3, and 4.4 below use the calculated fluoride positions for the bulk as reference. The unit cell was fixed during the structural relaxations which included the muon.

4.4 Diamagnetic states

4.4.1 Equilibrium geometries

The equilibrium geometries of the diamagnetic muon states obtained from a structural relaxation on a +1 charged supercell are shown in Fig. 4.1. The results predict the formation of linear F–μ–F states in all of the compounds of this series. This is in agreement with previous experimental data for non-magnetic LiF, NaF, CaF_2, and BaF_2 [97]. The calculated and experimentally measured bond lengths are tabulated in Table 4.1. Our calculated bond lengths are in all cases

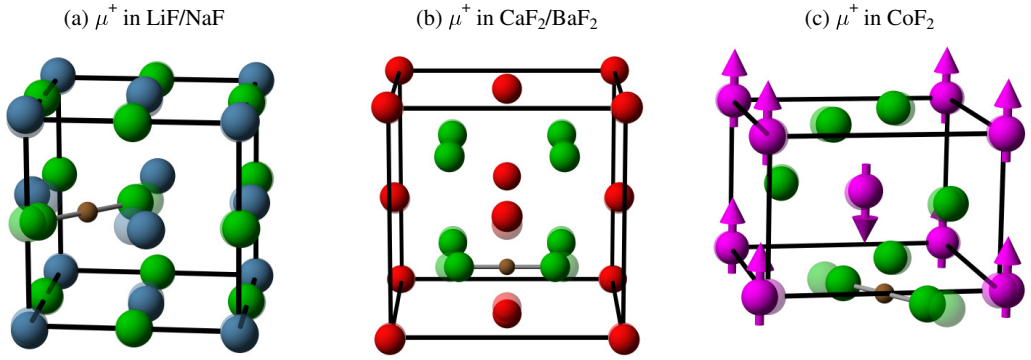

Figure 4.1: . Calculated equilibrium geometries of diamagnetic μ^+ muon states in LiF/NaF (Li/Na blue, F green), CaF_2/BaF_2 (Ca/Ba red), and CoF_2 (Co magenta). Translucent spheres represent the equilibrium ionic positions before the muon (brown) is introduced into the crystal. Black lines are a guide to the eye. The c-axis is vertical.

within 3% of the experimental values demonstrating the high level of accuracy of these results. The F–μ bond length of about 1.18 Å (calculated value for the F–μ–F^- molecule in vacuum) corresponds to approximately one ionic radius of the fluoride ion. The F–μ–F^- molecule can therefore be pictured as two hard spheres of fluoride ions that are just touching with the muon in between. I have found no evidence for any other stable diamagnetic states in this series.

For CoF_2 a detailed experimental study [92] has determined the muon site to be the octahedral $\frac{1}{2}00$ site, in agreement with our calculations, although no experimental reports of an F–μ–F state exist. In that experiment,[92; 110] the paramagnetic phase, where the potential F–μ–F signal would be present, was studied only under an applied magnetic field, impeding the observation of a potential F–μ–F signal. Following our first-principles results, I have therefore searched for experimental signatures of an F–μ–F state in CoF_2 in zero applied field.

A powder sample of CoF_2 (Sigma Aldrich 236128) was wrapped in 25 μm silver foil and mounted in a ^{4}He cryostat on the GPS instrument at the Paul Scherrer Institut in Switzerland. Above the critical temperature of 37.85 K, oscillations

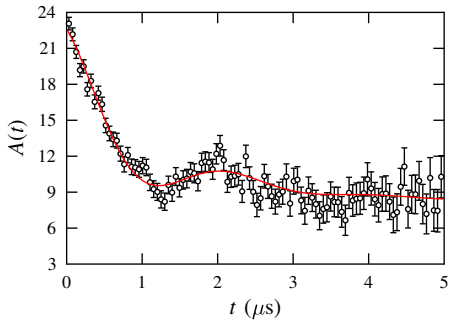

Figure 4.2: . Experimental muon decay asymmetry $A(t)$ at 70 K in CoF_2. The red line is the fit to Eq. 4.3.

in the muon decay asymmetry $A(t)$ characteristic of an F–μ–F state are present, see Fig. 4.2. The data were fitted to

$$A(t) = A_1 \exp(-\lambda_1 t) D_z(t) + A_{\mathrm{bg}} \exp(-\lambda_{\mathrm{bg}} t), \tag{4.3}$$

where $D_z(t)$ was determined by diagonalizing the Hamiltonian in Eq. 4.1 and solving Eq. 4.2. The procedure was iterated to find the F–μ–F geometry that yielded the best fit using a custom-written fitting program [111]. The second term in Eq. 4.3 accounts for a slowly relaxing background due to muons stopping in the cryostat tail or sample holder. The term $\exp(-\lambda_1 t)$ models residual magnetic dynamics in the sample with a fitted value of $\lambda_1 = 0.73(8)$ MHz at 70 K. The best fit is for a symmetric, linear F–μ–F state with a fluoride-fluoride separation of 2.43(2) Å, in very good agreement with our calculated value of 2.36 Å. The extracted F–μ–F geometry is not very sensitive to the precise choice of parameterization in Eq. 4.3 as it is dominated by the nature of the function $D_z(t)$ which encodes this geometry. The results in all of the compounds in this series demonstrate that DFT is a powerful tool for determining diamagnetic muon sites.

4.4.2 The perturbation caused by the muon

Using a supercell approach, it is also possible to quantify the extent of the perturbation of the implanted muon on its host. The calculated structures (Fig. 4.1) allow the study of the radial displacements of the ions as a function of their unperturbed distance from the muon site (Fig. 4.3). The calculated displacements demonstrate that the muon's perturbation is large but short ranged. While it is known that the perturbation of the fluoride ions must be significant based on the experimentally measured F–μ bond lengths of the F–μ–F states found in many fluorides [97; 98], these results allow the perturbation of the cations to be quantified for the first time. Since localized magnetic moments would be located on the cation, the cation displacements are particularly pertinent to understanding the effect of the muon's perturbation on experimentally measured μ^+SR spectra discussed below. These results show that in LiF, CaF_2, and BaF_2 the perturbation of the nearest neighbour (n.n.) cations even exceeds those of the fluoride ions bound in the F–μ–F state. At short distances the direct Coulomb interaction between the muon and the surrounding ions dominates over the elastic interaction transmitted through the lattice. Therefore similar distortions should be expected in *any* ionic insulator, regardless of whether fluoride ions are present or not. Indeed it is likely that the formation of the F–μ–F state somewhat mitigates the n.n. cation distortions due to the attraction of negative charge density towards the muon. At short distances all displacements are radially in- or outwards from the muon due to the symmetry of the site. Beyond the n.n. shell, elastic interactions cause some non-radial displacement.

I now discuss the effect of the muon's perturbation on experimental μ^+SR spectra. First, I have investigated the effect that the muon has on the magnetic moments of the surrounding ions. In this series only CoF_2 is magnetic.

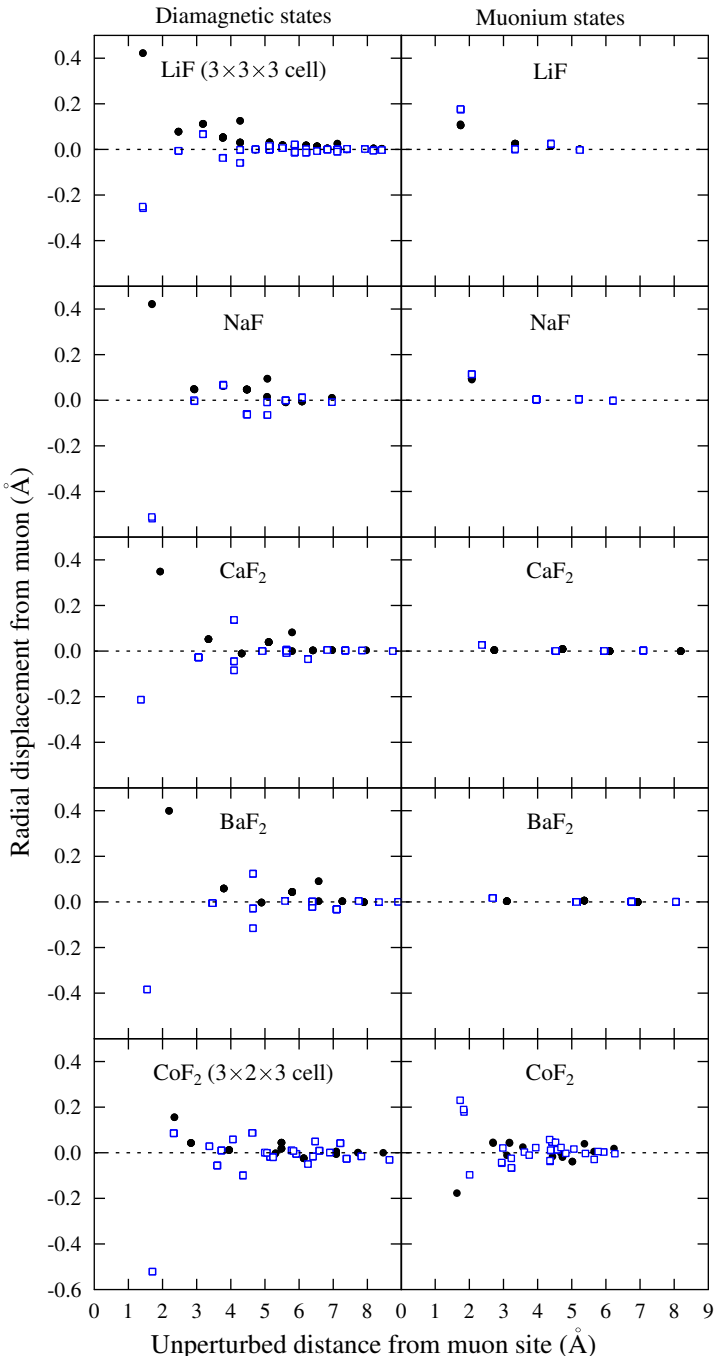

Figure 4.3: The radial displacements of the ions as a function of their distance from the muon site in the unperturbed crystal. Cation (black circle), fluoride (blue square). For all compounds the displacements are well converged already on a $2 \times 2 \times 2$ supercell but for LiF and CoF_2 the F–μ–F displacements are shown for larger cells.

The (unperturbed) spin-only moment was estimated from a Löwdin population analysis to be 2.68 μ_B per Co ion, while a simple integration of the absolute value of the spin density per supercell yields a spin-only Co moment of 2.81 μ_B. This compares with a total moment of 2.60(4) μ_B measured with powder neutron diffraction [112] and a spin-only moment of 2.21(2) μ_B determined from high energy photon diffraction [113]. The considerable reduction of the spin-only moment in CoF_2 from the ideal $S = 3/2$ value of 3 μ_B has been related [112] to the relative size of the E and D anisotropy constants, where the anisotropy term in the magnetic Hamiltonian is of the form $DS_z^2 + E(S_x^2 - S_y^2)$. Crystalline anisotropies are not reproduced accurately without explicit inclusion of spin-orbit coupling in the GGA functional. Since the functionals employed in this study did not include the spin-orbit coupling this is the likely cause for the overestimate of the spin-only moment in these calculations. A previous DFT study [114] also using the GGA has found a spin-only moment of 2.62 μ_B, consistent with my calculation.

The largest perturbation of the Co spin-only moment due to the presence of the *diamagnetic* muon in the site shown in Fig. 4.1 is found to be approximately $\pm 0.5\%$ and is therefore negligible. The perturbation of the total moment is likely to be similar and thus the perturbation of the magnetic moments in CoF_2 is unlikely to have any measurable effect on experimental μ^+SR spectra. My calculations also predict a spin-only moment of 0.026 μ_B on each fluoride ion that experiences a perturbation of up to ± 0.017 μ_B due to the muon. Since the fluorine moments are very small, they have been neglected in the calculation of the dipolar coupling with the muon below.

In general, the magnetic coupling of the muon is a sum of dipolar coupling, contact hyperfine interaction, demagnetising and Lorentz fields (see Sec. 2.5).

The calculated contact hyperfine coupling for the diamagnetic F–μ–F muon in CoF_2 is < 1 MHz and is negligible in comparison with the dipolar coupling. Furthermore in an antiferromagnet the demagnetizing and Lorentz fields are zero. Hence for the diamagnetic F–μ–F muon only the dipolar coupling $\mathbf{B}_{\rm dip}(\mathbf{r}_\mu)$ given in Eq. 2.10 needs to be considered[1]. $\mathbf{B}_{\rm dip}(\mathbf{r}_\mu)$ has been calculated for both an unperturbed crystal and an aperiodic perturbed crystal (simulating the presence of the muon). In the calculation of the dipolar coupling in the aperiodic perturbed crystal the perturbation of the crystal structure due to the muon was included within one supercell around the muon (with the muon at the centre), surrounded by unperturbed ions within a Lorentz sphere of 23 a lattice parameters. The perturbation of the magnetic moments has been neglected.

The calculations predict the structural perturbation due to the muon to reduce the measured dipolar coupling by 21.4% ($2\times2\times2$ supercell), 23.6% ($3\times2\times3$ supercell), 23.9% ($4\times2\times2$ supercell) compared to the unperturbed crystal. Experimentally the dipolar coupling is measured to be 16% lower [92] than expected from a Co moment of 2.64 $\mu_{\rm B}$. This is in reasonable agreement with our prediction and demonstrates that relaxed geometries obtained from DFT are suitable for calculating corrections to expected dipolar fields and hence, in principle, can be used to apply corrections to estimated magnetic moments measured by μ^+SR.

Note that the perturbation of the n.n. cations in CoF_2 is fairly moderate in comparison with the other compounds in this series (Fig. 4.3). Nonetheless the n.n. cation displacements in CoF_2 have a significant effect on the calculated

[1]There will be a quantum correction to the dipolar coupling which has not been included at this level of approximation. While a direct spin relaxation due to the quantum zero-point motion discussed in Sec. 4.4.3 is motionally-narrowed out from the spectra (see Sec. 2.6), such that only the average dipolar coupling is observed, there will be a quantum correction to this average due the finite muon wavefunction spread. There will also be a small shift in inter-atomic distances due to the muon zero-point motion, on the order of 0.03 Å for the hydrogen-fluoride bond length, see the discussion in Sec. 4.4.4.

dipolar coupling due to the short-ranged nature of the dipolar interaction. The short-ranged nature of the dipolar coupling can be illustrated by separately considering the dipolar coupling of the F–μ–F muon with the nearest neighbour (n.n.) and the remaining cations in the crystal: assuming a Co moment of 2.64 μ_B, the crystallographic distortion reduced the dipolar field from the two n.n. Co ions from -0.378 to -0.309 T, while the dipolar field from all other ions in the solid merely changes from 0.113 to 0.101 T (all along the c-axis and for the $2 \times 2 \times 2$ supercell). If the cations in the non-magnetic compounds LiF, NaF, CaF_2, and BaF_2 were magnetic and aligned antiferromagnetically (ferromagnetically) along the c-axis, the dipolar corrections for the F–μ–F states shown in Fig. 4.3 would be: LiF -39%(-70%), NaF -34%(-67%), CaF_2 0%(-46%), and BaF_2 0%(-47%). In the antiferromagnetic case, the muon would be located in a site of cancellation of the dipolar field in CaF_2 and BaF_2.

These results illustrate that in ionic insulators the muon's perturbation cannot be neglected if magnetic moments are to be determined accurately by μ^+SR. In more covalent compounds the μ^+ charge can be expected to be more screened and so structural distortions might be expected to be smaller. However, similar work on the coordination polymer $CuF_2(H_2O)_2$(pyrazine) [see Sec. 5.4] and on the organic radical magnet F4BImNN [115] shows that due to the relative 'softness' of many covalent materials, perturbations induced by a muon bonding to the atoms in the host can be just as large as those observed here or even larger.

4.4.3 Quantum effects

All of the results above are valid for a positive muon, a proton, or a deuteron defect and are 'classical' in the sense that they do not take account of quantum-mechanical zero-point effects due to the small muon mass ($m_\mu \approx m_p/9$). The

	$2r_{DFT}$	$2r_{exp}$	ν_{SS}	ν_{B}	ν_{B}	ν_{AS}	ZPE
$(FHF)^-$ exp.[a]	–	2.28	583	1286	1286	1331[b]	0.28
$(FHF)^-$ this work	2.36		581	1289	1289	1611	0.30
$(FHF)^-$ harm-MP2[c]	2.29	–	633	1334	1334	1280	0.28
$(FHF)^-$ NEO-MP2[c]	2.32	–	611	–	–	–	–
$(F–\mu–F)^-$	2.36	–	581	3797	3797	4748	0.80
LiF	2.34	2.36(2)[d]	–	2825	4603	4881	0.76
NaF	2.35	2.38(1)[d]	–	3071	4363	4813	0.76
CaF_2	2.31	2.34(2)[d]	649	2737	4481	5446	0.83
BaF_2	2.33	2.37(2)[d]	613	3033	4130	4974	0.79
CoF_2	2.36	2.43(2)	585	3076	3473	4570	0.73

Table 4.1: Calculated (DFT) and experimental (exp) properties of the diamagnetic F–μ–F states in solid and vacuum, and of the $(FHF)^-$ molecular ion in vacuum. r (Å) is the muon-fluoride bond length, ν is the frequency (cm^{-1}) of the symmetric stretch (SS), asymmetric stretch (AS), and bending (B) mode, and ZPE is the zero-point energy (eV). [a]Ref. 116. [b]Ref. 117 reports 1377 cm^{-1}. [c]Conventional MP2 calculations with harmonic treatment of the vibrational modes (harm-MP2) and NEO-MP2 calculation treating the nuclei on the same footing as the electrons [118] [d]Ref. 97.

quantum nature of nuclei is generally ignored in DFT calculations since nuclear masses are typically so large that quantum effects (caused for example by the difference in zero-point energy between two sites) are negligible since they lie below the current level of accuracy of the technique. The muon, however, is an exceptionally light impurity and quantum effects can therefore be expected to play a more significant role in the localisation of a muon than for the majority of conceivable point defects. I have used density-functional perturbation theory [79] (DFPT) to calculate the vibrational properties of the F–μ–F system in the solid and in vacuum (Table 4.1). In vacuum the linear $(F–\mu–F)^-$ anion has three distinct vibrational modes: symmetric stretch, bending (two-fold degenerate), and asymmetric stretch. Note that the agreement with the experimentally determined vibrational modes for the $(FHF)^-$ molecule is excellent, except for the asymmetric stretch mode. It is possible that this is due to a numerical error introduced

by the hydrogen getting too close to the core of the fluorine pseudopotential in this mode (see discussion below).

In the solid the two-fold degeneracy of the bending mode is broken due to the symmetry of the site: in LiF, NaF, CaF_2, and BaF_2 there are two fundamentally inequivalent directions of bending; one is towards a neighbouring cation and is shifted up in frequency while the other direction is into a 'gap' in the crystal structure and is shifted down in frequency. The asymmetric stretch is very similar to its vacuum value except in CaF_2, where the small bond length leads to a larger value. In CaF_2, BaF_2, and CoF_2 all F–μ–F modes are highly-localized and decouple from the lattice modes. The decoupling of the vibrational modes of the linear F–μ–F system illustrates that it may be viewed as a molecule-in-a crystal defect similar to the V_K center found in the alkali halides [119]. In LiF and NaF the symmetric stretch mode mixes with the lattice modes so this analogy is slightly less apposite. From the frequencies of the decoupled vibrational modes I have estimated the zero-point energy (ZPE) of the system (in the harmonic approximation). The muon-fluoride (or hydrogen-fluoride) bond is the strongest known hydrogen bond in nature [120] with a bond enthalpy of 565 kJ/mol (for HF) compared with 463 kJ/mol for the hydroxyl bond in OH [121]. Combined with the small mass of the muon this leads to the exceptionally large ZPE of the F–μ–F center of 0.80 eV in vacuum, which is larger than the ZPE of any natural triatomic molecule (the ZPEs of H_2O and H_3^+ are 0.56 and 0.54 eV respectively [122]). This demonstrates the importance of quantum effects in muon localization. Note that in the case of the fluorides discussed above the structural relaxation yields only a single candidate muon site, that is the muon can relax from any other site into the stable F–μ–F state. Hence in the case of the fluorides studied here the ZPE has no effect on the stability of the site. Other scenarios are feasible, where the

muon has a choice of local minima and where the ZPE could have a substantial effect on the relative stability of various candidate sites.

4.4.4 Comparison with other work

Also shown in Table 4.1 are the results of calculations using a different *ab initio* method known as second-order Møller-Plesset perturbation theory (MP2) [118], which is a post-Hartree-Fock method not uncommonly applied in computational chemistry codes for small systems but not usually applied to calculations in solids. Swalina and Hammes-Schiffer [118] have applied both the conventional MP2 formalism as well as a modified version called NEO-MP2, where NEO stands for nuclear-electronic orbital, to calculate the bond lengths and vibrational modes of *vacuum* $(FHF)^-$. In the conventional case the frequencies are calculated using the harmonic approximation and nuclear quantum effects are not taken into account for the calculation of the bond length. The NEO-MP2 method takes a fuller account of the quantum properties of the nuclei than the adiabatic approximation employed by us since it treats them on an equal footing with electrons. Swalina and Hammes-Schiffer's results predict an increase in the F–F separation by 0.03 Å which is worse compared with the experimental value than their conventional MP2 result, though the bond length is somewhat closer than our calculated value. The harmonic approach employed by us would not predict any increase in bond lengths for which anharmonic terms in the potential are required. The calculated vibrational frequencies of Swalina and Hammes-Schiffer are only better for the asymmetric stretch mode, where our calculations may have been hindered by technical problems (see discussion above). Note also that neither the MP2 nor the NEO-MP2 method can readily be applied in a solid, and that the difference between the MP2 and the NEO-MP2 results is, at least for $(FHF)^-$, on

the same scale as numerical differences between different functionals. The level of improvement expected from a NEO treatment of nuclear quantum effects is therefore, at least in this system, below the level of accuracy of DFT.

A similar method to treat light nuclei such as hydrogen and the muon on the same footing as an electron was applied in Hartree-Fock calculations of vacancy-containing defect complexes in diamond with some success [123]. A full treatment of nuclear quantum effects within state-of-the-art DFT, however, is likely to be only possible within the path-integral molecular dynamics (PIMD) formalism [124] or more recent improvements thereof [125]. Some attempts at using PIMD to study muonium in Si [102; 104; 106] and diamond [107] have been made.

Shortly after the publication of the work presented here in Ref. [86], Bernardini *et al.* published a similar study [126] of the diamagnetic states in LiF and YF_3. Their structural results for LiF are consistent with the results above with a calculated F–μ–F bond length of $2r = 2.3$ Å. Bernardini *et al.* have also estimated ZPEs for the diamagnetic muon by solving the Schrödinger equation for the muon in the electrostatic potential of the unperturbed host. This has the advantage that it is computationally approximately a factor of $3N$ (N being the number of atoms) cheaper than the estimate based on DFPT presented above. However, Bernardini *et al.*'s approximation neglects the muon–ion coupling and hence their results differ somewhat from the results presented above with the ZPE of the muon being estimated to be 0.5 eV in LiF and 0.15 eV in YF_3. For a *molecular defect* such as the F–μ–F center, the methodology based on DFPT provides more accurate results than that used by Bernardini *et al.*, as evidenced by the comparison with the $(FHF)^-$ molecular ion in Table 4.1.

4.5 Muonium

4.5.1 Equilibrium geometries

I now discuss the properties of neutral muonium (Mu) in this series of fluorides. The calculated equilibrium geometries obtained for a neutral supercell are shown in Fig. 4.4. Since the muon charge is screened by an electron, the Mu site is fundamentally different to the diamagnetic site. In LiF and NaF, Mu occupies the tetrahedral interstitial site. An interstitial site was previously suggested based on the observed hyperfine coupling [127]. In CaF_2 and BaF_2, Mu occupies the octahedral cation-cation centred site and the fluoride-fluoride centred octahedral site is unstable. In CoF_2 a single Mu site in a nearly octahedral position at approximately (0.56, 0.84, 0.50), distorted by the neighbouring fluoride, is predicted.

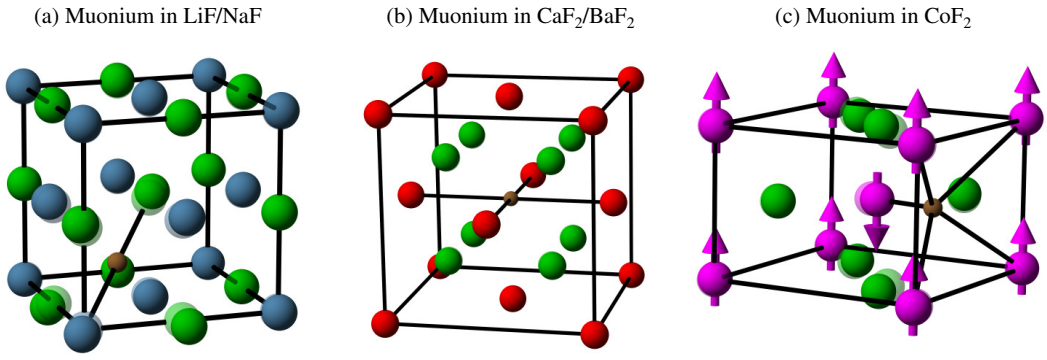

Figure 4.4: . Calculated equilibrium geometries of the neutral muonium states in LiF/NaF (Li/Na blue, F green), CaF_2/BaF_2 (Ca/Ba red), and CoF_2 (Co magenta). Translucent spheres represent the equilibrium ionic positions before the muon (brown) is introduced into the crystal. Black lines are a guide to the eye. The *c*-axis is vertical.

4.5.2 The perturbation caused by the muon

Fig. 4.3 shows the radial displacements of the ions from the Mu defect. Due to the screening effect of the Mu electron, the displacements are generally much smaller than for the diamagnetic μ^+. In LiF, NaF, CaF_2, and BaF_2 the displacements of the n.n. ions are again along the radial direction due to the symmetry of the Mu site and the ions are only displaced away from the Mu. In CoF_2 the symmetry of the Mu site is lower, leading to small displacements in the tangential direction, even for the n.n. shell, through elastic interactions with the lattice. These are also the likely cause for the effective attraction of some ions despite the neutral charge state of Mu. All of this also applies to neutral interstitial hydrogen H_i^0.

The paramagnetic state is experimentally characterized by the (dipolar and contact) hyperfine coupling between the muon (proton) spin and the surrounding spin density. For all paramagnetic states above, except the one in CoF_2, the dipolar coupling cancels by symmetry. Unlike in the diamagnetic case, the n.n. Co spin-only moment *is* significantly perturbed (-25%) by the presence of the Mu. The dipolar coupling was estimated as above by assuming coupling to localized Co moments only. The Co moment was assumed to be 2.64 μ_B and the perturbation of the n.n. moment was taken to be -25% (the calculated reduction of the spin-only moment). The perturbation of the spin-only moments of the other Co ions in the supercell was negligible. Crystallographic distortions were taken into account as above. At different levels of approximation the dipolar coupling of muonium in CoF_2 is 0.49 T (unperturbed crystal), 0.72 T (crystallographic distortions only) and 0.52 T (crystallographic distortions and perturbation of the n.n. Co moment), all are along c and have the same sign as the contact coupling (see below).

The contact hyperfine coupling A is related to the unpaired spin density $\rho(\mathbf{r}_n)$

		A	E_{HA}	$\langle A\rangle_{\mathrm{HA}}$	E_{FD}	$\langle A\rangle_{\mathrm{FD}}$	A_{exp}
Vac.	Mu	4711	–	–	–	–	4463
	H_i^0	1480	–	–	–	–	1420
LiF	Mu	4368	0.50	4256	0.51	4238	4584[a]
	H_i^0	1372	0.18	1361	0.17	1360	1400[b]
NaF	Mu	4389	0.38	4293	0.42	4208	4642[a]
	H_i^0	1379	0.13	1371	0.14	1367	1500[c]
CaF_2	Mu	4610	0.31	4564	0.33	4564	4479[d]
	H_i^0	1448	0.10[e]	1440	0.10	1440	1464[f]
BaF_2	Mu	4605	0.20	4560	0.23	4565	–
	H_i^0	1447	0.07	1440	0.07	1440	1424[g]
CoF_2	Mu	1281	0.62	1397	0.59	1535	–[h]
	H_i^0	403	0.21	420	0.20	441	–

Table 4.2: Calculated and experimental contact hyperfine couplings (MHz) and zero-point energies E (eV) of Mu and H defects. A: 'classical' hyperfine coupling; $\langle A\rangle$: quantum corrected value using the harmonic approximation (HA), by solving the full Schrödinger equation using finite differences (FD). [a]Ref. 127. [b]Ref. 128. [c]Ref. 129. [d]Ref. 130. [e]Measured [131] to be 0.12 eV at 100 K. [f]Ref. 132. [g]Ref. 133. [h]While no experimental value A_{exp} has been reported for CoF_2, a total coupling of 1280 MHz has been measured [134] in MnF_2. The dipolar coupling (without quantum correction) in CoF_2 is $\approx$ 71 MHz (0.52 T along c) and adds to the contact term.

at the muon/proton position $\mathbf{r}_n$ *via*

$$A = \frac{2\mu_0}{3}\gamma_e\gamma_n\rho(\mathbf{r}_n), \tag{4.4}$$

where γ_e is the electron gyromagnetic ratio and γ_n is the muon/proton gyromagnetic ratio, see Sec. 2.5. The spin density was obtained using the projector-augmented wave reconstruction method [83] and the resulting contact hyperfine couplings for 'classical' Mu are shown in Table 4.2 and compared to a wide range of available experimental data, partly measured for muonium by μ^+SR and partly measured for interstitial hydrogen by electron paramagnetic resonance. Note that at this level of approximation, the results do not depend on particle mass. The excellent agreement between predicted and observed hyperfine couplings demon-

strates the high level of accuracy of DFT in the calculation of the properties of hydrogenic defects in these systems.

4.5.3 Quantum effects

As for the diamagnetic muon states the small muon mass can be expected to give rise to a substantial ZPE and hence quantum spread of the defect wavefunction leading to a quantum correction to the hyperfine coupling. While this correction can be expected to be relatively small in these systems given the already excellent agreement between calculated and observed hyperfine couplings, I have nonetheless made estimates of this effect, since it is difficult to quantify experimentally and there are only few existing theoretical estimates. Previous theoretical estimates concern muonium and proton defects in Si, Ge, and diamond [103; 105].

While a complete treatment would involve a parameterization of the full three-dimensional contact hyperfine coupling and potential energy surface to calculate the three-dimensional wavefunction [105], I have obtained an estimate of this effect as follows. The vibrational modes of the defect were calculated using DFPT as above and the potential energy and hyperfine coupling were calculated along the direction of the eigenmodes. Since the eigenmodes are mutually perpendicular, the motion along the three modes decouples and the wavefunction factorizes. I have then calculated the Mu and H_i^0 nuclear wavefunctions in two ways. The first is an anisotropic harmonic approximation where the wavefunction along each mode is the ground state wavefunction of the harmonic oscillator given by

$$\psi_{\mathrm{HA}}(\mathbf{r}) = \left(\frac{1}{R_1^2 R_2^2 R_3^2 \pi^3}\right)^{1/4} e^{-(r_1'^2+r_2'^2+r_3'^2)/2}, \tag{4.5}$$

where $r_i' = r_i/R_i$ is the distance from equilibrium along eigenmode i of angular

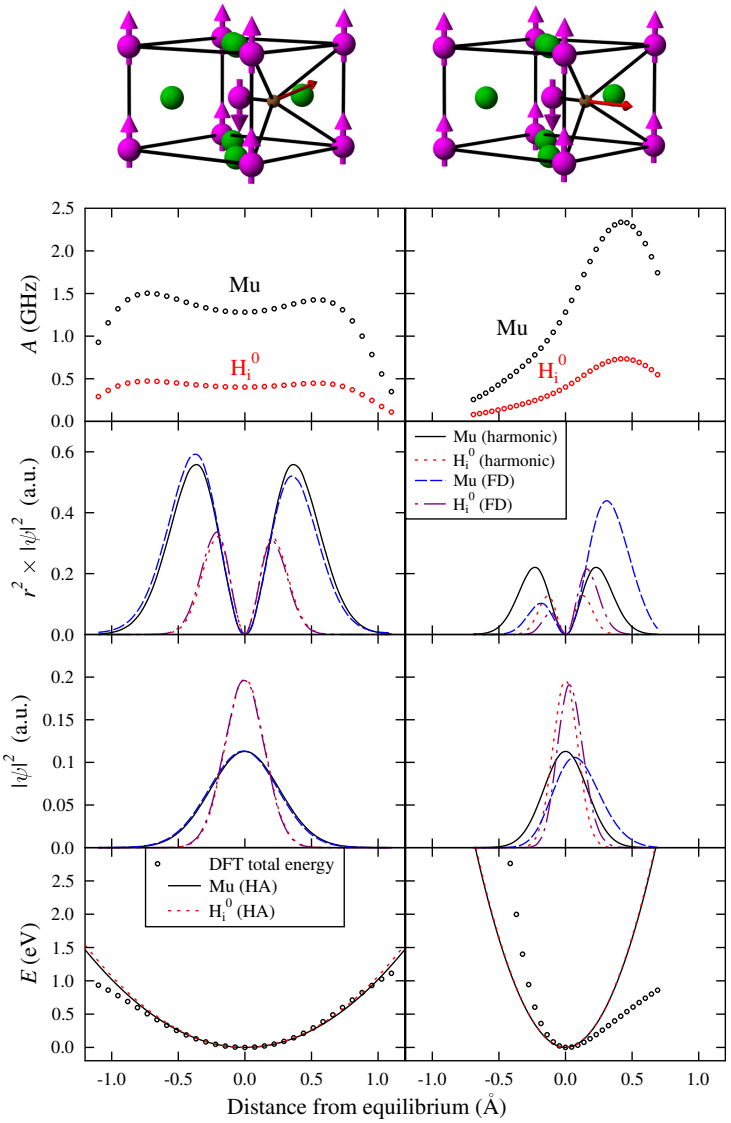

Figure 4.5: Quantum correction to contact hyperfine coupling using both the harmonic approximation (HA) and by solving the full Schrödinger equation using finite differences (FD) along two eigenmodes in CoF_2. From top to bottom: schematic of the eigenmode, the red arrow indicates displacement in positive direction; the contact hyperfine coupling for Mu (black) and H_i^0 (red); the wavefunction weighted by r^2; the normalized unweighted wavefunction for Mu (HA black; FD blue) and H_i^0 (HA red; FD purple); the potential energy above equilibrium calculated from the DFT total energy and the harmonic approximation to it for Mu and H_i^0. Note that while for the mode on the left the HA is quite reasonable, there are large deviations for the second mode.

frequency ω_i, normalized by the 'range' of the wavefunction $R_i = \sqrt{\frac{\hbar}{m\omega_i}}$ and m is the mass of the particle. Along each mode I have calculated the contact hyperfine coupling $A(\mathbf{r})$ and the total energy up to $3R_i$ from equilibrium in the positive and negative directions at equal spacings. The quantum average of the hyperfine coupling is then given by

$$\langle A \rangle = \frac{\sum_{i,j} (r_i^j)^2 |\psi(r_i^j)|^2 A(r_i^j)}{\sum_{i,j} (r_i^j)^2 |\psi(r_i^j)|^2}, \tag{4.6}$$

where i sums over modes and j is the step along each eigenmode. The calculated couplings $A(\mathbf{r})$ and nuclear wavefunction $\psi(\mathbf{r})$ are weighted by r^2 to obtain an approximate three-dimensional average. This approximation is accurate so long as $\psi(\mathbf{r})$ and $A(\mathbf{r})$ are approximately spherically symmetric, which I expect to be a reasonable approximation. This is illustrated in Fig. 4.5.

This *double adiabatic approximation* assumes that the motion of the electrons, the muon/proton, and the nuclei decouples. This a good approximation since the mass ratios of electron : muon and muon : lithium nucleus (the lightest of the nuclei involved) are approximately 1:207 and 1:61, respectively. For the proton these ratios are 1:1836 and 1:7 so the approximation holds less well than for the muon. Nonetheless, the ratio of the vibrational energies of the muon and the proton calculated using DFPT (which includes the ion–muon coupling) is close to $\sqrt{m_\mathrm{p}/m_\mu} \approx 3$ demonstrating that muon and proton modes are largely decoupled from the ionic motion in the geometries studied here, see Table 4.2.

Inspection of the potential energy surface has revealed significant anharmonic terms along some directions in some of the compounds, see Fig. 4.5. As a second method of estimating the quantum spread of the $\mathrm{Mu}/\mathrm{H}_\mathrm{i}^0$ nuclear wavefunction,

I have therefore also solved the full Schrödinger equation along the calculated mode directions using a finite differences method. The calculated total energies were taken to define the one-dimensional potential well $V(x)$ for the Mu/H_i^0. The Schrödinger equation given by

$$-\frac{\hbar^2}{2m}\frac{\partial^2\psi}{\partial x^2} + V(x)\psi(x) = E\psi(x), \tag{4.7}$$

where E is the energy of the particle, was then approximated by setting

$$\left.\frac{\partial^2\psi}{\partial x^2}\right|_{x=x_n} = \frac{\partial}{\partial x}\frac{\psi_{n+1/2} - \psi_{n-1/2}}{\delta x} = \frac{\psi_{n+1} - 2\psi_n + \psi_{n-1}}{(\delta x)^2}, \tag{4.8}$$

and hence reduces to

$$-t\left(\psi_{n+1} - 2\psi_n + \psi_{n-1}\right) + V_n\psi_n = E\psi_n, \tag{4.9}$$

where $t = \frac{\hbar^2}{2m(\delta x)^2}$ is a measure of the kinetic energy cost of localization within δx. Eq. 4.9 can be turned into matrix form and solved using standard diagonalization techniques. Periodic boundary conditions where $\psi_{N+1} = \psi_1$ for a system consisting of N grid locations along x were employed. The resulting wavefunction was used to calculate the quantum-corrected hyperfine coupling *via* Eq. 4.6.

The quantum corrections are tabulated in Table 4.2. The correction is smaller for the heavier and thus more localized H_i^0. As expected, the quantum corrections are indeed relatively small. Note however that there are significant differences between the quantum correction calculated using the harmonic approximation and that calculated using the finite-differences method. The latter should provide a more accurate estimate as it takes full account of anharmonicities in the potential.

The hyperfine couplings are somewhat underestimated for LiF and NaF and the quantum correction reduces them even further. The cause for this is likely a technical difficulty of the calculation. In LiF and NaF there is relatively little space for the interstitial Mu/H_i^0. Therefore part of the Mu/H_i^0 electron probability density overlaps with the core region of the fluorine and cation pseudopotentials, a problem that is aggravated when the muon/proton is displaced from the octahedral equilibrium position. This leads to an error in the contact hyperfine coupling. Unfortunately, this problem can only be overcome by reducing the core region of the pseudopotential, which would probably require treating more (and in the case of Li and F all) electrons as valence electrons, which in turn would require far higher charge density and wavefunction cutoffs to achieve satisfactory convergence. This has therefore not been attempted. Note that a related problem is observed for the asymmetric stretch mode of the F–μ–F and the $(FHF)^-$ molecule where the muon/proton gets very close to the fluoride, while no such problem is observed for the hyperfine coupling in CaF_2 and BaF_2, where the interstitial region is much larger.

Overall the final estimated hyperfine couplings for Mu and H_i^0 are within approximately 10% of the experimental value for LiF and NaF, the same level of accuracy as previous calculations in Si, Ge, and diamond [103; 105] and within 2% of the experimental value for CaF_2 and BaF_2.

4.6 Comparison with electrostatic potential

There has been considerable interest recently in identifying muon sites by locating the minima of the electrostatic potential of the unperturbed host (calculated at varying levels of complexity) [136–140]. In this section I compare the sites of

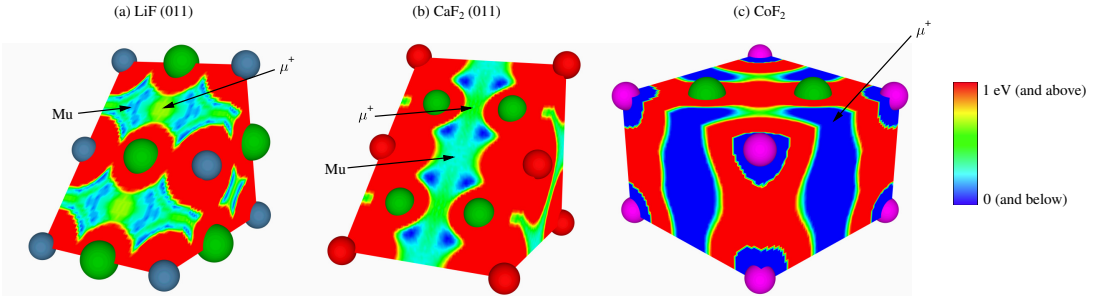

Figure 4.6: . Calculated electrostatic potential for the unperturbed solid. Blue coloring indicates regions that are attractive to a positive charge, red regions repel a positive charge. Below and above the end of the scale the color coding is blue and red, respectively, with no further gradient. The scale is relative and cannot be compared between different compounds. Li (blue), F (green), Ca (red), Co (magenta). The *c*-axis is vertical. Arrows indicate the dia- and paramagnetic muon sites obtained through a full relaxation, which agree with the experimentally determined muon sites. In CoF_2 the muonium site is close to the octahedral site that also hosts the diamagnetic muon. Note also that the muon ZPE, characterizing the extent of its delocalization in the absence of bonding, is about 0.8 eV in the F–μ–F state and about $0.2-0.6$ eV as muonium, see Tables 4.1 and 4.2. The data were visualized with the *VESTA* program [135].

the dia- and paramagnetic muons obtained through a full ionic relaxation with the location of the minima of the electrostatic potential of the unperturbed solid. The *electrostatic potential* is taken to mean the inverted sum of the conventional Hartree and ionic potentials (conventionally defined to be positive in regions that repel electronic charge density), see Chapter 3. The calculated electrostatic potentials are shown in Fig. 4.6 for three of the compounds of this series. It is evident that the minima of the electrostatic potential do not coincide in general with the correct dia- or paramagnetic muon sites. In the diamagnetic case this is due to the interaction of the muon with its host and in particular the formation of the molecular F–μ–F state which releases a substantial amount of energy upon formation. While interstitial muonium generally interacts more weakly with the host due to the screening by the Mu electron, this screening also makes muonium

less sensitive to the host's electrostatic potential and the site of muonium localization is mainly determined by the space required to accommodate the Mu electron. Note that muonium could also be located in a bond-centered rather than an interstitial location, in which case there usually is a significant interaction with the lattice [103; 105]. All of the compounds studied here are very ionic in character and the μ^+–lattice interaction is therefore expected to be stronger than in more covalent insulators or metals (where the μ^+ charge would at least be partially screened). Nonetheless we expect the combination of this screening (where operative), the muon-lattice interaction, and the muon's exceptionally large zero-point energy to frequently lead to muon localization away from the minima of the electrostatic potential of the unperturbed host. We therefore believe that muon sites cannot be determined reliably on the basis of the electrostatic potential alone.

4.7 Conclusions and outlook

In this chapter I have presented the first detailed study of the quantum states of dia- and paramagnetic muons in a series of fluorides, where experimental information on the diamagnetic muon site is available. In the next chapter this approach to studying the states of muons in solids is applied to a molecular magnet studied under applied hydrostatic pressure. We have recently published a similar study [115] accompanying experimental μ^+SR work on the purely-organic radical magnet F4BImNN. In F4BImNN the magnetic moment does not originate from any transition metal ion, but instead is due to an unpaired radical electron delocalised over the nitronyl-nitroxide group. DFT calculations of the muon's state in F4BImNN demonstrate that it has quite a dramatic effect on the local magnetic properties in F4BImNN since the muon bonds to one of the

molecules, pairing the radical electron and therefore almost completely destroys the magnetic moment locally. When this effect is taken into account, the calculated dipolar couplings are in good agreement with the experimental values for both F4BImNN as well as its non-fluorinated analogue BImNN, whereas if this effect is neglected the calculated couplings are out by an order of magnitude.

The results demonstrate that DFT can be used to comprehensively and accurately address the two most fundamental limitations of the μ^+SR technique: the problem of the unknown muon site and the perturbation exerted by the muon on its host. With the continuing improvements of electronic-structure methods and the growing performance of the computational resources available, muon states can be explored more accurately and in ever greater detail than ever before. It is hoped that this will become a routine part of many muon experiments and will boost the range of physical properties that can be explored with μ^+SR. A detailed understanding of the nature of the muon's state in solids is relevant beyond the field of μ^+SR since the muon acts as a light analogue of hydrogen, which is a ubiquitous impurity in all technologically important semiconductors, where it strongly affects the electronic and structural properties of the material [141]. In the longer term I hope to apply more advanced methods for treating the quantum properties of nuclei based on the path-integral molecular dynamics (PIMD) formalism [124] or more recent improvements thereof [125]. This could be applied for example to study the quantum tunnelling of muons established in KCl [142] and suggested to occur in the spin-ice material $Dy_2Ti_2O_7$ [143].

Chapter 5

A pressure-operated magnetic dimensionality switch

Much of the research in the area of molecular magnetism focusses on low-dimensional magnetic systems. In this chapter I discuss the interesting possibility of controlling the magnetic dimensionality in a molecular magnet by driving the system through a quantum critical point using applied pressure. I present the results of muon-spin relaxation measurements and high-field magnetisation experiments on the coordination polymer $CuF_2(H_2O)_2$(pyrazine) in pressures up to 22.5 kbar that demonstrate a transition from a quasi-two-dimensional to a quasi-one-dimensional antiferromagnetic phase driven by a rotation of the Jahn-Teller axis at 9.1 kbar. Antiferromagnetic ordering is observed in both regimes. The dimensionality switch is accompanied by a halving of the primary magnetic exchange energy J and a fivefold decrease in the ordering temperature T_N. Density-functional theory calculations of the spin density and muon sites as well as calculations of the dipolar anisotropy are used to complement the experimental data. Part of this chapter is based on work published in Ref. 144.

5.1 Introduction

Pressure plays a central role in the exploration of physical phenomena because it allows a controlled adjustment of structural parameters, such that their influence on electronic and magnetic properties can be studied. Recently a lot of work has focussed on studying the interplay of magnetism and superconductivity under applied pressures, see for example Refs. 145 and 146. While some examples exist [146] where pressure has quite a dramatic effect on the electronic properties of inorganic systems driving the system through a pressure-induced quantum critical point, commonly the energy scales in these systems are so large that changes with applied pressure tend to be limited to continuous changes in critical temperature and magnetic moment [145]. The relatively 'soft' metal-organic framework provided by transition metal coordination polymers on the other hand is much more sensitive to even relatively modest applied pressures. Some molecular magnets are based on hetero-ligand Jahn-Teller (JT) [147; 148] active metal centres, where the transition metal ion is located in a position of perturbed octahedral symmetry, surrounded by an asymmetric ligand environment. In such systems, each *trans*-coordinated ligand provides an additional degree of freedom on the JT-axis, meaning that small perturbations of the metal-ligand environment can be enough to rotate the JT-axis and radically modify the material's properties. It has recently been shown that it is possible to select the magnetic dimensionality of polymeric magnets at the synthesis stage [149]. In this chapter I demonstrate that pressure can be used to operate a Jahn-Teller driven magnetic dimensionality switch, between a two dimensional and a one-dimensional antiferromagnetic phase, in the extended Cu-based coordination network $CuF_2(H_2O)_2(pyz)$ (pyz = pyrazine, $C_4H_4N_2$). In this compound, hydrogen-bonding interactions,

a JT-active metal centre, and three different *trans*-coordinated ligands promote significant pressure-induced structural transitions. Together, these features enable the pressure-induced perturbation of the magnetic exchange, allowing the modification of the system's magnetic dimensionality.

The experimental work reported here has been published in Ref. 144. Author contributions: the μ^+SR experiment was performed by myself, Tom Lancaster, Fan Xiao, and Stephen Blundell with technical help from Alexander Maisuradze and Rustem Khasanov. All μ^+SR data analysis was performed by myself. The magnetisation measurements and data analysis were performed by Saman Ghannadzadeh and Paul Goddard with technical help from Stan Tozer and David Graf. The sample was prepared by John Schlueter. The density-functional and dipolar anisotropy calculations reported in Sec. 5.4 were performed by myself independent of the publication in Ref. 144.

5.2 Previous work on $CuF_2(H_2O)_2(pyz)$

$CuF_2(H_2O)_2(pyz)$ has a strongly anisotropic structure, consisting of Cu–pyz–Cu chains along the crystallographic *a*-axis, with the Cu^{2+} metal centres also joined together *via* a two-dimensional hydrogen-bonding lattice in the *bc*-plane, as shown in Fig. 5.1. The spin–1/2 Cu^{2+} ion is located at the centre of a distorted octahedron, surrounded by *trans*-pairs of Cu–O, Cu–F and Cu–N ligands. At ambient pressure the elongated JT-axis is oriented along the N–Cu–N bonds, implying that the $d_{x^2-y^2}$ orbitals and the directions of largest electronic overlap are directed perpendicular to this axis, and lie within the *bc*-plane. This situation is confirmed by pulsed-field magnetisation, electron-spin resonance (EPR), muon-spin relaxation, and density-functional theory calculations of the magnetic exchange

constants [150] showing that the compound displays highly two-dimensional antiferromagnetic behaviour ($J = 11.5$ K, secondary exchange energy $J_\perp \sim 10^{-4}J$) and undergoes long-range magnetic ordering below $T_\mathrm{N} = 2.6\,\mathrm{K}$. The primary magnetic exchange is mediated *via* the Cu–OH$\cdots$F–Cu spin exchange paths within the *bc*-planes, confirmed also by later DFT calculations of the spin density at 0 kbar [151]. The importance of the H$\cdots$F bonds in mediating exchange has also been investigated through selective isotopic substitution of hydrogen with deuterium [152]. Recent neutron scattering measurements have determined the magnetic order in the low-pressure phase to be collinear antiferromagnetism with an ordered moment of 0.60(3) μ_B along the [0.7 0.0 1.0] direction with an ordering wavevector [0.5 0 0], i.e. the magnetic unit cell corresponds to a $2\times1\times1$ supercell of conventional unit cells [153].

Synchrotron x-ray powder diffraction measurements by Halder *et al.* [154] have revealed that $CuF_2(H_2O)_2(pyz)$ undergoes two structural phase transitions as a function of pressure, accompanied by a rotation of the JT-axis and orbital orientations. The first, occurring at $P_\mathrm{c} \approx 10\,\mathrm{kbar}$, corresponds to a change of the elongated JT axis from the Cu–N to the Cu–O bond direction. This corresponds to a reorientation of the $d_{x^2-y^2}$ orbitals, from lying within the hydrogen-bonded *bc*-plane to the *ab*-plane — thus significantly decreasing the electronic overlap along the Cu-OH$\cdots$F-Cu bonds, while simultaneously increasing the magnetic orbital overlap along the Cu–pyz–Cu chains. Based on these observations and the behaviour of the susceptibility measured under applied pressure, Halder *et al.* [154] suggested that this would switch the magnetic dimensionality from quasi-two-dimensional (Q2D) to quasi-one-dimensional (Q1D). No sign of magnetic order above 2 K was detected in the suggested Q1D phase. A further pressure-induced change of the JT axis to the Cu–F direction, suggested to also correspond to one-

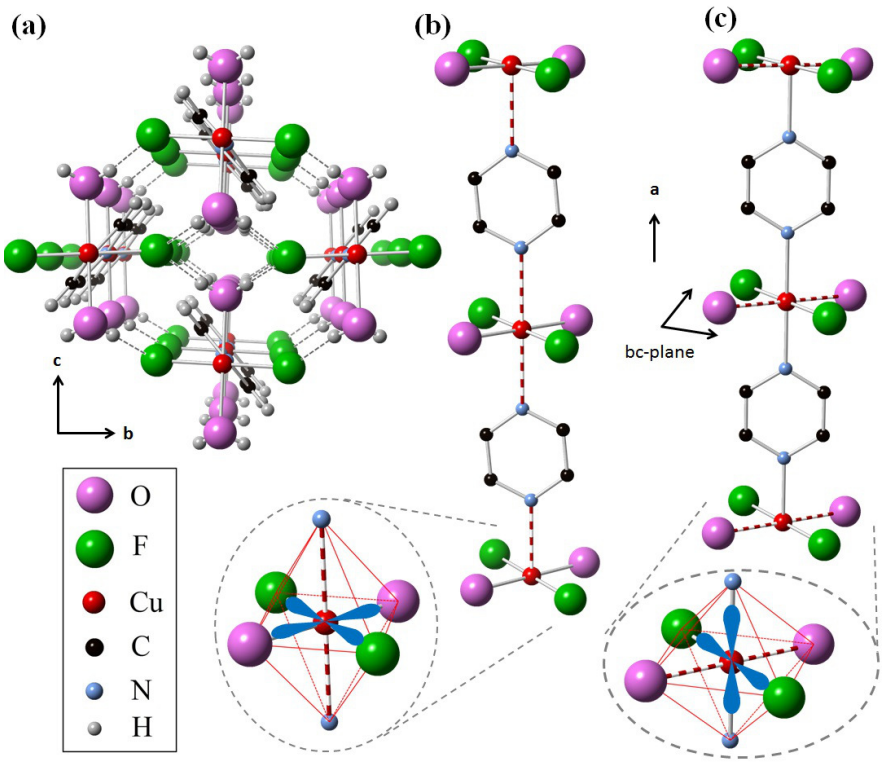

Figure 5.1: Crystal structure of $CuF_2(H_2O)_2(pyz)$ [150; 154], showing (a) the 2D hydrogen bonding network at ambient pressure. Hydrogen positions are approximate. Also shown is an isolated Cu–pyz–Cu chain at (b) ambient pressure and (c) 13.9 kbar, on the same scale. The JT-axis is shown by the red striped bonds. The zoomed-in regions show the JT octahedron, together with a representation of the magnetic orbitals, which provide the dominant exchange pathways.

dimensional spin-exchange along the Cu–pyz–Cu chains, was observed at 31 kbar. A second study [155] found a similar reorientation of the Jahn Teller axis and magnetic orbitals using single-crystal xray diffraction and electron paramagnetic resonance (EPR), although the critical pressure, estimated to be around 18 kbar, is in disagreement with the previous measurements.

Here a detailed study of the magnetic properties of $CuF_2(H_2O)_2(pyz)$ under applied hydrostatic pressure using μ^+SR and high-field magnetisation is reported. The μ^+SR results allow the changes in ordering temperature T_N under applied pressure to be tracked and demonstrate for the first time the existence of long-

range magnetic order in the Q1D phase. The transition to the Q1D phase is observed as a five-fold decrease in ordering temperature concomitant with a reduction of the number of precession frequencies from three to one and a halving of the observed (average) frequency. High-field magnetisation allows the changes in primary exchange coupling to be studied, which is found to halve at the transition. To further advance the understanding of the observed transition and the magnetism in both low- and high-pressure phases as well as to understand the state of the muons in the sample, I have performed DFT calculations of the spin density and the muon sites in both phases. Combined, these results provide unambiguous direct evidence for a switching of the magnetic dimensionality from Q2D to Q1D at a critical pressure of around 9 kbar. Further I present an argument based on dipolar anisotropies to explain the experimentally-determined direction of the magnetic moments in the low-pressure phase.

5.3 Muon measurements

5.3.1 Experimental details

A powder sample of $CuF_2(H_2O)_2(pyz)$ was pressed into a pellet to increase the packing efficiency and hence the signal from the sample. It was loaded into a piston cylinder cell with Daphne oil as pressure medium. A Cu-Be piston-cylinder cell was used for the measurements at 1 and 10.5 kbar, while a cell made from MP35 (a Ni-Co-Cr-Mo alloy) was used for the 4.8, 11.2, 14.8, and 22.5 kbar measurements. Both cells are paramagnetic and do not display hysteresis. The Cu-Be cell offers a simpler experimental background and a larger sample space (8 mm inner diameter) and thinner walls that stop less muons than the cell made from MP35 alloy (6 mm inner diameter). The Cu-Be cell therefore offers a better

signal to background ratio. In the Cu-Be cell approximately 50% of the signal originated from the sample compared with only 30% for the cell made from MP35 alloy. However, pressures above approximately 10 kbar at cryogenic temperatures can only safely be reached in the cell made from the stronger MP35 alloy.

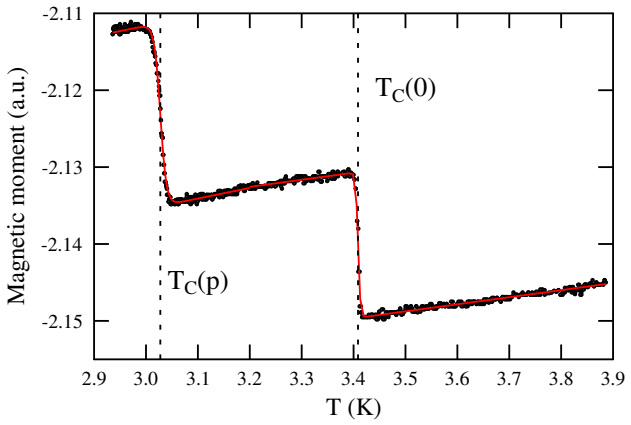

Figure 5.2: AC susceptibility measurement of the superconducting transition temperature in indium platelets placed inside the pressure cell at 10.5 kbar (lower transition) and outside of the cell (higher transition). The red line is a fit to a step function with a finite width, which was used to estimate the non-hydrostaticity across the indium platelet and the error on the pressure.

The pressure cell was pressurised at ambient temperature to a pressure (measured mechanically) of 1-5 kbar above the target pressure at cryogenic temperatures to account for thermal contraction. An accurate measurement of the achieved pressure was made by measuring the shift of the superconducting transition temperature T_c of a platelet of indium placed inside the cell with respect to the superconducting transition of an identical platelet placed outside the cell. The pressure inside the cell is then given by $P = [T_c(0) - T_c(p)]/0.0364$, where temperatures are in Kelvin and the pressure is in kbar. The critical temperature, T_c, was measured using a separate AC susceptibility setup. An example measurement is shown in Fig. 5.2. The indium platelets were approximately 10% of the sample size. The width of the transition is a measure of the non-hydrostaticity

of the pressure across the indium platelet and was used to estimate the errors on the measured pressures.

The pressure cell was mounted inside a ^{3}He cryostat on the GPD instrument at the Swiss Muon Source, Paul Scherrer Institut, and the sample was centred in the muon beam. GPD is the only muon instrument used for work reported in this thesis that allows the momentum of the muon beam to be tuned. This is essential as the available pressure cells have varying thicknesses and stopping powers. While all other instruments at ISIS and PSI employ *surface muons*, see Chapter 2, with fixed momentum of 29.8 MeV, the muons at GPD originate from pions that decay in flight.[1] Beam momenta of 100-110 MeV can be easily achieved this way, which is essential to penetrate the walls of the pressure cell. The beam momentum was chosen to maximise the signal from the sample.[2] Standard detector calibration of α was performed in an applied transverse field once the momentum was fixed. All muon data analysis was performed with a custom-written fitting program [111].

5.3.2 Experimental results

Detailed temperature scans were performed at six different pressures. Example μ^+SR spectra are given in Figs. 5.3(a-c). Within the low-pressure regime, we observe oscillations at three frequencies below a critical temperature, which at approximately 1 kbar is 2.48(1) K. This is in agreement with previous ambient pressure measurements which found oscillations at three frequencies below 2.59(1) K [150]. In the low-pressure phase the data were fitted to

[1] Usually, somewhat confusingly, called *decay muons*.

[2] For the Cu-Be cell the optimum momentum was 105 MeV, for the MP35 cell it was 105.6 MeV. Without adjusting the momentum the signal would have been poor.

$$\begin{aligned} A(t) = & A_1 e^{-\lambda_1 t} \cos(2\pi\nu_1 t + \phi_1) \\ & + A_2 e^{-\lambda_2 t} \cos(2\pi\nu_2 t + \phi_2) \\ & + A_3 e^{-\lambda_3 t} \cos(2\pi\nu_3 t + \phi_3) + A_4 e^{-\lambda_4 t} + A_\mathrm{b}(t), \end{aligned} \tag{5.1}$$

where ν_i are the dominant oscillation frequencies due to long-range magnetic order of the sample, ϕ_i are constant phases, and the exponential term accounts for residual magnetic dynamics in the sample. The last term accounts for the signal from muons stopped in the pressure cell itself, and is well described by

$$A_\mathrm{b}(t) = \frac{1}{3} A_\mathrm{cell} + \frac{2}{3} A_\mathrm{cell} \exp\left(-\frac{1}{2}\Delta^2 t^2\right)\left(1 - \Delta^2 t^2\right), \tag{5.2}$$

where $\Delta = \gamma_\mu \sqrt{\langle B^2 \rangle}$ is the width of the internal field distribution in the cell and A_cell is the amplitude of the signal from the muons stopped in the cell (see Sec. 2.6.2). For all fits, the ratios $A_1 : A_2 : A_3$ and $\nu_1 : \nu_2 : \nu_3$ were fixed to $4 : 2 : 1$ and $1 : 0.65 : 0.55$, respectively, as in Ref. [150]. The evolution of the fitted oscillation frequencies is given in Fig. 5.3(d-f). In the low-pressure phase, T_N is found to *decrease* with application of pressure [see Fig. 5.9(e)].

At 11.2 kbar and above there is no discontinuous change in the μ^+SR spectra above 1 K, indicating the absence of long range order above 1 K. However, below 630 mK (at 11.2 kbar) oscillations at a single frequency appear in the asymmetry [Figs. 5.3(c,f)], demonstrating the existence of long-range magnetic order in the high-pressure phase. For $P \geq 11.2$ kbar the data can be described succesfully by

$$A(t) = A_5 e^{-\lambda_5 t} \cos(2\pi\nu_5 t) + A_6 e^{-\lambda_6 t} + A_\mathrm{b}(t). \tag{5.3}$$

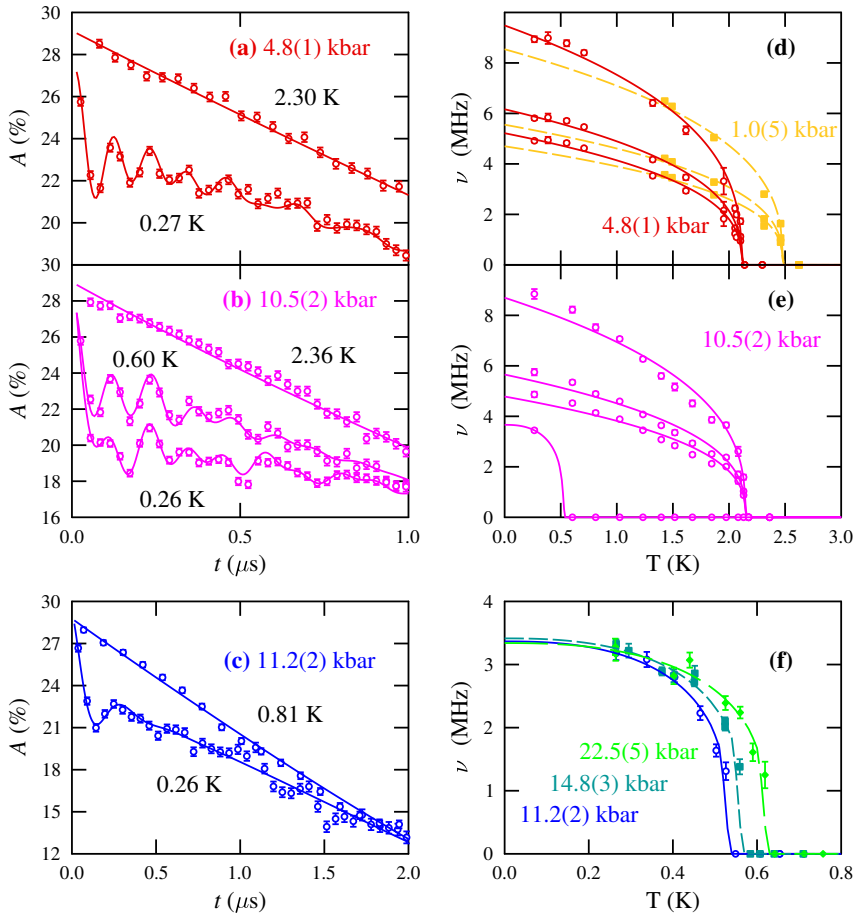

Figure 5.3: Time evolution of the μ^+ decay asymmetry $A(t)$ in (a-b) the low pressure regime, and (c) the high pressure phase. Also shown are (d-f) the fitted oscillation frequencies $\nu(T)$. Three frequencies were dominant in the low pressure regime, while the higher pressure phase was well described by a single frequency. The lines in (d-f) represent fits to $\nu(T) = \nu_0(1 - (T/T_N)^\alpha)^\beta$, where α and β were fixed to 1 (2.5) and 0.36 (0.3) in the Q2D (Q1D) phases, respectively.

In this phase T_N is found to *increase* with increasing pressure contrary to the behaviour in the lower-pressure phase. The change in T_N is found to be reversible upon reduction of pressure from 22.5 kbar to 11.2 kbar. Compared to a Q2D system, a Q1D system should be expected to have a much reduced long-range ordering temperature owing to the increased influence of classical and quantum fluctuations in one dimension. Therefore, the large decrease in T_N in the critical pressure region [Fig. 5.9(e)] is consistent with a transition to Q1D magnetic behaviour at high pressures. Also note the different temperature dependence of the oscillation frequencies in the Q1D and Q2D phases.

The data measured at 10.5(2) kbar display an interesting intermediate behaviour. All data measured down to 570 mK can be parameterised by just three oscillation frequencies, consistent in magnitude and number with the Q2D phase observed previously. At lower temperature however, a fourth frequency, consistent in magnitude with the Q1D phase appears unambiguously in the spectrum [see Fig. 5.3(c) and (e)]. This points towards the existence of a phase separation in the critical pressure region, an effect also seen in the magnetisation (see below). The data at 10.5(2) kbar could be parameterised by

$$\begin{aligned} A(t) =& A_1 e^{-\lambda_1 t}\cos(2\pi\nu_1 t + \phi_1) \\ &+ A_2 e^{-\lambda_2 t}\cos(2\pi\nu_2 t + \phi_2) \\ &+ A_3 e^{-\lambda_3 t}\cos(2\pi\nu_3 t + \phi_3) + A_4 e^{-\lambda_4 t} \\ &+ A_5 e^{-\lambda_5 t}\cos(2\pi\nu_5 t) + A_6 e^{-\lambda_6 t} + A_\mathrm{b}(t), \end{aligned} \tag{5.4}$$

where A_5 and A_6 were fixed to zero above the Q1D ordering transition around 0.5 K.

5.4 Density-functional theory calculations

In this section I present density-functional theory (DFT) calculations of the spin-density, the JT axes under pressure, and of the muon sites in $CuF_2(H_2O)_2(pyz)$; the latter were used to estimate the size of the ordered moment in the low-pressure phase. These calculations supplement the experimental μ^+SR data and provide valuable additional information about the nature of the magnetism in both phases.

Before discussing the DFT calculations in detail, I present an argument based on dipolar anisotropies to help explain the direction of the ordered Cu magnetic moment suggested by recent neutron scattering experiments by Wang *et al.* [153]. Wang *et al.* have determined the ordered moment in the low-pressure Q2D phase of $CuF_2(H_2O)_2(pyz)$ to be 0.60(3) μ_B along the [0.7 0.0 1.0] direction with an ordering wavevector [0.5 0 0]. Interestingly this moment direction does not correspond to any of the crystal axes. Furthermore, Wang *et al.*'s analysis employed the dipole approximation for the Cu^{2+} form factor which may induce a systematic error on both the direction and magnitude of the magnetic moment due to the anisotropy of the $d_{x^2-y^2}$ orbital [153]. It is therefore worthwhile to understand the energetics of different moment directions in $CuF_2(H_2O)_2(pyz)$. Since the Cu^{2+} ions are spin-1/2, a single ion anisotropy term DS_z^2 produces no anisotropy. Furthermore the moments are collinear so a potential Dzyaloshinskii-Moriya interaction $\mathbf{D}_{ij}^{\mathrm{DM}} \cdot (\mathbf{S}_i \times \mathbf{S}_j)$ is likely to be small. As a potential source of anisotropy this leaves primarily the dipolar anisotropy experienced by spins in the dipolar field of their neighbours. However, a small easy-plane exchange anisotropy term on the order of a few percent is also often observed in molecular magnetic systems of this type [156]. Here I concentrate on the dipolar anisotropy, which I

have calculated for the collinear antiferromagnetic structure of $CuF_2(H_2O)_2(pyz)$ with ordering wavevector [0.5 0 0] for localised moments located only on the Cu sites.

The dipolar field $\mathbf{B}(\mathbf{r}_0)$ was evaluated inside a Lorentz sphere of radius $r_\mathrm{L} = 5a$ lattice parameters, excluding the contribution of the arbitrarily chosen moment $\mathbf{m}_0$ at position $\mathbf{r}_0$. The resulting dipolar field and hence calculated anisotropies are expected to be converged within 5%. The dipolar energy of a chosen Cu moment $\mathbf{m}_0$ is then given by

$$E = -\mathbf{m}_0 \cdot \mathbf{B}_\mathrm{dip}. \tag{5.5}$$

This is equivalent to performing the summation

$$E = \sum_{i \neq 0} -\frac{\mu_0}{4\pi r_{i0}^3} \left[3(\mathbf{m}_i \cdot \hat{\mathbf{r}}_{i0})(\mathbf{m}_0 \cdot \hat{\mathbf{r}}_{i0}) - \mathbf{m}_i \cdot \mathbf{m}_0\right], \tag{5.6}$$

where the sum is over all moments $i \neq 0$ within the Lorentz sphere, $\hat{\mathbf{r}}_{i0}$ is the normalised separation vector between moments $\mathbf{m}_i$ and $\mathbf{m}_0$, and μ_0 is the vacuum permeability.

This calculation was performed for a number of directions of the magnetic moments $\mathbf{m}_i$ so as to evenly sample over the surface of a sphere. The resulting energies are plotted in Fig. 5.4 for both the low-pressure and the high-pressure phases for which the experimental lattice parameters at 0 kbar [150] and 18 kbar [155],

respectively, were used. In the chosen coordinate system

$$\begin{aligned} \mathbf{a} &= a\,[\sin(\beta), 0, \cos(\beta)], \\ \mathbf{b} &= b\,[0, 1, 0]\,, \\ \mathbf{c} &= c\,[0, 0, 1], \end{aligned} \tag{5.7}$$

where a, b, c are the unit cell dimensions and β is the angle between the **a** and **c** axes ($\beta = 112.029°$ at 0 kbar and $\beta = 115.095°$ at 18 kbar).

The calculation indicates that at this level of approximation the dipolar easy axis is not directed along any of the crystal axes. Instead it is close to (although not exactly along) the x-axis chosen above, which can be explained as follows. The dominant term in Eq. 5.6 is due to the nearest neighbours which, for any chosen Cu spin, are displaced by [0 0.5 0.5] and whose moments are antiparallel to $\mathbf{m}_0$. This leads to a large dipolar energy cost for moments along the b- or c-direction (greater along the c-axis since $c < b$ in both phases). The next nearest neighbour term is due to the interaction within the a-c plane where the moments are located approximately (though not exactly) on the corners of an equilateral triangle (see Fig. 5.5). This interaction is weaker than the nearest neighbour interaction and favours alignment of the moments along the c-axis and introduces an energy cost for moments along the a-axis. The consequence of this is that moments align approximately between the a- and c-axes which is close to the x-direction. Note that this is not the moment direction obtained from neutron scattering. The analysis of the experimental muon data above, combined with the knowledge about the muon sites and perturbations gained from the DFT calculations presented below, suggests a slightly better agreement with the experimental data for Cu moments along x. It is possible, however, that an additional small

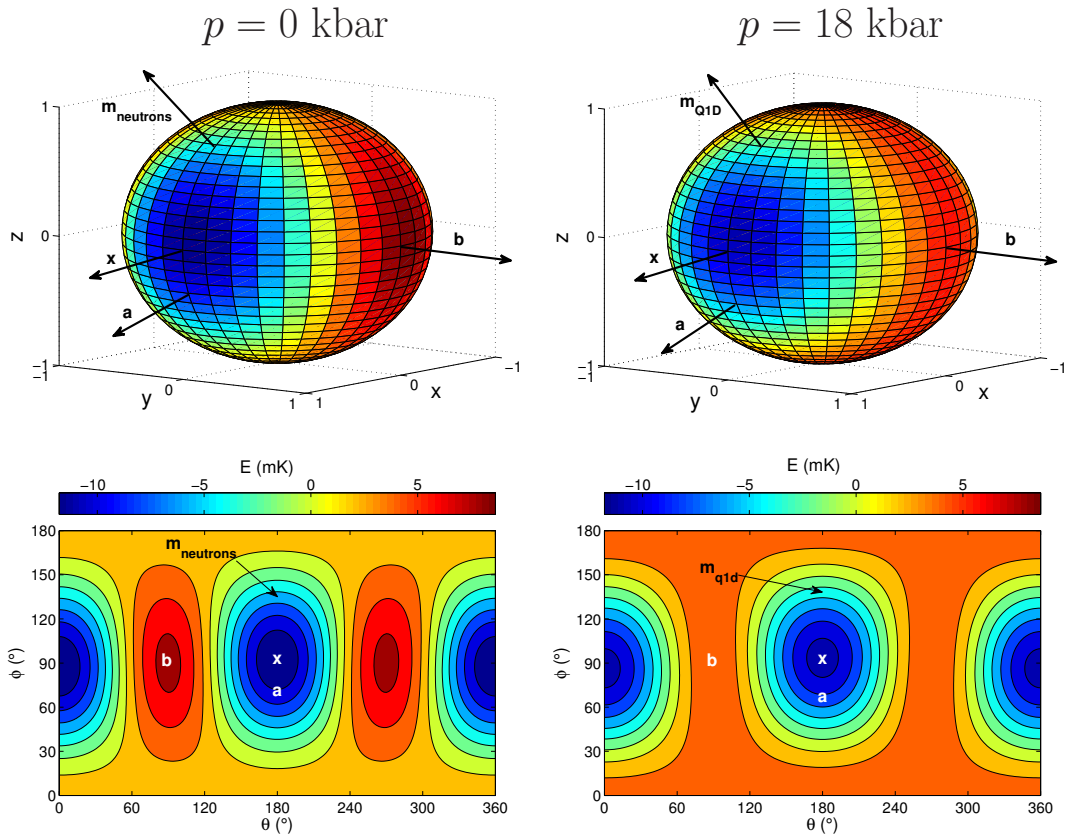

Figure 5.4: Calculated dipolar anisotropy for a Cu moment of 1 μ_B for the collinear antiferromagnetic state in $CuF_2(H_2O)_2(pyz)$. Dark blue regions indicate energetically favourable moment directions. Top: projection onto the surface of a unit sphere indicating the direction of the magnetic moment, bottom: contour plot in the θ-ϕ plane, where θ is the azimuthal angle with the x-axis in the x-y plane and ϕ is the zenith angle with the z(or c)-axis. The dipolar easy axis is close to the x-axis of the coordinate system chosen in Eq. 5.8. $\mathbf{m}_{\mathrm{neutrons}} \parallel [0.7\ 0.0\ 1.0]$ is the moment direction obtained from neutron scattering and $\mathbf{m}_{\mathrm{q1d}} \parallel [0.7\ 0.0\ 1.0]$ is the equivalent direction in the higher pressure phase (shown to correspond to Q1D behaviour in this work). The energy scale is identical for all four plots so the colouring can be compared directly.

anisotropy term favours shifting the moment direction further towards the c-axis and hence towards the [0.7 0.0 1.0] direction obtained from neutron scattering. For example, a small easy-plane exchange anisotropy may be responsible [156].

5.4.1 DFT computational details

Spin-polarised calculations were performed for the experimentally-known magnetic unit cell determined from neutron scattering [153], which contains $2 \times 1 \times 1$ conventional unit cells. Calculations were performed for both charged and neutral supercells. Total energies were converged to at least 2×10^{-12} Ry/atom (Ry is the Rydberg constant). Structural relaxations, total energies, band structures, and vibrational modes were calculated with wavefunction and charge density cutoffs of 80 and 320 Ry, respectively. A muon was placed in several randomly chosen low-symmetry sites and all ions were allowed to relax until the force on each ions had fallen below 10^{-3} Ry/a_0 (a_0 is the Bohr radius) and the energy change between subsequent steps had dropped below 10^{-4} Ry. The unit cell was fixed during all structural relaxations. Contact hyperfine couplings were calculated using the projector-augmented wave (PAW) method [83] as implemented in the GIPAW package [85]. The PAW calculation required norm-conserving datasets with wavefunction and charge density cutoffs of 120 Ry and 480 Ry, respectively. The PAW datasets and cutoffs were also used for the calculation of the Löwdin charges used to estimate magnetic moments. All calculations used a Gaussian broadening of the occupations of 0.02 Ry.

5.4.2 DFT results

First the optimised structures were calculated without the muon. This was done at a number of pressures, where the pressure was set by fixing the unit cell parameters to the experimentally determined values at a particular pressure. The results of this optimisation are summarised in Table 5.1. In the low-pressure phase the calculations correctly predict the Cu–N–Cu axis to be the elongated JT-axis with bond lengths that are almost exactly identical to the experimental values except for the Cu–F–Cu axis which is approximately 5% too long. Only small changes in the bond lengths are observed within the low-pressure phase as pressure is increased. Around 10 kbar, where the unit cell parameters change abruptly, DFT correctly predicts a change in JT-axis. However, the calculations incorrectly predict the Cu–F–Cu axis to be the elongated JT-axis in the high pressure phase, rather than the Cu–O–Cu axis. Note that in the third experimentally known phase, this is indeed the correct JT-axis. These results are independent of which initial (prior to the ionic relaxation) positions were assumed for the ions; for example at 18 kbar starting from the fractional coordinates at 0 kbar implies starting from a Cu–O–Cu JT axis but the relaxed state in either case involves a Cu–F–Cu JT axis instead. This indicates that the equilibrium state is achieved reliably.

Remaining with the unit cell without an implanted muon, the spin density was calculated for (a) the $p = 0$ kbar and (b) the $p = 18$ kbar relaxed structures, and (c) the experimental structure [155] at $p = 18$ kbar. The results are shown in Fig. 5.5. At ambient pressure the magnetic orbital lies in the *bc* plane as expected since the elongated JT-axis is the Cu–N–Cu axis. The Q2D nature of the magnetism in this phase is due to the diagonal orbital overlap in the *bc* plane, as found by previous calculations [151]. At 18 kbar, the calculations predict the

(a) $p = 0$ kbar with calculated ionic positions

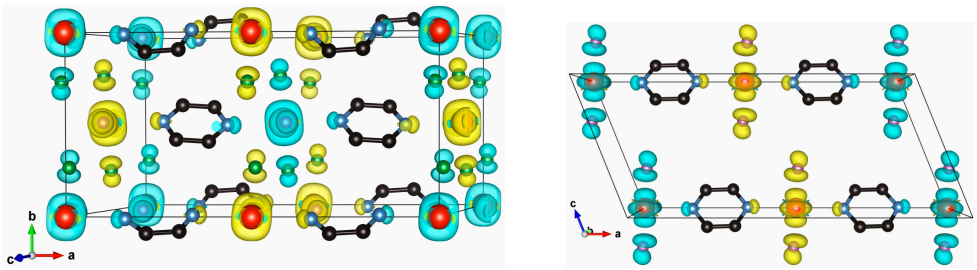

(b) $p = 18$ kbar with calculated ionic positions

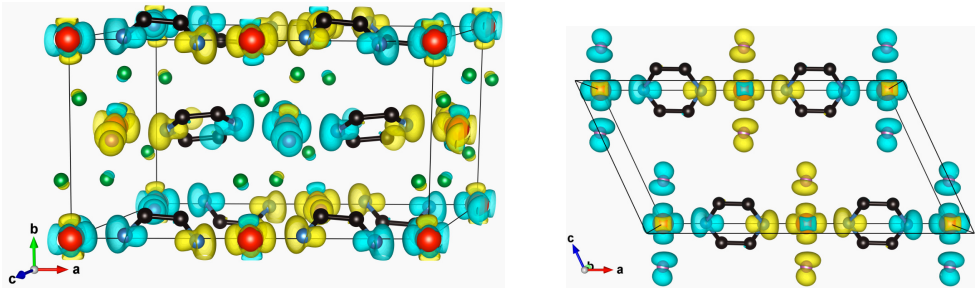

(c) $p = 18$ kbar with experimental ionic positions

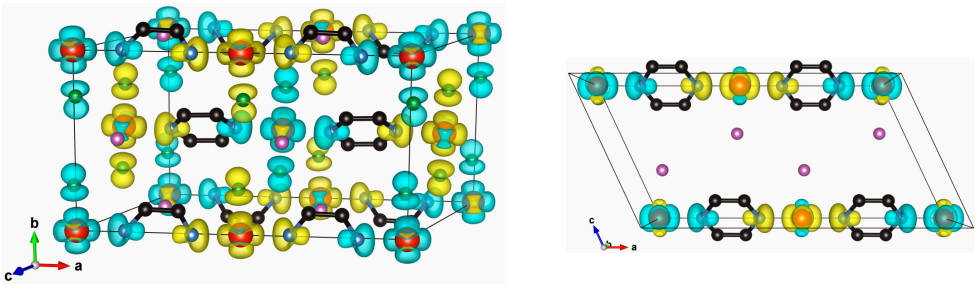

Figure 5.5: Calculated spin density in the magnetic unit cell. Yellow (cyan) isosurfaces represent positive (negative) regions. The isosurface level is $0.02/a_0^3$, where a_0 is the Bohr radius. The colour scheme is the same as in Fig. 5.1 but the atomic radii are modified to show the (red) magnetic Cu^{2+} ions more clearly. (a) For the $p = 0$ kbar calculated structure the spin density shows the largest overlap in the *bc* plane. (b) The $p = 18$ kbar calculated structure where the JT-axis is the Cu–F axis. The magnetic orbital lies in the *ac* plane and the material shows Q1D magnetic properties since the diagonal overlap in the *bc* plane is severely hindered by the lack of overlap along *b* and the increased mismatch of the orbitals preventing direct overlap along *c* (shown on the right). The primary overlap is along the Cu–pyz–Cu chain. Experimentally this corresponds to the third and highest pressure phase. (c) The $p = 18$ kbar experimental structure [155] with Cu–O being the JT-axis. As in (b) the overlap is primarily along the Cu–pyz–Cu chain but here the magnetic orbital lies in the *ab* plane.

	Cu–N (Å)	Cu–O (Å)	Cu–F (Å)
Exp: $p = 0$ kbar, Manson *et al.* [150]	2.423	1.978	1.916
DFT: $p = 0$ kbar unit cell [150]	2.421	1.972	2.033
Exp: $p = 9.3$ kbar, Halder *et al.* [154]	2.372	1.997	1.981
DFT: $p = 9.3$ kbar unit cell [154]	2.399	1.966	2.048
Exp: $p = 12.39$ kbar, Halder *et al.* [154]	2.019	2.211	1.955
DFT: $p = 10.16$ kbar unit cell [154]	2.057	2.042	2.243
Exp: $p = 17.92$ kbar, Halder *et al.* [154]	1.983	2.282	1.999
DFT: $p = 17.92$ kbar unit cell [154]	2.047	2.036	2.246
Exp: $p = 18$ kbar, Prescimone *et al.* [155]	2.039	2.308	1.898
DFT: $p = 18$ kbar unit cell[a] [155]	2.048	2.042	2.237

Table 5.1: Experimental (exp) and calculated (DFT) Cu coordination bond lengths. The DFT calculations show the JT-axis switch at the same pressure (set by the experimental unit cell parameters) as observed experimentally. However, while the correct JT-axis is predicted in the low-pressure phase, the DFT calculations incorrectly predict the Cu–F–Cu axis as the elongated JT-axis in the high-pressure phase. Unless mentioned otherwise, the calculations start from the experimental fractional ionic positions at 0 kbar [150]. [a]Starting from the experimental ionic coordinates at $p = 18$ kbar [155].

JT-axis to have switched to the Cu–F–Cu axis and the magnetic orbitals are found to lie in the *ac* plane. Due to the lack of overlap along the *b*-direction and the further reduction of direct overlap along the *c*-direction, the magnetic properties of this phase are due to the Q1D overlap along Cu–pyz–Cu chains. Experimentally this scenario corresponds to the third (and highest pressure) phase. When the experimental structure at 18 kbar [155] is used instead, the JT-axis is the Cu–O–Cu axis and the magnetic orbitals are located in the *ab* plane with very little overlap along *c*. The primary exchange pathway remains the Cu–pyz–Cu chain and the material can be expected to show Q1D magnetic properties. These calculations provide an insight into the nature of the magnetism in all three phases complementing in particular the structural data (i.e. the information on the JT axes) obtained in the two higher-pressure phases where spin densities had not been calculated previously, as well as the EPR data [155] where the critical

pressures disagree with the values obtained previously [154] and in this work (by μ^+SR and magnetisation measurements).

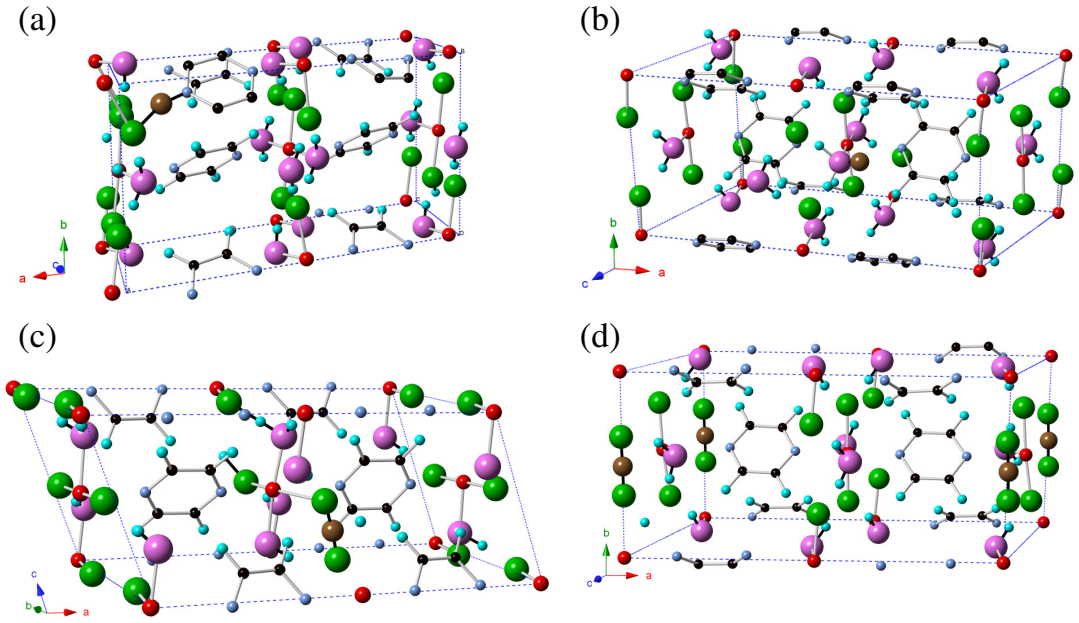

Figure 5.6: Calculated muon sites for $q = +1$ supercell. The colour scheme is the same as in Fig. 5.1 and the muon is a large brown sphere. Nearest neighbour crystallographic distortions are given in brackets. (a) The F–μ^+–N site (N: 0.7 Å, Cu: 0.5 Å, F: 0.4 Å). (b) A hydronium site where the muon forms part of the ion $H_2\mu O^+$ (H: 0.4 Å, O: 0.2 Å, Cu: 0.2 Å). (c) An F–μ–F ion with bond parallel to the c-direction (F: 0.7 Å, O: 0.4 Å, Cu: 0.4 Å). (d) An F–μ–F ion with bond axis along the b-direction (H: 0.8 Å, F: 0.6 Å, O: 0.6 Å). Apart from (d) all of these sites were also found for a neutral cell.

I now turn to the muon sites determined by relaxing the unit cell with a muon placed in a number of randomly chosen low-symmetry sites. All relaxations were performed in a supercell with the fixed experimental unit cell parameters [150]. Unlike for the case of the ionic fluorides considered in Chapter 4, the charge state of the muon was not determined by the charge of the supercell. Instead the more covalent nature of the molecular orbitals leads to only comparatively small differences between the neutral and charged cells, with the final relaxed muon

sites being nearly identical in most cases, although there are differences in the calculated perturbation of the spin density (see below). Only the muon sites in the ambient pressure phase will be discussed in detail. The erroneous prediction of the Cu–F axis as the JT-axis in the high-pressure phase implies incorrect positions for both the O and the F ions, both of which are found to be important muon stopping sites in both phases. While the structural errors are probably only on the order of 0.2 Å, they are sufficient to cause enough uncertainty to preclude a detailed analysis of the magnetic structure and moment in the high-pressure phase on the basis of the experimental μ^+SR data. Nonetheless the calculated dipolar couplings[3] are consistent with the magnetic moment estimated in Section 5.6. The types of sites in the high-pressure phase are very similar to those found in the low-pressure phase and can be described as muons forming $H_2\mu O$ molecules, F–μ–F centres, and an F–μ–O state where the muon bonds to one fluoride and one oxygen ion.

I now discuss the muon sites in the low-pressure phase. The calculations reveal four types of interstitial (as opposed to substitutional) low-energy sites, all of which are predicted to be diamagnetic by GIPAW calculations. The different types of sites are shown in Figure 5.6 and can be described as follows: (a) The site with the lowest classical total energy can be described as F–μ–N, where the muon bonds to a fluoride and a nitrogen (from the pyrazine ring) with bond lengths of 1.6 Å and 1.1 Å, respectively. This should give rise to an F–μ signal as has indeed been observed experimentally, albeit with an estimated F–μ bond length of 1.1 Å [150]. (b) The muon also forms a hydronium-type site (hereafter *hydromuonium*) where the muon forms part of the $H_2\mu O^+$ ion, where in analogy to the hydronium ion H_3O^+, the positive charge density is likely to be concentrated

[3]The calculation is described in detail for low-pressure phase below.

on the oxygen ion. The hydromuonium sites are approximately 0.4 eV higher in energy than the F–μ–N site. A number of these sites exist within the unit cell, which are not all magnetically equivalent for the antiferromagnetic structure that $CuF_2(H_2O)_2(pyz)$ assumes. (c-d) The muon is also predicted to form linear F–μ–F complexes with F–μ bond lengths of 1.2 Å, similar to those found in the ionic fluorides discussed in Chapter 4. The crystallographic distortions of the nearest neighbour atoms (indicated in the caption of Fig. 5.6) are similar to those encountered in the ionic fluorides demonstrating that though the muon charge may be shielded more effectively by the covalent nature of the material, this effect is compensated by the relative 'softness' of the covalent bonds.

For the neutral supercell only F–μ–F states along the crystallographic c-direction are predicted[4], while for the charged supercell F–μ–F states are predicted to occur both along the c and b axes (see Fig. 5.6). For the charged cell the F–μ–F states in (c) and (d) lie 0.8 eV and 1.0 eV, respectively, above the F–μ–N site. The ordering of the states is unaffected by the charge state of the unit cell and the level splittings are similar. Note that none of these energies take account of the muons' zero-point motion, which was shown to be substantial in Chapter 4. The size of these systems precludes an estimate of these energies using density-functional perturbation theory and methods based on finding the muon wavefunction in the static ionic potential are unlikely to provide accurate results due to the strong bonding of the muon in all of those sites. The relative energies of those sites, summarised in Table 5.2, should therefore only be taken as an approximate indication. It is conceivable that the kinematics of the muon stopping process will lead to the population of all of those sites, since in all of

[4]Instead of the F–μ–F state shown in Fig. 5.6(d), a site where the muon bonds to a C atom on the pyrazine ring is predicted. This C site lies 1 eV above the neutral cell ground state, which is also the F–μ–N site.

those sites the muon is localised by strong bonds.

The experimental observation of an F–μ signal with estimated F–μ bond length of 1.1 Å [150] does not contradict the DFT results above since a combination of an F–μ–F signal (bond length 1.2 Å) and an F–μ signal (bond length 1.6 Å) will yield a very similar depolarisation. Also note that not in every molecular system containing fluorine is an F–μ–F state found experimentally. In the purely organic molecular radical magnet F4BImNN, fluorine atoms are covalently bonded in a conjugated ring and are hence less attractive stopping sites for muons than, for example, fluoride ions in ionic insulators; a fact that was successfully reproduced in recent DFT calculations of muon stopping sites in F4BImNN [115].

Site	E (eV)	ν_μ/μ_B (MHz) $\mathbf{m}_\mathrm{Cu} \parallel [0.7\ 0.0\ 1.0]$	Ratio	ν_μ/μ_B (MHz) $\mathbf{m}_\mathrm{Cu} \parallel \hat{\mathbf{x}}$	Ratio
F–μ–N	0.0	10.4	0.65	15.9	1.0
Hydromuonium	0.34	5.9	0.36	3.4	0.21
Hydromuonium	0.42	12.6	0.78	9.7	0.61
Hydromuonium	0.44	16.1	1.0	13.4	0.84
F–μ–F	0.8	6.0	0.37	8.6	0.54
F–μ–F	1.0	10.4	0.64	2.2	0.14
HμO	–	3.8	0.17	4.1	0.2
μ–C	–	8.6	0.39	9.8	0.48
μ–C	–	21.8	1.0	20.5	1.0
μ–C	–	5.8	0.26	7.3	0.36
μ–C	–	6.9	0.32	10.1	0.49

Table 5.2: Summary of calculated magnetically-inequivalent interstitial muon sites (top) in the charged supercell and possible substitutional sites (bottom) using the relaxed hydrogen positions for a neutral supercell without the muon. This table compares the relative (classical) energy of the muon as well as the estimated dipolar couplings for a Cu moment $\mathbf{m}_\mathrm{Cu}$ of 1 μ_B for two different moment directions: the experimental moment direction measured with neutron scattering and for Cu moments along the x-axis which would minimise the dipolar energy.

To compare with the experimental μ^+SR data, the dipolar couplings given by Eq. 2.10 were calculated for muons in all of the four types of sites found above,

assuming localised moments located on the Cu^{2+} sites. Perturbations in crystal structure and magnetic moment were taken into account within one supercell around the muon (perturbing four Cu^{2+} ions). The Cu^{2+} spin-only moment, estimated for the relaxed structure without the muon, is 0.72 μ_B from a Löwdin population analysis, while a simple integration of the absolute spin density in the supercell yields a spin-only moment of 1.05 μ_B. Part of the difference between these two values may be due to a small amount of real delocalisation of the spin density away from the Cu^{2+} ion. Given the challenges in calculating magnetic moments accurately using DFT [157; 158] this is consistent with the full moment of 1 μ_B expected for a spin-1/2 system. The perturbation of the spin-only moment in presence of the muon was estimated from the perturbation of the Löwdin charges. This perturbation is up to -20% for the charged supercell and up to -58% for the neutral supercell. The perturbation of the total moment was assumed to scale identically. Table 5.2 shows the resulting calculated dipolar couplings for the charged supercell. For the neutral supercell, though the sites are nearly identical, the perturbation of the Cu^{2+} moments close to the implanted muon is considerably higher than for the charged supercell, particularly for those muon sites located close to the Cu^{2+} ions, which experience the largest dipolar couplings. The largest coupling is approximately 7.7 MHz for a Cu moment of 1 μ_B (for some of the hydromuonium sites). This would yield an unrealistically large ordered Cu^{2+} moment of nearly 1 μ_B (see below). Therefore, only the results for the charged supercell will be discussed in detail. Future work will involve hybrid functionals such as BLYP [75; 76], which are frequently employed in the study of molecular systems, to investigate the perturbation of the moments in more detail.

The ratio of the calculated dipolar couplings for the interstitial sites is in ap-

proximate agreement with the frequency ratio of 1:0.65:0.55 assumed in fitting the experimental μ^+SR data in the low-pressure phase. To assess whether the calculated couplings are indeed compatible with the experimental data, the experimental data measured at 270 mK and 4.8(1) kbar were refitted to the following equation

$$\begin{aligned} A(t) =& A_1 e^{-\lambda_1 t}\cos(2\pi\nu_1 t) \\ &+ A_2 e^{-\lambda_2 t}\cos(2\pi\nu_2 t) \\ &+ A_3 e^{-\lambda_3 t}\cos(2\pi\nu_3 t) \\ &+ A_4 e^{-\lambda_5 t}\cos(2\pi\nu_4 t) + A_5 e^{-\lambda_6 t} + A_{\mathrm{b}}(t), \end{aligned} \tag{5.8}$$

where the ratio $\nu_1 : \nu_2 : \nu_3 : \nu_4$ was fixed to $1 : 0.78 : 0.66 : 0.37$ for $\mathbf{m}_{\mathrm{Cu}} \parallel [0.7\ 0.0\ 1.0]$ and $1 : 0.84 : 0.57 : 0.18$ for $\mathbf{m}_{\mathrm{Cu}} \parallel \hat{\mathbf{x}}$. In both cases the ratio $A_1 : A_2 : A_3 : A_4$ was fixed to $4 : 2 : 2 : 1$ and all other parameters took similar values to the fit described in Eq. 5.1 above. Phases have been omitted intentionally. Note that since the lattice parameters and ionic coordinates only exhibit small changes with pressure within each phase a comparison of the experimental data measured at 4.8(1) kbar with the dipolar couplings calculated at ambient pressure is reasonable. This is confirmed by the weak dependence of $\nu(T = 0)$ on pressure, best illustrated in Fig. 5.3(f). The resulting fits are shown in Fig. 5.7(a). Both fits are of good quality although they yield slightly higher values of reduced χ^2 than the original best fit (1.26 for fits based on Eq. 5.8 compared with 1.22 for the fit based on Eq. 5.1). Fig. 5.7(b) shows the maximum entropy spectrum[5] of the same experimental data set together with the calculated muon precession frequencies scaled by the maximum frequency ν_1 fitted in Eq. 5.8.

[5]Obtained using the WiMDA program [159].

The calculated lines agree reasonably well with the maximum entropy spectrum confirming that the calculated μ^+SR spectrum provides a good description of the experimental data. Note that here the agreement is better for Cu moments along x. This might indicate an error in the moment direction suggested by neutron scattering. The analysis of the neutron scattering data employed the dipole approximation for the Cu^{2+} form factor which may induce a systematic error on both the direction and magnitude of the magnetic moment due to the anisotropy of the $d_{x^2-y^2}$ orbital [153].

Assuming the moment direction $\mathbf{m}_{\mathrm{Cu}} \parallel [0.7\ 0.0\ 1.0]$ suggested by neutron scattering [153], the value of the fitted frequency $\nu = 8.55$ in Eq. 5.8, together with the calculated dipolar couplings in Table 5.2, allows the zero-field Cu^{2+} moment to be estimated to be $m_{\mathrm{Cu}} \approx 0.53\ \mu_{\mathrm{B}}$. This value is identical if the Cu^{2+} moments are assumed to lie along the x-axis. This is in reasonable agreement with the value of 0.60(3) μ_{B} obtained by neutron scattering [153]. The heavily-reduced size of the ordered moment is due to a renormalisation by quantum fluctuations in Q2D magnetic systems, which reduce the size of the zero-temperature ordered moment to 0.62 μ_{B} for the ideal two-dimensional quantum Heisenberg antiferromagnet [25]. A similar reduction has been found in other low-dimensional magnetic systems [160–162]. Note that DFT can been viewed as taking a 'snapshot' of the system and would not be able to predict any such reduction due to quantum fluctuations. This result is therefore consistent with the DFT prediction of the full moment of 1 μ_{B}.

While the moment direction may not be firmly constrained in this case it is conceivable that μ^+SR experiments with a smaller background (i.e. without a pressure cell) and with higher statistics will be able to distinguish between different trial magnetic structures. Therefore this study is not only a rare ex-

ample where the determination of the magnetic moment has been possible using μ^+SR but also sets an important precedent, particularly for μ^+SR experiments on frustrated systems where moment sizes are often too small to be measured with neutron scattering (see for example Ref. 33).

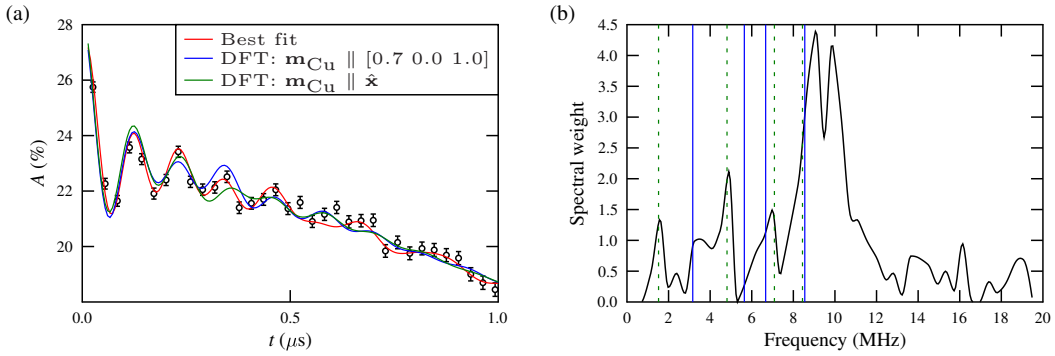

Figure 5.7: (a) Comparison of best fit to experimental μ^+SR data measured at 270 mK and 4.8(1) kbar described by Eq. 5.1 and fits to Eq. 5.8 using the *ab initio* estimates of the ratio of the dipolar couplings for interstitial muons for Cu moments along [0.7 0.0 1.0] and along the x-axis. (b) Maximum entropy spectrum for the same experimental data set with the calculated frequencies shown as vertical lines for the two Cu moment directions. The calculated frequencies are scaled by the time-domain fit of ν_1 in Eq. 5.8.

In addition to the interstitial sites discussed above, perhaps the most obvious candidate sites for implanted muons are the proton sites in the H_2O groups or the pyrazine ring. If the substituted hydrogen atom has sufficient energy to be displaced from the trapping unit cell, there may be no damage to that cell at all. The energy of these sites may not be directly compared to the energy of the interstitial sites since the number of atoms involved is not identical (and neither is the charge in the case of the charged cell). The likelihood of a muon replacing any one of those hydrogen atoms is therefore not easy to estimate. Table 5.2 shows the dipolar couplings for a muon substituting for one of the protons in $CuF_2(H_2O)_2$(pyz). Note that per formula unit there are four hydrogen

atoms in H_2O molecules (all are found to have an identical dipolar coupling) and four hydrogens in the pyrazine ring (which are found to have different dipolar couplings). The couplings are similar for the two Cu moment directions and for a moment size of 0.53 μ_B they are compatible with the experimentally observed μ^+SR spectrum. It is therefore possible that some of these sites are realised experimentally.

Finally I briefly discuss the issue of non-zero phase factors, which are almost ubiquitous in the μ^+SR spectra of molecular magnets. A muon localising at time $t = 0$ in a single site with magnetic field B_μ should experience a rotation of its spin $\propto \cos(\gamma_\mu B t + \phi)$ with $\phi = 0$ (see Chapter 2). Yet many μ^+SR spectra, including those measured in the low-pressure phase above, are best described with non-zero values of ϕ, a fact that has never been explained satisfactorily. One explanation would be that muons form the state where their spins undergo precession with some constant delay t_0. However the phases found here and in other μ^+SR experiments [163] are best kept constant and do not correlate with the precession frequency ν, which precludes at least this simple model of delayed state formation. While no definite conclusions about the appearance of phase factors in μ^+SR data on molecular magnets can be made based on this work alone, it does highlight two important points. First, in complex molecular systems such as molecular magnets there will frequently be a large number of muon stopping sites. Second, the fits to Eq. 5.8 shown in Fig. 5.7 are of nearly the same quality as the fit to Eq. 5.1 which contains three further parameters (the phases ϕ_1 - ϕ_3). Both of these points can be expected to be valid in most molecular magnets. The improvement in the quality of the fit by adding phase factors is then due to the approximation of the true broad distribution of magnetic couplings (with some finite cutoff ν_{max}) with a smaller number of precession frequencies.

Note that the maximum entropy spectrum shown in Fig 5.7 is not unlike the fre-

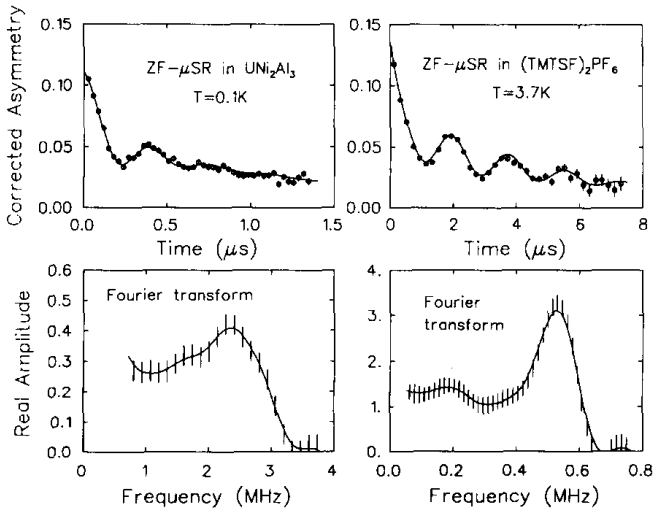

Figure 5.8: Zero-field μ^+SR time-domain data and Fourier transform for below the ordering temperature in UNi_2Al_3 (left) and in $(TMTSF)_2PF_6$ from Ref. 164. Copyright Elsevier Science Publishers.

quency spectrum (reproduced in Fig. 5.8) measured in the heavy fermion system UNi_2Al_3 and the organic compounds $(TMTSF)_2X$ ($X = PF_6, NO_3, ClO_4$). In UNi_2Al_3 and $(TMTSF)_2X$ the shape of the frequency spectrum is attributed to an incommensurate spin-density wave (SDW) state [164; 165], which gives rise to a continuous distribution of precession frequencies up to some finite cutoff $\nu_{\max}$ leading to a time-domain spectrum that is described by a zeroth-order Bessel function $J_0(2\pi\nu_{\max}t)$ [166; 167]. While the cause for this frequency distribution in $CuF_2(H_2O)_2(pyz)$ is the large number of muon sites rather than an incommensurate magnetic structure the effect on the time-domain spectrum is similar. Since a zeroth-order Bessel function $J_0(2\pi\nu_{\max}t)$ approximates a phase shifted sinusoidal oscillation $\cos(2\pi\nu_{\max}t + \pi/4)$ at early times, this would explain the apparent phase factors in the time-domain spectra. At large times where a deviation from a simple phase shifted cosine would become apparent, the damping of the oscillations (width of the spectral lines) typically experienced precludes a

more detailed analysis. Some deviations from the expected phase shift of $\pi/4$ can be expected since the frequency distribution will differ from that in an ideal incommensurate SDW system.

5.5 Magnetisation results

Single crystal magnetisation measurements in fields up to 35 T were performed at NHMFL, USA. Measurements were performed at 1.4 K, with the applied magnetic field parallel to the Cu–pyz–Cu chain direction. As for the μ^+SR measurements, a piston cylinder cell was used. The pressure was measured *in-situ* using the fluorescence of ruby, which showed good hydrostatic conditions.[6] Two measurements were performed in the low pressure regime ($P < P_c$), another at the critical pressure P_c, and a further three in the high pressure region ($P > P_c$).

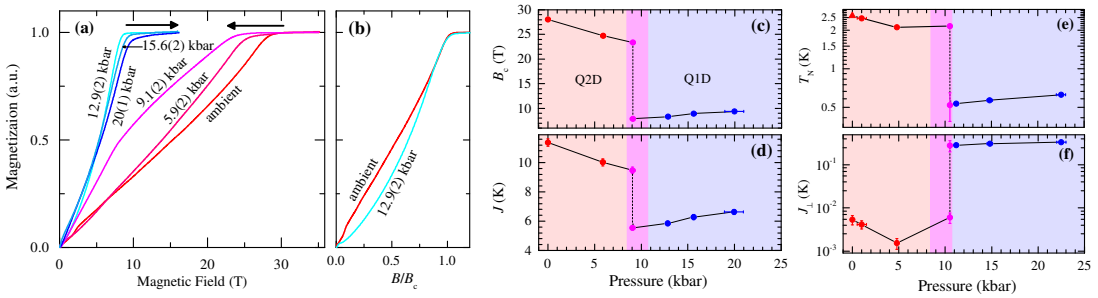

Figure 5.9: (a) magnetisation of $CuF_2(H_2O)_2(pyz)$ single crystals with $B \parallel a$-axis, at 1.4 K (2 K at 15.6 kbar). The arrows represent the change in the saturation field with increasing pressure. (b) M vs B/B_c at ambient pressure and 12.9 kbar, showing the change in curvature. Also shown is (c) the saturation field B_c, (d) the deduced primary exchange coupling energy J, (e) the ordering temperature T_N deduced from the μ^+SR data (see Fig. 5.3), and (f) the secondary exchange $J_\perp$. To extract J, we have used values of g obtained from EPR measurements [155]. T_N at ambient pressure (triangle symbol) is from Ref. [150].

The magnetisation, measured across a range of pressures up to 20 kbar, is given

[6] Further details are given in Ref. [144] and the DPhil thesis of Saman Ghannadzadeh.

in Fig. 5.9(a). At ambient pressure the magnetisation rises monotonically with a concave curvature typical of Q2D antiferromagnetic systems [149], saturating at 28.1 T in agreement with previous measurements [150]. As pressure is applied, we observe a steady reduction in the critical field B_c, down to 23.4 T at 9.1 kbar [see Fig. 5.9(c)]. Further application of pressure leads to a sudden drop in B_c to 8.3 T, after which any additional pressure serves to gradually increase the saturation field, in contrast to the behaviour seen at lower pressures.

The magnetism in $CuF_2(H_2O)_2(pyz)$ can be described by the Heisenberg model

$$\mathcal{H} = J \sum_{\langle i,j \rangle_{\parallel}} \mathbf{S}_i.\mathbf{S}_j + J_{\perp} \sum_{\langle i,j \rangle_{\perp}} \mathbf{S}_i.\mathbf{S}_j - g\mu_B B \sum_i S_i^z, \tag{5.9}$$

where in a Q2D (Q1D) phase, J and $J_{\perp}$ are the magnetic exchange strengths within and normal to the planes (chains), respectively. The first two summations are over the unique ligands through which the exchange coupling takes place, and the last term is the Zeeman splitting term. In a strongly anisotropic system ($J_{\perp} \ll J$), we can therefore express the saturation field as

$$B_c \approx nJ/g\mu_B, \tag{5.10}$$

where n is the number of nearest neighbor exchange ligands of interaction strength J ($n = 4$ for Q2D, 2 for Q1D), and g is the g-factor [168]. The sudden change in B_c can thus be understood as a combination of the change in n from 4 to 2, that is a Q2D to Q1D transition and a simultaneous change in J.

Furthermore, for a Heisenberg spin–1/2 antiferromagnet (AFM) the shape of the magnetisation up to saturation reflects the magnetic dimensionality, and Quantum Monte-Carlo simulations have shown that the magnetisation becomes strongly concave as the dimensionality is reduced [168]. Note that the measured

magnetisation becomes noticeably more concave above 9.1 kbar [Fig. 5.9(b)], indicating a reduction in the magnetic dimensionality from Q2D to Q1D.

The extracted values of J are given in Fig. 5.9(d). We find $J \approx 11.4\,\mathrm{K}$ at ambient pressure, consistent with previous pulsed-field measurements [150]. Under application of moderate pressures, J begins to decrease gradually at a rate of $0.21 \pm 0.01\,\mathrm{K/kbar}$, eventually reaching 9.5 K at 9.1 kbar. A further increase in pressure leads to a substantial reduction in J, down to 5.5 K, caused by the switching of the main exchange pathways to bonds with weaker effective nearest-neighbor interactions as the system undergoes a change in magnetic dimensionality. Within the high pressure region, any further application of pressure results in a steady increase in J at the rate of $0.1 \pm 0.01\,\mathrm{K/kbar}$.

Finally note that for the 9.1 kbar data, the magnetisation gradient changes at a field of 7.9 T, close to the critical field of the higher pressure phase. The curvature of the magnetisation below this field is similar to that of the higher pressure regime, while the curvature above it is closer to that seen at low pressures [see Fig. 5.9(a)]. This is indicative of the coexistence of Q1D and Q2D phases at 9.1 kbar.

5.6 Further discussion

The combination of a substantial change in the μ^+SR frequencies and ordering temperature T_N as well as a sudden reduction in the critical field B_c provide unambiguous evidence and direct confirmation of the proposed phase transition from Q2D to Q1D magnetism at a critical pressure of around 10 kbar, in agreement with the JT-axis switch observed in powder xray measurements [154]. No discontinuous changes were observed in powder μ^+SR or single-crystal magneti-

sation measurements around 18 kbar, the critical pressure region suggested by single-crystal xray and EPR experiments by Prescimone *et al.* [155].

Given the values of J and T_{N}, the secondary exchange constant $J_{\perp}$ for the Q2D and Q1D phases can be estimated using the empirical relations obtained from Monte Carlo simulations

$$|J_{\perp}| = |J| \exp\left(2.43 - 0.88\lambda\right) \qquad \text{(Q2D)}, \tag{5.11}$$

$$|J_{\perp}| = 1.073\, T_{\mathrm{N}} \left(\ln\lambda + 0.5 \ln\ln\lambda\right)^{-1/2} \qquad \text{(Q1D)}, \tag{5.12}$$

where $\lambda = 2.6\, J/T_{\mathrm{N}}$ [169]. The calculated values of $J_{\perp}$ are shown in Fig. 5.9(f). Within the low-pressure Q2D phase we find $J_{\perp}$ to be on the order of 1 mK. In the Q1D regime, $J_{\perp}$ is mediated by the portion of the $d_{x^2-y^2}$ orbitals that still lie within the *bc*-plane [see Fig. 5.5 (c)], and this leads to a jump in $J_{\perp}$ by two orders of magnitude to approximately 0.3 K as we move over to the Q1D phase.

Note that the dipolar anisotropies shown in Fig. 5.4 are on the scale of 5 mK even for an ordered moment of only 0.5 μ_{B} and are therefore larger than the estimated interplane exchange in the Q2D phase. No theoretical model exists to estimate the effect of this dipolar anisotropy on the propensity of the system to undergo ordering and for this reason dipolar anisotropies have been neglected in virtually every study of molecular magnets of this kind. While the dipolar anisotropy may primarily affect the direction of the ordered moment, dipolar interactions have been shown to be capable of driving molecular magnetic systems to order at temperatures as high as 58 K [170]. Future theoretical work will be required to understand the importance of dipolar anisotropies for the condensation of magnetic order in more detail.

Furthermore, fluctuations significantly reduce the size of the ordered moment

in low-dimensional AFMs. The zero-field moment in a spin–1/2 Q1D AFM can be estimated in a mean-field approximation from $m_0 = 2.034\sqrt{J_\perp/J}\,\mu_B$ [171]. The value of $J_\perp/J$ remains approximately constant within the Q1D phase, yielding a value of $m_0 = 0.46 \pm 0.01\,\mu_B$. This compares with a moment estimate for the Q2D phase of 0.60(3) μ_B measured by magnetic neutron scattering [153] and moments of $0.5\,\mu_B$ and $0.072\,\mu_B$ in the Q1D AFMs $KCuF_3$ and Sr_2CuO_3 [171].

The trends in J [Fig. 5.9(d)] can be explained in terms of the effect of pressure on the crystal structure and the magnetic exchange ligands. The decrease seen in J within the Q2D phase is due to the increase in the β-angle between the a and c axes [154], which leads to a misalignment of Cu–pyz–Cu chains and causes them to begin to slide past each other [151]. This serves to severely disrupt the H$\cdots$F bonded network, decreasing the efficiency of magnetic coupling along the Cu–OH$\cdots$F–Cu exchange pathways and thus reduces J. The steady increase in J with applied pressure within the Q1D regime may result from the relative resilience of the Cu–N bonds and the pyrazine rings (as opposed to the 'soft' H$\cdots$F bonded layers) with the result that no major distortions are seen within the Cu–pyz–Cu chain in the Q1D regime [151; 154]. This resiliency, together with the decrease in the chain length with applied pressure [154], enhances the magnetic d-orbital density overlap along the chain and results in the increase in J.

Finally a comment on the coexistence of Q1D and Q2D phases observed at 9.1(2) kbar in the magnetisation and at 10.5(2) kbar in the μ^+SR. While it is not possible to completely rule out that this is due to non-hydrostaticity in the measurements[7] or some degree of non-reversibility of the Q2D to Q1D transition,[8]

[7]Non-hydrostaticity is estimated to be ±0.2 kbar at 10.5(2) kbar for the μ^+SR and less than ±0.7 kbar for the 9.1 kbar magnetisation measurement.

[8]For the μ^+SR (magnetisation) measurement the pressure cell was pressurised to approx-

the observations in both powder μ^+SR and single crystal magnetisation measurements, as well as in the separate EPR study [155], seem to point towards the presence of an intrinsic phase separation in the critical pressure region, reminiscent of the phase separation frequently observed close to some pressure-induced quantum phase transitions [172]. This is also consistent with the indication of a phase separation in the original powder xray data by Halder *et al.* [154].

5.7 Conclusions and outlook

It was demonstrated that pressure can be used to operate a Jahn-Teller driven magnetic dimensionality switch in $CuF_2(H_2O)_2(pyz)$, due to a change in the primary magnetic exchange pathways. This provides an example of how pressure can be used to tune magnetic interactions and dimensionality in a transition-metal coordination polymer. The experimental results were complemented with calculations of the dipolar anisotropy, which provide a possible explanation for the direction of the ordered moment. Density-functional theory calculations of the spin density and muon sites have allowed an estimate of the ordered moment in the Q2D phase, which is heavily renormalised due to quantum fluctuations.

Having explored a pressure-induced Q2D to Q1D transition, future work will involve the zero-dimensional coordination polymer piperazinium hexachlorodicuprate (PHCC) and related systems. As for $[Cu(pyz)(gly)](ClO_4)$ discussed in Section 6.3, the low-energy physics of PHCC is best described by a model of weakly-interacting antiferromagnetic dimers giving rise to an $S = 0$ quantum disordered ground state [173; 174] separated by a gap from the degenerate triplet excited levels. The spin gap may be closed through a quantum critical point which

imately 12.8 kbar (11.4 kbar), well within the Q1D phase, to achieve the target pressure of 10.5 kbar (9.1 kbar) at cryogenic temperatures.

may be induced (i) through the application of a magnetic field, which causes one of the triplet modes to soften[9], and (ii) there is evidence from inelastic neutron scattering [174] that it may be possible to close the gap through the application of hydrostatic pressure, which softens all three excited levels. Beam time on GPD has been awarded to study the so-far quite unexplored scenario (ii) which should lead to the observation of 3D long-range order above an applied pressure of around 15 kbar.

[9] As discussed for [Cu(pyz)(gly)](ClO_4) in Sec. 6.3.

Chapter 6

Quantum magnetism in applied fields

This chapter contains two parts. The first describes how subtle differences in chemical composition can lead to starkly different structural and magnetic properties in transition metal coordination polymers. Two distinct molecule-based magnets were synthesised from the same starting compounds. These show different structural motifs which promote contrasting exchange pathways and consequently lead to markedly different magnetic ground states: $[Cu(pyz)(H_2O)(gly)_2](ClO_4)_2$ *may be considered a quantum Heisenberg antiferromagnetic chain that orders magnetically below 50 mK, while the related* $[Cu(pyz)(gly)](ClO_4)$ *is formed from strongly antiferromagnetically interacting* Cu^{2+} *dimers and remains disordered down to at least 30 mK in zero field, but displays a field-temperature phase diagram consistent with the Bose-Einstein condensation of triplons. The second part of the chapter describes* μ^+SR *measurements on the strong-leg spin ladder DIMPY and on the molecular nanomagnets* Cr_8Cd *and* Cr_8Mn *which highlight some of the remaining challenges for longitudinal-field* μ^+SR *experiments.*

6.1 Introduction

The aspiration to tailor bespoke magnetic devices based on molecular magnets depends primarily on the sufficient proficiency in the chemical control of transition metal coordination polymers. This, in turn, relies on a detailed understanding of the relationship between structural and magnetic properties. Here a single synthetic route applied to the same starting compounds is shown to produce two distinct molecular magnets with quite contrasting low-dimensional motifs: the quasi one-dimensional quantum Heisenberg antiferromagnet (Q1DQHAF) $[Cu(pyz)(H_2O)(gly)_2](ClO_4)_2$ and the zero-dimensional dimer compound $[Cu(pyz)(gly)](ClO_4)$ that can be driven to a state of long-range magnetic order in an applied magnetic field *via* a quantum critical point (QCP), yielding a phase diagram reminiscent of the Bose Einstein condensation (BEC) of triplons.

The work presented on the gly-based magnets discussed in the first part of this chapter describes a collaborative effort with the following author contributions: the μ^+SR experiments were performed by myself, Tom Lancaster, Peter Baker, Francis Pratt, and Stephen Blundell. μ^+SR data analysis was performed by myself. The project was led by Tom Lancaster and Stephen Blundell, samples were synthesised and their structures determined by Jamie Manson, heat capacity and susceptibility measurements as well as magnetisation measurements on $[Cu(pyz)(H_2O)(gly)_2](ClO_4)_2$ were performed by L. Huang and Joachim Wosnitza, high-field magnetization on $[Cu(pyz)(gly)](ClO_4)$ was performed by Saman Ghannadzadeh, Francesca Foronda, and Paul Goddard. A preprint of the article is now available [175].

The synthesis of the materials involves mixing aqueous solutions of

$Cu(ClO_4)_2 \cdot 6H_2O$, glycine [NH_2CH_2COOH, (gly)], and pyrazine [$C_4H_4N_2$, (pyz)]. Purple blocks of $[Cu(pyz)(gly)](ClO_4)$ typically form first upon slow evaporation of the solvent, while continued evaporation leads to the formation of blue rods of $[Cu(pyz)(H_2O)(gly)_2](ClO_4)_2$ in higher yield.

6.2 An antiferromagnetic chain: $[Cu(pyz)(H_2O)(gly)_2](ClO_4)_2$

$[Cu(pyz)(H_2O)(gly)_2](ClO_4)_2$ crystallises in the space group $C2/c$ and is based on linear chains of $S = 1/2$ Cu^{2+} ions linked with pyrazine ligands as shown in Fig. 6.1. Glycine and H_2O groups coordinate to the Cu ions and act to separate the chains along with non-coordinating ClO_4 counter-ions. The pyrazine ligand is known to be an effective mediator of magnetic exchange in materials of this type and so one would expect the chain-like structure to promote Q1D antiferromagnetic behaviour.

The magnetic properties of $[Cu(pyz)(H_2O)(gly)_2](ClO_4)_2$ were found to be well-described by the Hamiltonian for a Q1DQHAF

$$\mathcal{H} = J \sum_{\langle i,j \rangle_{\parallel}} \mathbf{S}_i \cdot \mathbf{S}_j + J_{\perp} \sum_{\langle i,j \rangle_{\perp}} \mathbf{S}_i \cdot \mathbf{S}_j - g\mu_B B \sum_i S_i^z, \tag{6.1}$$

where J is the exchange coupling within the magnetic chains, $J_{\perp}$ is the exchange coupling between chains and the first and second terms sum over unique nearest neighbour spins $\mathbf{S}_i$ along and perpendicular to the magnetic chain, respectively. Fig. 6.2(a) shows the measured magnetisation and magnetic susceptibility of a polycrystalline sample of $[Cu(pyz)(H_2O)(gly)_2](ClO_4)_2$. The susceptibility is well-described by the form expected [176] for the model in Eq. 6.1 with $J = 9.4(1)$ K

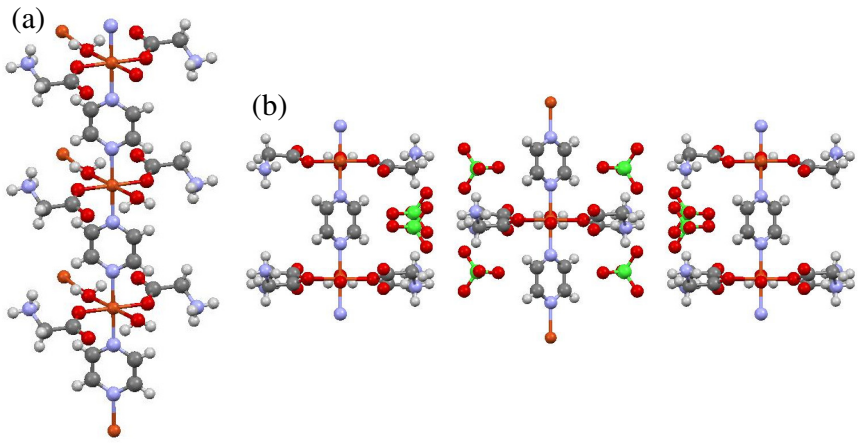

Figure 6.1: Structure of $[Cu(pyz)(H_2O)(gly)_2](ClO_4)_2$. (a) Cu–(pyz)–Cu chains forming the Q1D exchange pathways on which $[Cu(pyz)(H_2O)(gly)_2](ClO_4)_2$ is based. Also shown are the gly and H_2O groups that coordinate the Cu ions. (b) View along the *c*-axis showing the packing of the chains with non-coordinating ClO_4 groups. Colour scheme: Cu (orange), O (red), N (blue) C (grey), H (white), Cl (green).

and $g = 2.10(1)$. Furthermore the magnetisation has a concave curvature typical of a Q1D system [144; 149]. Assuming that $|J_\perp| \ll |J|$ the saturation field $B_c = 13.3(1)$ T allows an estimate of the dominant exchange *via* Eq. 5.10. Using $g = 2.10(1)$ this yields $J = 9.4(1)$ K in good agreement with the value from the susceptibility and typical of Cu–(pyz)–Cu exchange pathways [149].

In addition zero-field (ZF) μ^+SR measurements were performed in order to investigate whether $[Cu(pyz)(H_2O)(gly)_2](ClO_4)_2$ undergoes long-range ordering. A powder sample was mounted on the cold finger of a dilution refrigerator on the LTF instrument, PSI. Example experimental asymmetry spectra are shown in Fig. 6.2(b). The data were described well across the whole temperature range by the following fitting function

$$A(t) = A_1 e^{-\sigma_1^2 t^2} + A_2 e^{-\sigma_2^2 t^2} + A_3 e^{-\lambda t} + A_\parallel, \tag{6.2}$$

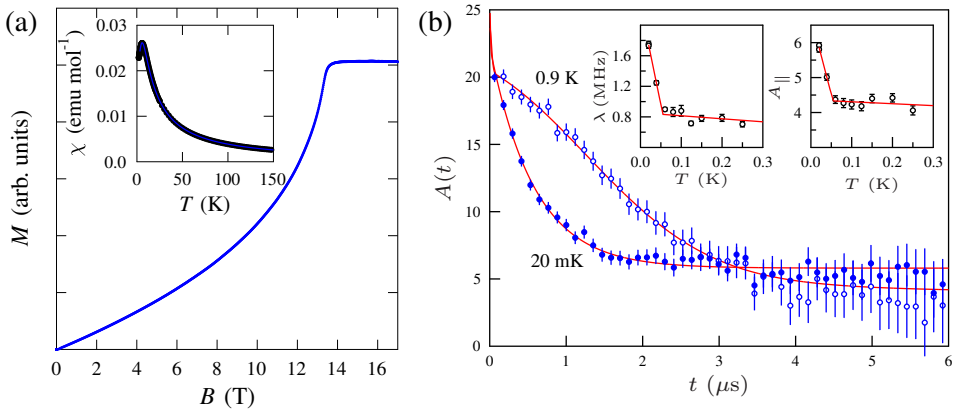

Figure 6.2: (a) Magnetisation of $[Cu(pyz)(H_2O)(gly)_2](ClO_4)_2$ measured at 0.5 K. Inset: magnetic susceptibility measured in an applied field of 100 mT. (b) ZF μ^+SR spectra at 900 and 20 mK. Inset: relaxation rate (left) and longitudinal amplitude (right) as a function of temperature showing the magnetic transition at 0.05(1) K. In the insets red lines are a guide to the eye.

where the first term captures the very rapid depolarisation at early times ($\sigma_1 \sim 20 - 100$ MHz), probably due to muonium formation or molecular radical states of the muon, the second term captures the relaxation due to static disordered nuclear moments ($\sigma_2 = 0.48$ MHz), the third term captures the relaxation due to electronic moments, and the non-relaxing final term is a combination of a background contribution and the fraction of muons polarised parallel to the local magnetic field (expected to be 1/3 of the muons for a magnetically ordered polycrystalline sample). Although oscillations are not observed at any temperature, a sharp rise in the rate λ of relaxation due to electronic moments concomitant with a rise in the baseline amplitude $A_\parallel$ is observed at 40 mK. This behaviour has been observed previously in similar chain-like materials [149] and can be taken as strong evidence for the onset of long-range magnetic order below $T_N = 0.05(1)$ K. The interchain coupling can then be estimated from T_N and J using Eq. 5.12 to be $|J_\perp/J| \approx 2 \times 10^{-3}$ which provides a measure of

how well $[Cu(pyz)(H_2O)(gly)_2](ClO_4)_2$ approximates the ideal Q1DQHAF (for which $|J_\perp/J| = 0$). Based on this estimate $[Cu(pyz)(H_2O)(gly)_2](ClO_4)_2$ is a better approximation to the ideal Q1DQHAF than $Cu(pyz)(NO_3)_2$ [63] where $|J_\perp/J| = 4.4 \times 10^{-3}$, but less well so than Sr_2CuO_3 where $|J_\perp/J| \approx 7 \times 10^{-4}$ (based on $T_N \approx 5$ K [177] and $J = 2600$ K [178]) and the organic radical-ion salt DEOCC-$TCNQF_4$ [179] where $|J_\perp/J| < 10^{-4}$.

6.3 A dimer system: $[Cu(pyz)(gly)](ClO_4)$

6.3.1 Structure

$[Cu(pyz)(gly)](ClO_4)$ crystallises in the space group $P2_1/n$. In contrast to $[Cu(pyz)(H_2O)(gly)_2](ClO_4)_2$ its structure (Fig. 6.3) is based on a lattice of alternating Cu^{2+} dimers linked with pyrazine ligands through which the primary exchange takes place. The dimers are tethered together with gly bridges forming corrugated sheets with non-coordinating ClO_4^- ions between these sheets. The exchange through gly groups and ClO_4^- ions might be expected to be relatively weak, suggesting that the magnetism of this material is due to weakly interacting dimer units.

6.3.2 Zero-field ground state

Zero-field (ZF) and longitudinal field (LF) μ^+SR experiments were performed down to 32 mK on the HiFi instrument at ISIS. A polycrystalline sample was mounted on the cold-finger of a dilution refrigerator. No sign of magnetic order or any sizeable relaxation due to electronic moments was observed above 32 mK. Instead the spectra shown in Fig. 6.4(a) display a Gaussian relaxation typical

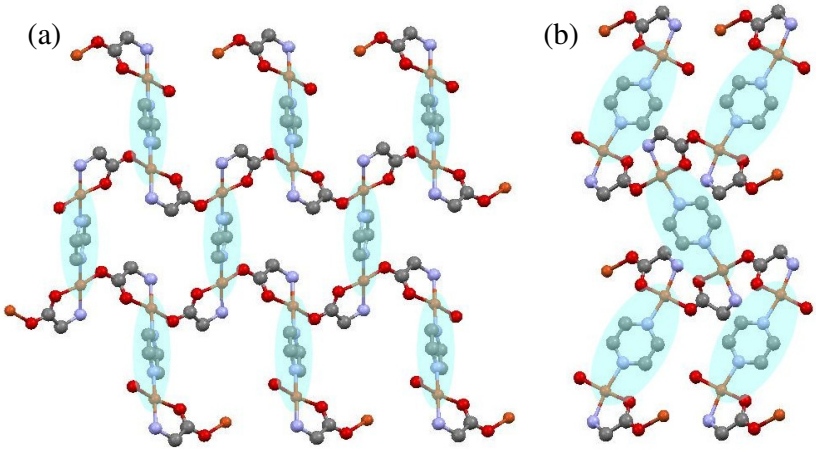

Figure 6.3: Structure of [Cu(pyz)(gly)](ClO$_4$)(a) along the a-axis and (b) along the c-axis showing pairs of Cu^{2+} ions strongly coupled magnetically *via* pyrazine ligands forming alternating dimers. Dimers are shaded and ClO_4^- ions have been omitted for clarity. Colour scheme: Cu (orange), O (red), N (blue) C (grey), H (white).

of disordered nuclear moments. A small longitudinal field was found to rapidly quench any relaxation confirming the picture that the ZF μ^+SR relaxation is due to disordered static nuclear magnetism with rapidly-fluctuating electronic moments that are motionally narrowed from the spectra.

The magnetic susceptibility of [Cu(pyz)(gly)](ClO$_4$) is shown in Fig. 6.4(b), measured along the long axis of a crystallite. The data are well described by the Bleaney-Bowers model of non-interacting antiferromagnetically-coupled dimers [180]

$$\chi = \frac{2Ng^2\mu_B^2}{k_B T} \frac{1}{3 + \exp(-J_0/k_B T)}, \tag{6.3}$$

where N is the number of dimers with intradimer exchange J_0, g-factor g, T is temperature, k_B Boltzmann's constant, and μ_B the Bohr magneton. A fit to Eq. 6.3 yields the intradimer exchange strength $J_0 = 7.5(1)$ K with $g_{HC} = 2.3$. The fit is improved slightly if a small ferromagnetic interdimer exchange of 2 K is allowed for [then the best fit yields $J_0 = 8.1(1)$ K].

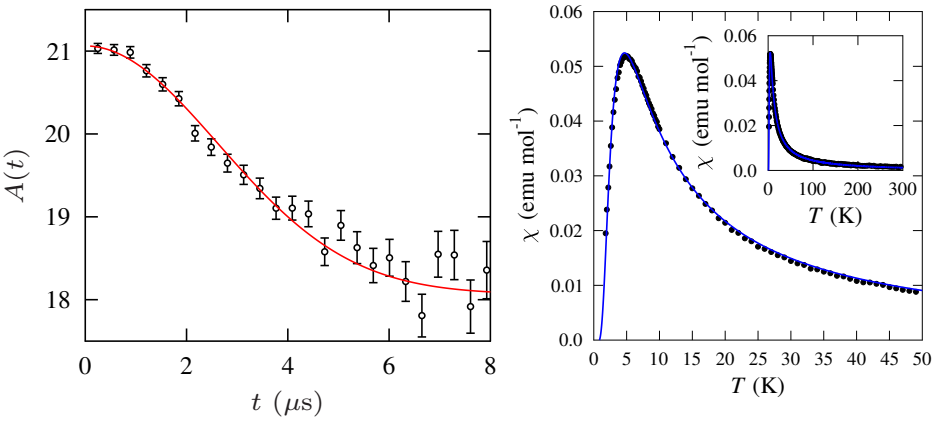

Figure 6.4: (a) Zero-field asymmetry. (b) Magnetic susceptibility of [Cu(pyz)(gly)](ClO_4) measured in a field of 5 mT. The solid line is a fit to the Bleaney-Bowers model of non-interacting dimers.

These results suggest that the magnetism in [Cu(pyz)(gly)](ClO_4) can be described by the Hamiltonian

$$\mathcal{H} = J_0 \sum_i \mathbf{S}_{1,i} \cdot \mathbf{S}_{2,i} + \sum_{\langle mnij \rangle} J_{mnij} \mathbf{S}_{m,i} \cdot \mathbf{S}_{n,j} - g\mu_B B \sum_{m,i} S^z_{m,i}, \qquad (6.4)$$

where the first term is the antiferromagnetic ($J_0 > 0$) intradimer interaction between the spins forming a dimer, $\mathbf{S}_{m,i}$ denote spins on site m in dimer i, the second term is the interdimer interaction, and $\langle\rangle$ denotes a sum over nearest neighbours, and the third term is the Zeeman interaction of all spins with an applied magnetic field B in the z-direction. If J_{mnij} is sufficiently weak compared to J_0 this Hamiltonian leads to a ZF ground state with total dimer spin $S = 0$ and a triply degenerate $S = 1$ excited state of energy J_0. Any dimers excited into the triplet state can be associated with the presence of a bosonic $S = 1$ triplon. For $J_{mnij} = 0$ the system remains quantum disordered down to absolute zero in the absence of an applied field [31].

6.3.3 Triplon condensation in applied field

In an applied magnetic field, the $S^z = 1$ mode in Eq. 6.4 softens and the Zeeman term acts like a chemical potential and can be used to control the density of triplons. Indeed experimentally, [Cu(pyz)(gly)](ClO$_4$) is found to undergo a magnetic phase transition in an applied field. The transition is seen in transverse field (TF) and LF μ^+SR as well as in heat capacity (HC), and dynamic susceptibility (χ) measurements.

TF μ^+SR measurements were performed on a polycrystalline sample on the LTF instrument, PSI. A magnetic field was applied at approximately 56° to the direction of the initial muon spin polarization and the transverse relaxation was followed as a function of applied field. The signals detected in two detectors placed on opposite sides of the sample were fitted simultaneously. In each of the detectors d, the positron count rate $N(d,t)$ was fitted to

$$\begin{aligned}\frac{N(d,t) - N_{\mathrm{BG}}(d)}{N_0(d)\, e^{-t/\tau_\mu}} =& 1 + A(d)\cos[\gamma_\mu B\, t + \phi(d)] \\ & \times [(1 - f_{\mathrm{G}})e^{-\lambda t} + f_{\mathrm{G}} e^{-(\gamma_\mu B_{\mathrm{rms}} t)^2/2}],\end{aligned} \tag{6.5}$$

where $N_{\mathrm{BG}}(d)$ is the background count rate, $N_0(d)$ the signal count rate, $A(d)$ is the asymmetry amplitude, $\phi(d)$ the detector phase, $\tau_\mu \approx 2.2$ μs the muon lifetime, γ_μ the muon gyromagnetic ratio, f_{G} the fractional amplitude of the Gaussian relaxation, and 0.08 MHz $< \lambda <$ 0.23 MHz. The transverse relaxation is described similarly well by two Gaussians (with different relaxation rates); this parameterization, however, provides a slightly better fit. Two signal fractions relaxing at different rates were required to provide an accurate description of the data in either case. Example asymmetry data are shown in Fig. 6.5(a) and (b)

where the asymmetry $A(t)$ is given by

$$A(t) = \frac{N'(d_1,t) - \alpha N'(d_2,t)}{N'(d_1,t) + \alpha N'(d_2,t)}, \tag{6.6}$$

where $N'(d,t) = N(d,t) - N_{\mathrm{BG}}(d)$ and $\alpha = N_0(d_1)/N_0(d_2)$ is a field-dependent experimental calibration constant accounting for different detector sensitivities.

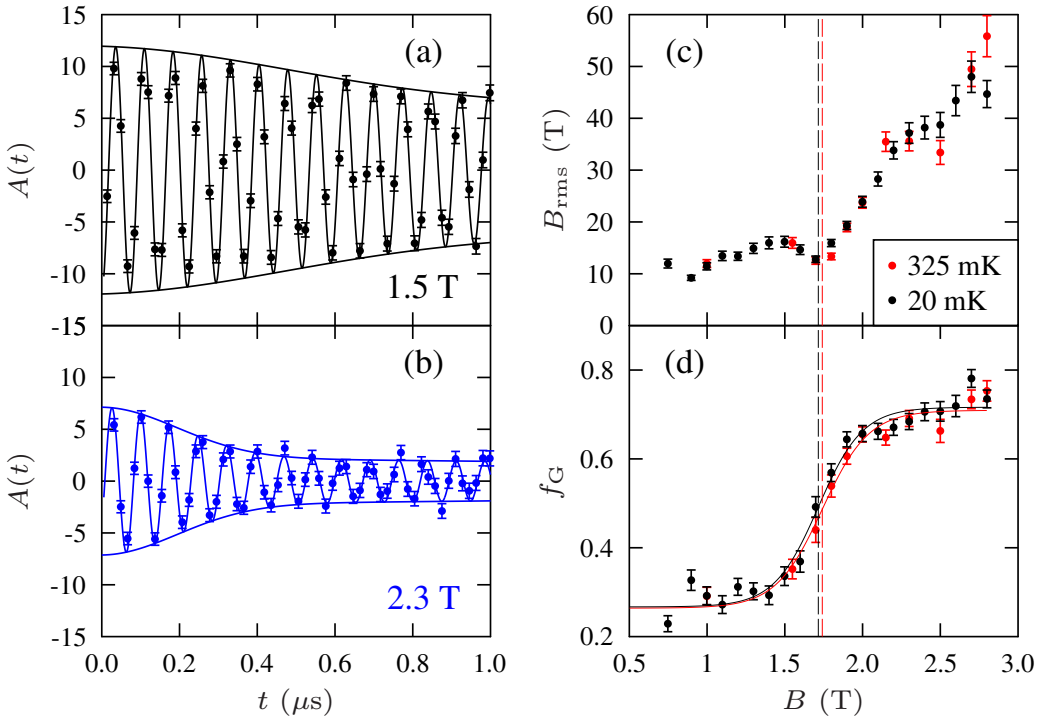

Figure 6.5: (a)-(b) Transverse field data taken on LTF at 19 mK in (c) 1.5 T and (d) 2.3 T applied field. The data are shown in the 'rotating reference frame' rotating at $B-0.1$ T hence oscillations are observed at $\gamma_\mu \times 0.1$ T $= 13.6$ MHz. (c) B_{rms} and (d) fraction of Gaussian relaxation f_{G} as a function of applied transverse field showing transitions at 1.72(6) and 1.74(8) T at 20 and 325 mK, respectively.

Fig. 6.5(c) and (d) show B_{rms} and the Gaussian signal fraction f_{G} as a function of applied field B. A sharp increase in the relaxation and hence the distribution of (static) fields B_{rms} experienced by the muon is observed at 1.72(6) and 1.74(8) T at 20 and 325 mK, respectively, concomitant with a sharp increase

in the Gaussian-shaped relaxing fraction of the signal. The critical fields were obtained by fitting a finite-temperature step function to f_G. These data provide strong evidence of a transition to a long-range ordered state in the bulk of the sample. The observed signal is similar to that observed for field-induced transitions in the related material $[Cu(HF_2)(pyz)_2]BF_4$ [163] (see Sec. 6.3.4) as well as the BEC candidate material $Pb_2V_3O_9$ [181]. Note that a fraction of the signal ($\sim 25\%$) continues to relax at a much smaller rate in the ordered phase. This is most likely a background contribution due to muons stopped in the sample holder or cryostat tail.

In addition to the TF measurements performed on LTF, extensive LF data were taken on the HiFi instrument at ISIS. Example data are shown in Fig. 6.6(a). The asymmetry $A(t)$ was fitted to

$$A(t) = A_{\mathrm{rel}} \exp\left[-(\lambda t)^{\beta}\right] + A_{\mathrm{nr}}, \tag{6.7}$$

where for the field scans the relaxing amplitude A_{rel} and $\beta = 1$ were held constant[1] and for the temperature scan the sum of A_{rel} and the non-relaxing asymmetry A_{nr} was held constant, reflecting the fact that the initial asymmetry should stay constant regardless of the applied field. An alternative method of analysing the data considered the time-integrated asymmetry A_{int}. A_{int} was approximately corrected for the effect of the magnetic field on the decay positrons by subtracting a straight-line fit to A_{int}. The relaxation rate λ and corrected integrated asymmetry $A_{\mathrm{int}}^{\mathrm{corr}}$ versus field obtained at a number of temperatures are shown in Fig. 6.6. Two features in λ and $A_{\mathrm{int}}^{\mathrm{corr}}$ are found to coincide and are present over the whole range

[1] While the temperature scan discussed below allows the changes in A_{rel} and β to be quantified, the level of noise encountered during the field scans precludes fitting the field scan data with this many degrees of freedom. Note that the baseline asymmetry is highly field dependent.

of temperatures considered (65-1750 mK). These two features are located around 1 T and 2–2.5 T applied field. Around these field values, the applied field focusses the muon beam to a particularly small spot size [shown in Fig. 6.6(e)] [182]. The sample was mounted centrally in the beam so a smaller muon spot size would be expected to yield a larger signal fraction from the sample and a smaller signal fraction from the silver backing plate. The increased relaxation (and therefore reduced integrated asymmetry) observed in the data is therefore to be expected as the muon relaxation in the sample should exceed the muon relaxation rate in silver. These features therefore primarily constitute a previously unknown instrument background and do not directly reflect any changes in the magnetic state of the sample[2]. However, an additional peak is present in λ around 1.7 T in the 65 mK and 650 mK data, but not in the 1.75 K data set. The location of this peak is consistent with the position of the phase boundary determined from TF μ^+SR above, as well as determined using thermodynamic measurements (discussed below). The thermodynamic measurements also demonstrate that the highest critical at the top of the dome in the phase diagram (shown in Fig. 6.8) is located around 1.3 K, consistent with the absence of the peak in λ around 1.7 T in the 1.75 K data. There is therefore strong evidence that the peaks in the longitudinal relaxation rate λ observed around 1.7 T are a signature of critical magnetic dynamics around the magnetic phase transition. Similar behaviour of the longitudinal relaxation is found at the ordering transitions in many related molecular magnets [163] and reflects the critical magnetic dynamics in the sample.

It was possible to unambiguously identify the magnetic transition using a temperature scan performed at a fixed longitudinal field of 3 T [see Fig. 6.6(a) and

[2]While the detailed shape of this background can be expected to depend on sample size, shape, and position as well as on the cryostat used, this background was also found in a number of other LF μ^+SR measurements on HiFi discussed in Sec. 6.5 below.

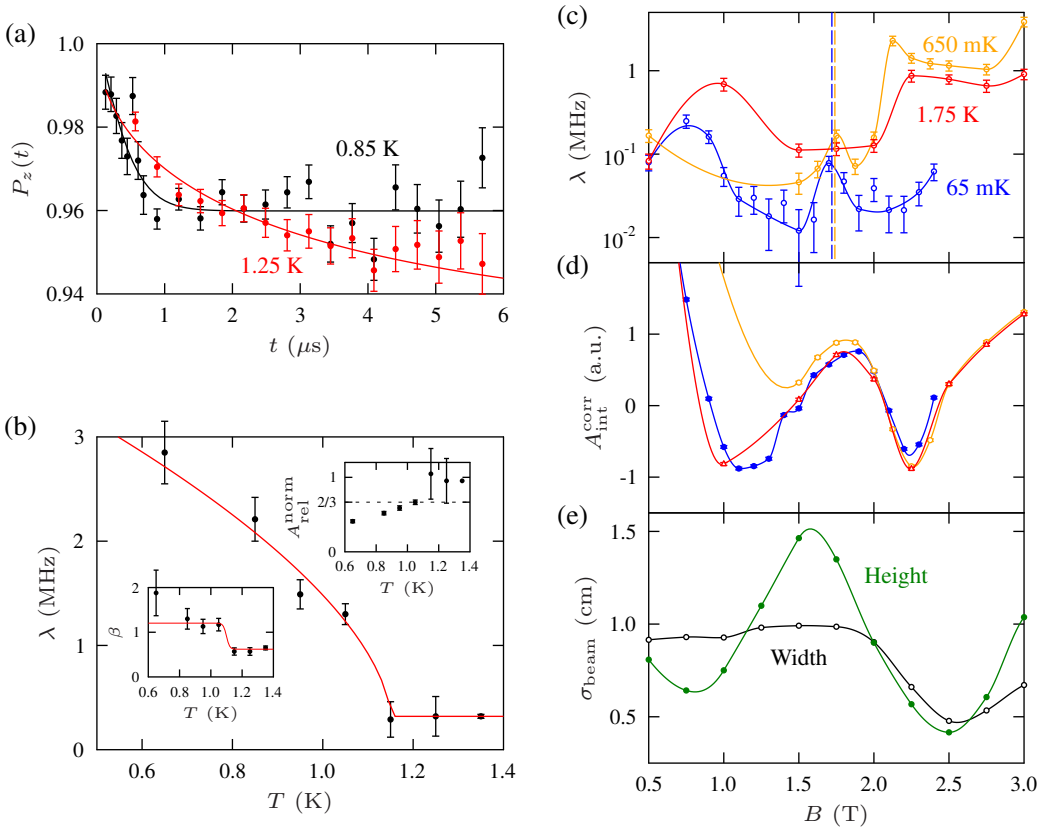

Figure 6.6: Summary of LF μ^+SR measurements for [Cu(pyz)(gly)](ClO$_4$) in applied field. (a) μ^+SR spectra in a longitudinal field of 3 T. (b) Relaxation rate against temperature at a constant LF of 3 T, inset: temperature dependence of β (bottom) and the normalised relaxing asymmetry (top). The relaxing asymmetry is normalised to its average for $T \geq 1.15$ K. (c) Relaxation rate versus field at constant temperature showing features around 1 T, 1.7 T, and 2.3 T at 65 mK and 650 mK and only around 1 T and 2.3 T at 1.75 K. The vertical stripes indicate the location of the transition identified with TF μ^+SR at 20 mK (blue) and 325 mK (orange), respectively. (d) Corrected time-integrated asymmetry showing features around 1 T and 2.3 T. (e) Gaussian size of muon beam [182] showing minima in beam size around 1 T and 2.5 T. In (b)–(e) solid lines are guide to the eye.

(b)]. A temperature scan has the advantage of avoiding the complicated field-dependent background found above. At a longitudinal field of 3 T, a sharp rise in the relaxation rate with a shape resembling that expected for an order parameter was observed below 1.15(5) K. Simultaneously the lineshape parameterised by β changes, indicating a more static distribution of fields experienced by the muon and the baseline asymmetry rises by approximately $A_{\mathrm{rel}}(T \geq 1.15\ \mathrm{K})/3$ as expected for the development of static magnetic order in a randomly-oriented polycrystalline sample. The further drop of the relaxing asymmetry below 1.15 K is due to the reduced instrument response to faster relaxation at a pulsed muon source. Similar parameterisations of the data yield identical results; the lineshape is well-described by a Gaussian for $T < 1.15$ K and a Lorentzian for $T \geq 1.15$ K. These findings demonstrate for the first time the sensitivity of LF μ^+SR for the study of a field-induced magnetic transition of this kind.

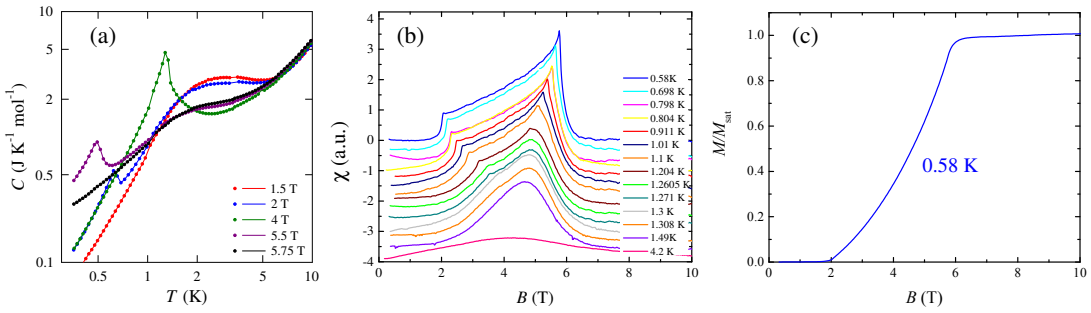

Figure 6.7: (a) Heat capacity and (b) dynamic susceptibility with the field normal to the (110) crystallographic plane (data offset for clarity) showing magnetic transitions in applied magnetic field. (c) Magnetisation at 0.58 K obtained by integrating the susceptibility.

The magnetic transition was also observed as sharp peaks in heat capacity and dynamic susceptibility measurements shown in Fig. 6.7. Heat capacity measurements were performed on a single crystal in the same orientation as for the dc susceptibility shown in Fig. 6.4 using field scans covering the 2–6 T region over

temperatures from 0.2–1.4 K. Single crystal dynamic susceptibility measurements were performed using a radio-frequency based susceptometer [183]. The dynamic susceptibility $\chi = dM/dB$ was measured in two different orientations (i) with the magnetic field applied close to the normal to the (110) planes — i.e. with the field parallel to the *a*-*b* plane containing the dimers — or (ii) with the field perpendicular to the (122) crystallographic planes.

6.3.4 Discussion

The compiled phase diagram of [Cu(pyz)(gly)](ClO_4) is shown in Fig. 6.8. The positions of the phase boundaries differ slightly between the different measurements, reflecting g-factor anisotropy. The phase boundaries are found to coincide if $g_\chi^{(110)} = 2.18$, $g_\chi^{(122)} = 2.15$, $g_{\mu SR} = 2.2$, and $g_{\rm HC} = 2.3$, which are typical for Cu-based transition metal coordination polymers [149].

The phase diagram of [Cu(pyz)(gly)](ClO_4) is consistent with weakly ferromagnetically-coupled dimers. At temperatures well below the intradimer exchange J_0 the system is a quantum disordered paramagnet formed from a sea of singlets [18; 31; 184]. The applied field (taken along z) closes the singlet-triplet gap *via* a quantum critical point at $g\mu_{\rm B}B_{\rm c1}$. For $B_{\rm c1} < B < B_{\rm c2}$ the system exhibits XY magnetic order as the transverse spin components $\langle S_x \rangle$ and $\langle S_y \rangle$ spontaneously break the rotational $O(2)$ symmetry of the spin Hamiltonian in Eq. 6.4. Further application of the field for $B_{\rm c1} < B < B_{\rm c2}$ increases the magnetisation of the system as the spins start to cant towards z until the spins become fully polarised at a second QCP at $B = B_{\rm c2}$.

In a mean-field approximation [184] the upper phase boundary occurs at $g\mu_{\rm B}B_{\rm c2} = J_0$ for ferromagnetically-coupled dimers, which yields $J_0 = 9.0(2)$ K, consistent with the value derived from the dc susceptibility. The lower phase

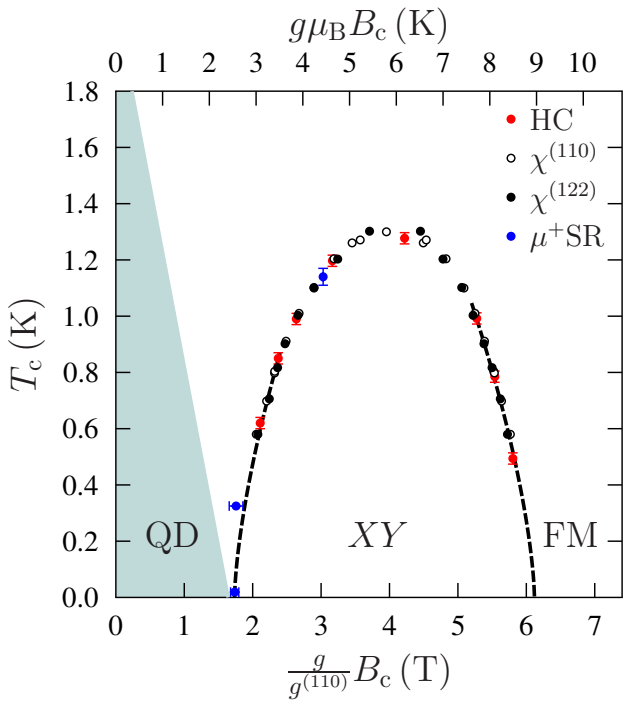

Figure 6.8: The phase diagram of [Cu(pyz)(gly)](ClO_4) compiled from μ^+SR, heat capacity, and dynamic susceptibility measurements, showing QCPs at $g\mu_B B_c = 2.5(1)$ K and 9.0(2) K. Dashed lines indicate critical behaviour expected for a BEC of triplons with exponent $\phi = 2/3$. Shading indicates the spin gap $\Delta = g\mu_B(B_{c1} - B)$ for $B < B_{c1}$.

boundary is predicted at $g\mu_B B_{c1} = J_0 - z|J_1|/2$, where $J_1 = \langle J_{mnij} \rangle$ is the interdimer exchange of each Cu ion with z nearest neighbours. Assuming $z = 4$ (each Cu ion has four roughly equidistant neighbours within 7 Å excluding the other Cu ion in the dimer) $g\mu_B B_{c1} = 2.5(1)$ K yields $|J_1| = 3.2(2)$ K. If instead the interdimer coupling was antiferromagnetic, the critical fields are predicted to be $g\mu_B B_{c1} = J_0 - z|J_1|/2$ and $g\mu_B B_{c2} = J_0 + z|J_1|$ yielding an intradimer coupling of $J_0 = 4.7(1)$ K that is not consistent with the dc susceptibility [$|J_1|$ would be 1.08(2) K].

Dimer systems are frequently discussed in the context of the Bose-Einstein condensation of triplons. The spin Hamiltonian in Eq. 6.4 can be rewritten in

second-quantised form as [31]

$$\mathcal{H} = \sum_i (J_0 - h) a_i^\dagger a_i + \sum_{i,j} t_{ij} a_i^\dagger a_j + \frac{1}{2} \sum_{i,j} U_{ij} a_i^\dagger a_j^\dagger a_j a_i, \tag{6.8}$$

where $a_i^\dagger$ (a_i) creates (annihilates) a triplon on dimer i and $h = g\mu_B B$. The term containing t_{ij} is generated by the coupling of transverse spin components $S_{m,i}^x S_{n,j}^x + S_{m,i}^y S_{n,j}^y$ and describes triplon hopping between sites i and j. U_{ij} is the triplon repulsion arising from the longitudinal term $S_{m,i}^z S_{n,j}^z$ when triplons occupy neighbouring dimers i and j. The rotational $O(2)$ symmetry of the spin Hamiltonian is isomorphic to the $U(1)$ symmetry of the boson Hamiltonian. The density of triplons is controlled by the applied field, which acts like a chemical potential.

The singlet ground state in spin language corresponds to the triplon vacuum in the boson picture. Above the first QCP triplons condense and the canted spin state can be described by a superposition of singlet and $S^z = +1$ triplet $|\psi\rangle_i = \alpha_i |0,0\rangle_i + \beta_i |1,1\rangle_i$, where $\alpha_i = 1$ and $\beta_i = 0$ for $B = B_{c1}$ and $\alpha_i = 0$ and $\beta_i = 1$ for $B = B_{c2}$ (at zero temperature) so that at saturation each site is occupied by exactly one triplon. The angle of the spin for the transverse XY order can be mapped onto the phase of the triplon wavefunction, which represents the $U(1)$ order parameter [31].

The critical properties of the condensate in the vicinity of the QCP are determined by the BEC universality class; close to the QCP the phase boundary follows $T_c \propto (B - B_{c1})^\phi$ (close to B_{c1}) and $T_c \propto (B_{c2} - B)^\phi$ (close to B_{c2}), where $\phi = 2/3$ for quadratically dispersing triplons in three dimensions [18; 31]. BEC of triplons has been observed in a number of dimer-based magnetic insulators such as $A\mathrm{CuCl_3}$ (A = Tl, K, NH_4), $BaCuSi_2O_6$, $Cu(NO_3)_2 \cdot 2.5H_2O$,$Cs_3Cr_2Br_9$,

$(CH_3)_2CHNH_3CuCl_3$, and $(C_4H_{12}N_2)Cu_2Cl_6$ (see Ref. 31 and references therein). The $\phi = 2/3$ power-law dependence of the phase boundary in the critical region is consistent with our data, although the scarcity of data close to the QCP prevents a rigorous assessment.

Note also that rotational $O(2)$ symmetry of the spin Hamiltonian [isomorphic to $U(1)$ symmetry of the boson Hamiltonian] is essential for the realisation of the triplon BEC. Any real system may have symmetry breaking terms in the Hamiltonian arising from weak anisotropic interactions such as crystalline anisotropies, spin-orbit coupling, and dipolar interactions[3]. So far the energy scale of these interactions has not been characterised in $[Cu(pyz)(gly)](ClO_4)$. In particular it is not possible to rule out a small Dzyaloshinskii-Moriya (DM) interaction $\mathbf{D}_{ij} \cdot (\mathbf{S}_i \times \mathbf{S}_j)$ in the Hamiltonian. Even though inversion centres exist between neighbouring dimers with the same orientation (implying that between those $\mathbf{D}_{ij} = \mathbf{0}$ by symmetry), neighbouring dimers of different orientation are related by a glide plane, implying a non-zero DM interaction $\mathbf{D}_{ij}$ within the *a*-*c* plane, which, if not directed along *c*, would break the XY symmetry in the *a*-*b* plane. Small symmetry-breaking terms can (once characterised) be accounted for in a theoretical treatment and hence do not rule out future theoretical work on this compound in the context of BEC of triplons.

Finally, it is interesting to compare the phase diagram of $[Cu(pyz)(gly)](ClO_4)$ to the phase diagram of the Q2D QHAFM $[Cu(HF_2)(pyz)_2]BF_4$ reproduced in Fig. 6.9 which inspired this work on $[Cu(pyz)(gly)](ClO_4)$. Unlike $[Cu(pyz)(gly)](ClO_4)$, $[Cu(HF_2)(pyz)_2]BF_4$ does not dimerise and orders antiferromagnetically in zero field below $T_N = 1.63$ K [14]. In an applied magnetic field,

[3]Here lies an important advantage of studying BEC in cold atomic gases where the $U(1)$ symmetry is exact [31].

mean field theory predicts a monotonic decrease of T_N with field due the suppression of the amplitude of the order parameter by polarising the spins along a certain direction. However, this misses the effect of the applied field on the phase fluctuations, which are reduced by changing the order parameter space from a sphere to a circle. The relevant energy scales are determined by a Berezinsky-

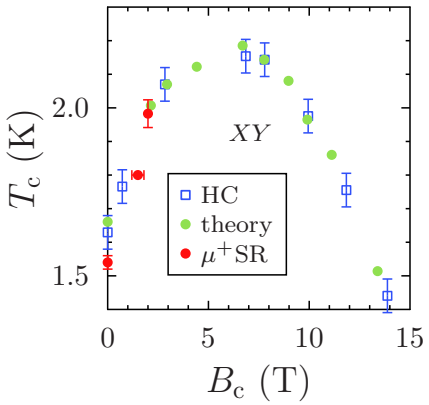

Figure 6.9: The phase diagram of [Cu(HF$_2$)(pyz)$_2$]BF$_4$, adapted from Ref. 163 and 14. The phase boundary separates an XY long-range ordered state from a paramagnetic one at low-fields and from the fully saturated phase at high fields. The boundary was determined experimentally using heat capacity [14] (HC) and TF μ^+SR [163] and is compared with the theoretical prediction based on the stochastic series expansion quantum Monte Carlo method [14]. Copyright American Physical Society.

Kosterlitz-Thouless (BKT) mechanism [9; 10; 12; 13] and the interlayer coupling $J_\perp$. The consequence of this is an unusual non-monotonic field dependence of T_N. At low fields the suppression of the phase fluctuations is the dominant effect since in the 2D limit the phase fluctuations are responsible for preventing magnetic order. This leads to an increase in T_N at low fields. At high fields on the other hand the suppression of the amplitude of the order parameter becomes dominant driving T_N down to zero at a critical field $g\mu_B B_c = 4J_\parallel + 2J_\perp$ [14]. It is difficult to observe a BKT transition directly in Q2D systems due to the in-

terlayer coupling driving the system to order magnetically at finite temperature. The non-monotonic dependence of T_N is therefore valuable indirect evidence of the BKT physics at play. Using the stochastic series expansion quantum Monte Carlo method it was possible to make an accurate prediction [14] for the phase boundary of $[Cu(HF_2)(pyz)_2]BF_4$ which was verified by heat capacity (identifying a small anomaly at the transitions) [14] and TF μ^+SR measurments [163]. Hence the relevant physics in the two Q2D QHAFMs $[Cu(pyz)(gly)](ClO_4)$ and $[Cu(HF_2)(pyz)_2]BF_4$ is very different, yet the phase diagram of the two compounds share a similar field dependence of T_N. This highlights the versatility of transition metal coordination polymers and the wealth of physics that can be explored by studying them.

6.4 Conclusions

A combination of experimental techniques has been applied to study the magnetism in $[Cu(pyz)(H_2O)(gly)_2](ClO_4)_2$ and $[Cu(pyz)(gly)](ClO_4)$, two molecular magnets distinguished by their dimensionality that were synthesised from the same starting compounds using the same synthetic pathway. While $[Cu(pyz)(H_2O)(gly)_2](ClO_4)_2$ is best described as a Q1D QHAFM that orders at low temperatures, $[Cu(pyz)(gly)](ClO_4)$ is best described as a quantum-disordered dimer system that undergoes triplon condensation in an applied magnetic field. This work demonstrates the potential for creating still more exotic magnetic ground states from coordination polymers. TF and LF μ^+SR have been shown to be sensitive to the phase boundary in $[Cu(pyz)(gly)](ClO_4)$ and will play an important rôle in the future study of field-temperature phase diagrams, in particular with the advent of the new high-field spectrometer at PSI, enabling studies

in transverse or longitudinal fields up to 10 T. The next section discusses some of the remaining challenges for using LF μ^+SR to study the field-temperature phase diagram in a number of molecular quantum magnets.

6.5 Further LF μ^+SR measurements

In this section I describe further LF μ^+SR work on (i) the organic spin ladder system DIMPY, and (ii) the two molecular nanomagnets Cr_8Cd and Cr_8Mn. LF μ^+SR was used to study field cross-overs and level-crossing resonances. In principle, LF μ^+SR should offer some of the same advantages that ZF μ^+SR has over more conventional probes such as heat capacity, susceptibility and neutron scattering in systems where correlations develop well above the transition under study and moment sizes are small. Unfortunately in all three compounds discussed here, a similar field-dependent background as encountered for $[Cu(pyz)(gly)](ClO_4)$ above presents a significant challenge to the utility of LF scans using the HiFi instrument. These are among the first experiments performed on the HiFi instrument and the detailed understanding of the instrument response will be crucial for any future LF experiments on the HiFi spectrometer.

The experiments described here were performed by myself, Tom Lancaster, Peter Baker, Francis Pratt, and Stephen Blundell. All data analysis presented here was performed by myself.

6.5.1 A spin ladder in the strong-leg regime

Spin ladders present a class of low-dimensional quantum magnets that occupy a regime of subtle behaviour which lies between the stark extremes of a one-dimensional chain and a two-dimensional plane. They are characterised by two

antiferromagnetic exchange constants: J_{rung} along the rungs of the ladder and J_{leg} along the ladder legs. Remarkably, the spin excitation spectrum for a spin ladder is gapped for an even number of legs and gapless for an odd number; a phenomenon — reminiscent of the Haldane gap in antiferromagnetic integer spin chains — which has received great theoretical and experimental attention [18; 30]. For even-legged ladders a $T = 0$ quantum phase transition to a gapless phase can be driven by an applied magnetic field, where the nature of the gapless phase depends crucially on the dimensionality of the system. For ladders with significant two or three-dimensional interactions, for which the dimer system $[\mathrm{Cu(pyz)(gly)}](\mathrm{ClO_4})$ studied above can be considered an example, the gapless phase displays long-range antiferromagnetic order. For one-dimensional systems such as isolated spin ladders, however, long-range magnetic order is prevented by divergent phase fluctuations and, instead, a spin Luttinger liquid (LL) is realised. The LL state is characterised by algebraically decaying spin-correlations and due to the absence of long-range order the LL regime is reached from the gapped phase *via* a cross-over rather than a phase transition.

Unfortunately, the range of physical systems with suitable energy scales is scarce. Most of the best studied ladder systems are based on copper-oxide, where the large exchange constants preclude a detailed study of the phase diagram; for example in the spin-1/2 ladder compound $\mathrm{SrCu_2O_3}$ the gap $\Delta \geq 400$ K corresponds to a hopeless $B_{\mathrm{c}} \geq 300$ T ($g = 2$) [185]. Molecular systems offer the advantage of much smaller exchange interactions, and therefore accessible energy scales as well as a high degree of tunability. The strong-rung ($J_{\mathrm{rung}} > J_{\mathrm{leg}}$) material $(\mathrm{C_5H_{12}N})_2\mathrm{CuBr_4}$ was the first spin-1/2 two-leg ladder to be studied in detail using thermodynamic measurements [29], nuclear magnetic resonance (NMR) [186], neutron diffraction [187], and inelastic neutron scattering (INS) [188]. These have

identified the 1d LL regime in the gapless phase above a 3d XY antiferromagnetic phase where interladder interactions drive the system to order magnetically.

In this section I discuss LF μ^+SR experiments on the novel molecular spin-ladder bis(2,3-dimethylpyridinium) tetrabromocuprate [or $(C_7H_{10}N)_2CuBr_4$, hereafter DIMPY] [189]. Crystal structure, density functional theory calculations of the exchange constants, and susceptibility measurements suggest that DIMPY is the first example of a spin-1/2 two-leg spin-ladder in the strong leg regime with $J_{\text{leg}} \approx 1.94\, J_{\text{rung}}$ [189]. The strong-leg regime is particularly interesting because quantum fluctuations are more pronounced in this regime and hence the singlet in the gapped phase will be more delocalized — a state reminiscent of Anderson's famous *resonating valence bond* [190]. INS and heat capacity measurements performed by Hong *et al.* [191] found that the ground state of DIMPY is highly one-dimensional with a gap that may be closed in an applied field. The heat capacity in the gapless phase takes the asymptotic linear shape characteristic of a LL and the critical field was determined to be $\mu_0 H_{\text{c1}} = 3.0(3)$ T. Comparison of the triplon excitation spectrum obtained through INS with perturbative continuous unitary transformation calculations yield an estimated ratio of $J_{\text{leg}} \approx 2.2\, J_{\text{rung}}$. Hong *et al.* found no evidence for a long-range ordered phase in their measurements down to 150 mK. More recently two independent studies have found small λ-anomalies indicating long-range order in the gapless phase below a maximum critical temperature of approximately 300 mK [192; 193]. High-field magnetisation [194] has confirmed the lower critical field and provided a value for the upper critical field $H_{\text{c2}} = 29$ T, above which the system is fully polarised and a gap reopens, this value is consistent with a later density matrix renormalisation group calculation [193]. Further INS work has been reported very recently [195; 196].

Here LF μ^+SR was used to study the phase diagram of DIMPY. This is the

first study of the field-induced cross-over into a LL regime in a spin ladder using μ^+SR. A mosaic of single crystals was mounted on a silver backing plate fixed to the cold finger of a dilution refrigerator (DR). DR measurements were performed for $T \leq 4.5$ K and measurements at $T \geq 4.5$ K were performed in a closed-cycle refrigerator (CCR).

Example μ^+SR spectra are shown in Fig. 6.10. In ZF the asymmetry takes the shape of a slowly-relaxing Gaussian and any relaxation is rapidly quenched in a small magnetic field, indicating the absence of magnetic order down to at least 100 mK in zero field. The relaxation recovers significantly in the 2.5 T and 4–4.5 T regions. Unlike for [Cu(pyz)(gly)](ClO_4), the relaxation is never better described by a Gaussian than by a Lorentzian. As before, two alternative approaches to analyse the data were used. The first is fitting the asymmetry to the function

$$A(t) = A_{\mathrm{rel}} \exp\left(-\lambda t\right) + A_{\mathrm{nr}}, \tag{6.9}$$

where the relaxing asymmetry A_{rel} was kept fixed and A_{nr} is a constant. The second method simply examines changes in the time-integrated asymmetry, correcting for positron beam optics by subtracting a straight-line fit.

The results of the analysis are presented in Fig. 6.10. Two peaks are observed in the relaxation rate that coincide with three dips observed in the asymmetry around 2.5 T and 4–4.5 T. The peaks in λ and dips in integrated asymmetry are located close to the minima of the muon beam spot size. If the sample is located at the centre of the beam, the background due to muons stopping in the silver backing plate (which can be expected to be a very slow relaxation) will be reduced and more of the signal will originate from the sample. Hence the increase in relaxation close to the minima of the beam spot is encouraging and indicates

that the sample depolarises muons more rapidly than silver. From the linear dependence of the heat capacity the upper boundary of the LL regime has been estimated to be 0.5–1 K around 5 T [191; 192] in addition to an estimate of the long-range ordering temperature of up to 100–200 mK below the 4.7 T upper limit of the LF μ^+SR measurements. Therefore, over the temperature range covered with LF μ^+SR (100 mK–4.5 K) one or two changes in the muon response should be expected. While some temperature dependence is evident in the data shown in Fig. 6.10, for example the lower peak in λ is shifted towards higher fields for the 100 mK data, the background caused by the changes in the beam spot precludes firmer conclusions from the field scans.

However, the temperature scan shown in Fig. 6.10(c) is not affected by this complicated field-dependent background. The fits to Eq. 6.9 were performed keeping relaxing and baseline asymmetry fixed. While the relaxing asymmetry is very small, causing substantial difficulty in extracting changes in the relaxation rate, the longitudinal relaxation rate λ is seen to increase below approximately 1 K at 3.3 T, concomitant with a drop of the time-integrated asymmetry. This approximately corresponds to the estimated upper boundary of the LL regime. Though it is possible that this is a signature of the onsetting magnetic order at lower temperatures, this may indicate for the first time that μ^+SR *is* sensitive to the cross-over into a LL regime — a region where no long-range magnetic order is present and no symmetry is broken.

Also shown in Fig. 6.10 is the integrated asymmetry for DIMPY in the CCR and for a polycrystalline sample of $(C_7H_{10}N)Cl$ in the CCR. $(C_7H_{10}N)Cl$ was measured to examine whether the features in the muon response are due to molecular level crossing resonances of molecular radical states of the muon. $(C_7H_{10}N)Cl$ has the same molecular motif as DIMPY but lacks the magnetic $CuBr_4$ units; it

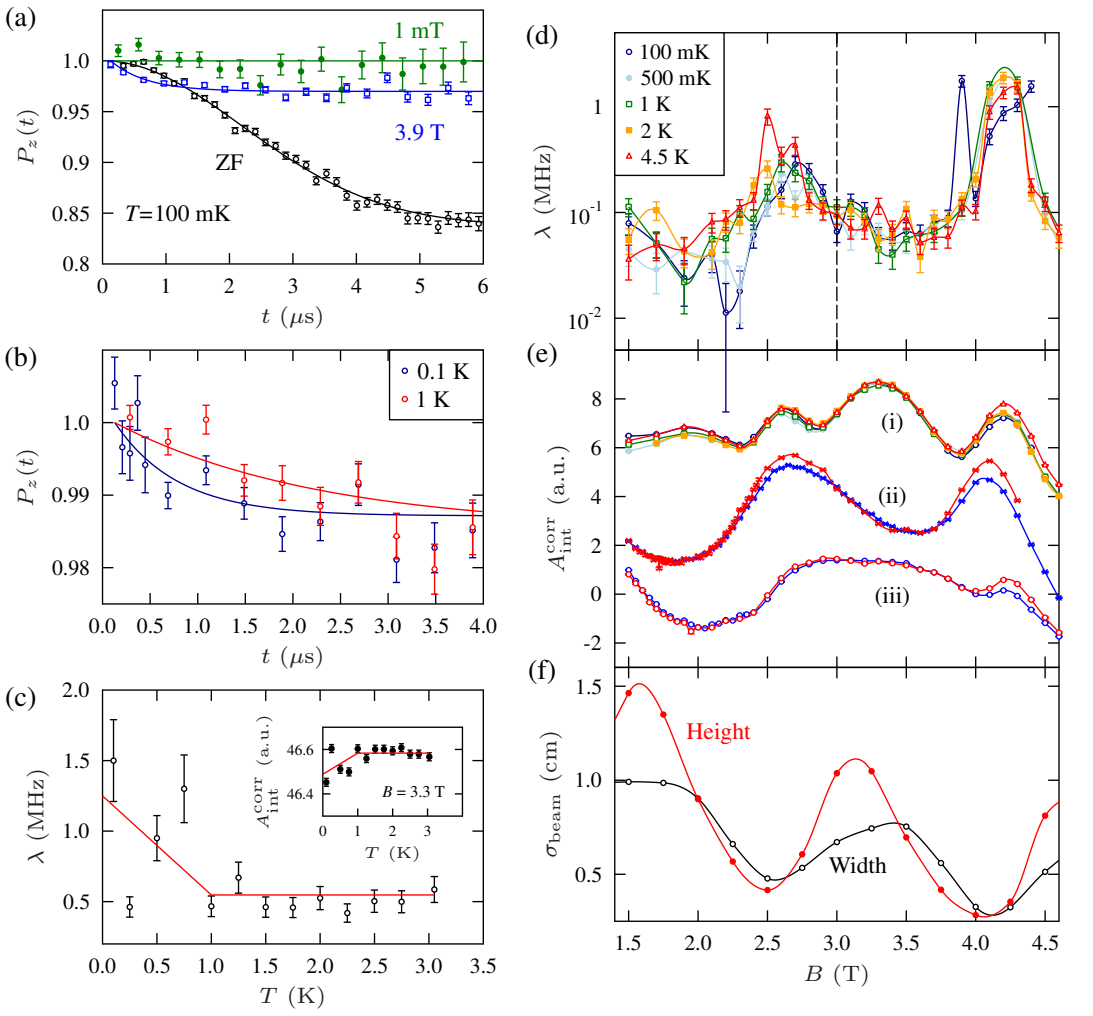

Figure 6.10: (a)–(d) data are for DIMPY in the DR. (a) Example asymmetry spectra at 100 mK. (b) Example asymmetry spectra at 3.3 T. (c) Longitudinal relaxation rate versus temperature in a LF of 3.3 T, inset: corrected time-integrated asymmetry for the same temperature scan. (d) Longitudinal relaxation rate versus applied field at various temperatures showing features around 2.3 T and 4 T. The vertical line indicates the position of the cross-over into the LL regime. (e) Corrected time-integrated asymmetry versus applied field for (i) DIMPY in the DR [same colour scheme as in (c)], (ii) DIMPY in the CCR at 20 K (blue) and 250 K (red), and (iii) $(C_7H_{10}N)Cl$ in the CCR at 4.5 K (blue) and 250 K (red). (f) Gaussian size of muon beam spot [182]. In (c)–(f) solid lines are a guide to the eye.

should therefore yield very similar molecular level-crossing resonances (if present) without any of the magnetic spin-ladder signal. The absence of any significant temperature dependence over the range 4.5 K–250 K for both DIMPY [shown as (ii) in Fig. 6.10(e)] and $(C_7H_{10}N)Cl$ [shown as (iii) in Fig. 6.10(e)] confirms that the muon response is not due to molecular level crossing resonances. These data serve to identify differences in the instrument background between the DR and CCR, as well as between single crystal and polycrystalline samples in the CCR.

In conclusion, the first LF μ^+SR experiments on LL physics were presented for the strong-leg spin ladder system DIMPY. The field scan data are dominated by an effect that can be ascribed to muon beam optics, but temperature scan data suggest a sensitivity of the experiments to either the low-temperature magnetically ordered phase or the cross-over into the LL regime. Future work on this compound will attempt to minimise this background through the use of very large samples. In particular, through more detailed measurements of the longitudinal relaxation as a function of temperature [see Fig. 6.10 (c)] at different applied fields, this may enable the nature of the interactions in the LL regime to be characterised. This would allow the results of very recent NMR measurements on this compound to be tested, which suggest that the interactions between the spinless fermions in the LL phase are attractive, a scenario that would be unprecedented in any LL [197].

6.5.2 Level-crossings in molecular nanomagnets

Molecular nanomagnets (MNMs) comprise clusters of transition metal ions linked by organic ligands [198]. Strong exchange coupling between these ions within a single molecule results in each molecule possessing a ground state described by a total spin eigenvalue S and z-component M. Excited states will possess

different values of S (split by the exchange coupling) or M (split by anisotropy). A level crossing takes place when two levels become degenerate due to the Zeeman splitting of the levels in an applied magnetic field. MNMs have been widely studied in recent years, most recently in anticipation of their possible deployment as elements of quantum computers [32], although much interest also centres on the quantum tunnelling of the magnetization (QTM) which can take place when the magnetic energy levels are at resonance [198] and the effects of frustration in odd-numbered rings, such as the systems studied here [199].

When muons were first used to study MNMs it was hoped that they would be sensitive to level crossings in these systems. However, early μ^+SR studies failed to observe any evidence for level-crossings between levels split by an anisotropy term [200]. Such crossings have been observed using μ^+SR in a broadly related inorganic system [201] and there is some μ^+SR evidence for effects ascribed to a matching of the MNM electronic energy levels (split mainly by exchange) with that of the muon hyperfine levels in a molecular grid system [202]. The level-crossing between levels of different M, i.e. those split by anisotropy, is highly angular dependent due to the angular dependence of the anisotropy term. This poses experimental challenges and usually requires aligned crystals or microcrystallites. On the other hand the level crossing between levels of different S, i.e. levels split by exchange, can be expected to exhibit a much weaker angular dependence, since the exchange is expected to be isotropic in most cases. Such crossings may therefore be more easily observed experimentally even in unaligned samples. Note that also historically a level-crossing between levels of different total spin S has been observed in a powder sample of $[Fe(OMe)_2(O_2CCH_2Cl)]_{10}$ [203] before the unambiguous observation of a level-crossing between levels of different M in aligned microcrystalline [204] and single crystal [205] samples of

$Mn_{12}O_{12}(CH_3COO)_{16}(H_2O)_4$.

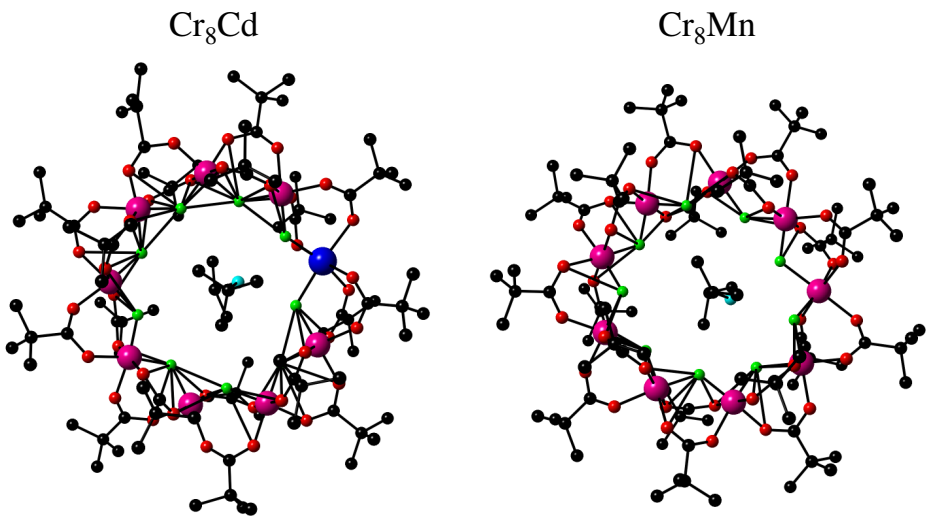

Figure 6.11: The structure of Cr_8Cd (left) [206] and Cr_8Mn (right) [199]. Cr (large, magenta), O (red), N (cyan), F (green), Cd (large, blue). The Mn site is disordered over the Cr positions, while the Cd site is thought to be ordered. H atoms are omitted for clarity.

This section is concerned with LF μ^+SR experiments on the MNMs $[H_2N^tBu^iPr][Cr_8CdF_9(O_2CC(CH_3)_3)_{18}]$ (hereafter Cr_8Cd) and $[(Me_2CH)_2NH_2][Cr_8MnF_9(O_2CCMe_3)_{18}]$ (hereafter Cr_8Mn). Cr_8Cd and Cr_8Mn are related to the octonuclear system $[Cr_8F_8(O_2CC(CH_3)_3)_{16}]$ (hereafter Cr_8) [207], which has a total $S = 0$ ground state due to strongly antiferromagnetically coupled Cr^{3+} $s = 3/2$ spins ($J_{Cr-Cr} \approx 16.9$ K).

Cr_8Cd in contrast can be viewed as a broken ring system due to the addition of a non-magnetic $s = 0$ Cd^{2+} ion to the ring [206]. The antiferromagnetic coupling between Cr^{3+} ions still leads to a total $S = 0$ ground state, but the difference in magnetic topology between Cr_8 and Cr_8Cd leads to the lowest-lying level crossing $S = 0 \rightarrow S = 1$ to take place at a critical field of $B_c = 2.3$ T compared to 7.3 T for Cr_8 [208], which is located above the 5 T maximum field currently accessible with European μ^+SR instruments.

Cr_8Mn is a rare example of an odd-membered ring of antiferromagnetically coupled spins [199]. To date only one other example of such a molecular ring system, Cr_8Ni, has been studied in detail [199; 209–211]. Odd-membered rings of antiferromagnetically coupled spins are particularly interesting since they permit the study of frustration as not all spins can simultaneously satisfy all of their magnetic interactions. The odd number of magnetic electrons (Mn^{2+}, $s = 5/2$) leads to a total spin $S = 1/2$ ground state. Recent inelastic neutron scattering experiments on Cr_8Mn have identified the lowest level crossing as $S = 1/2 \rightarrow S = 3/2$ at a critical field $B_c = 3.8$ T [212].

The low-lying levels can be described by the Hamiltonian

$$\begin{aligned}\mathcal{H} =& J_{\mathrm{Cr-X}}(\mathbf{s}^1_{\mathrm{Cr}} \cdot \mathbf{s}_{\mathrm{X}} + \mathbf{s}^8_{\mathrm{Cr}} \cdot \mathbf{s}_{\mathrm{X}}) + J_{\mathrm{Cr-Cr}} \sum_{i=1}^{7} \mathbf{s}^i_{\mathrm{Cr}} \cdot \mathbf{s}^{i+1}_{\mathrm{Cr}} \\ &+ \sum_{i=1}^{8} \mathbf{s}^i_{\mathrm{Cr}} \cdot \mathbf{D}^i_{Cr} \cdot \mathbf{s}^i_{\mathrm{Cr}} + \mathbf{s}_{\mathrm{X}} \cdot \mathbf{D}_X \cdot \mathbf{s}_{\mathrm{X}} \\ &- g_{\mathrm{Cr}}\mu_{\mathrm{B}} \sum_{i=1}^{8} \mathbf{s}^i_{\mathrm{Cr}} \cdot \mathbf{B} - g_{\mathrm{X}}\mu_{\mathrm{B}}\, \mathbf{s}_{\mathrm{X}} \cdot \mathbf{B},\end{aligned} \tag{6.10}$$

where $J_{\mathrm{Cr-Cr}}(J_{\mathrm{Cr-X}})$ is the exchange between Cr–Cr (Cr–X) ions with spins $\mathbf{s}$, $\mathbf{D}^i_{Cr}(\mathbf{D}_X)$ is the single-ion anisotropy tensor, B is the applied magnetic, $g_{\mathrm{Cr}}(g_{\mathrm{X}})$ the Cr (X) g-factor, μ_{B} the Bohr magneton, and $X = \mathrm{Cd}, \mathrm{Mn}$. Since Cd^{2+} is non-magnetic, it is reasonable to assume that $J_{\mathrm{Cr-Cd}} = 0$. The energy of the lowest-lying states of a given total spin S is approximately given by $E(S) = (2J/N)S(S+1)$ [213].

Single crystal samples were prepared as described previously [199; 206]. The unaligned crystals were mounted on the cold-finger of a dilution refrigerator. The measurements were performed in a longitudinal field applied parallel to the initial muon spin polarization using a superconducting magnet.

Example data are shown in Fig. 6.12. Over the whole range of applied fields $B > 0$ the data were described well by a single exponential relaxation

$$A(t) = A_{\mathrm{rel}} e^{-\lambda t} + A_{\mathrm{nr}}, \tag{6.11}$$

where A_{rel} was held fixed and A_{nr} is a highly field-dependent non-relaxing term. The measured relaxation rate λ is shown in Fig. 6.12. Also shown is the time-integrated asymmetry, corrected approximately for the effect of positron beam optics in applied field by subtracting a straight line.

Despite their different magnetic ground states and level crossings, the data taken on Cr_8Cd and Cr_8Mn resemble each other closely. As the peaks in λ and dips in the corrected asymmetry around 1 T, 2.5 T, and 4 T coincide with the minima in the beam spot size, it is likely that variation in muon beam spot size is the primary cause for the observed features. Unfortunately the second dip in the corrected asymmetry, seen for Cr_8Cd, Cr_8Mn, [Cu(pyz)(gly)](ClO_4), and DIMPY, is located at 2.3 T, the level crossing in Cr_8Cd. The LF measurements on Cr_8Cd were among the first experiments performed on the, then new, HiFi spectrometer and were performed before any of the other LF measurements reported here. Without the detailed understanding of the instrument background — for which all of this LF work has been crucial — this feature was initially misidentified as a direct signature of the level crossing [214].

However, there are some observations that cannot be attributed to the changes in muon beam optics alone. Most importantly the relative size of the first and second peak in λ is different in the two samples, with the peaks being of identical size in Cr_8Mn and of very different size in Cr_8Cd. Previous work has shown that the relaxation mechanism for muons is starkly different in $S = 0$ and $S \neq 0$

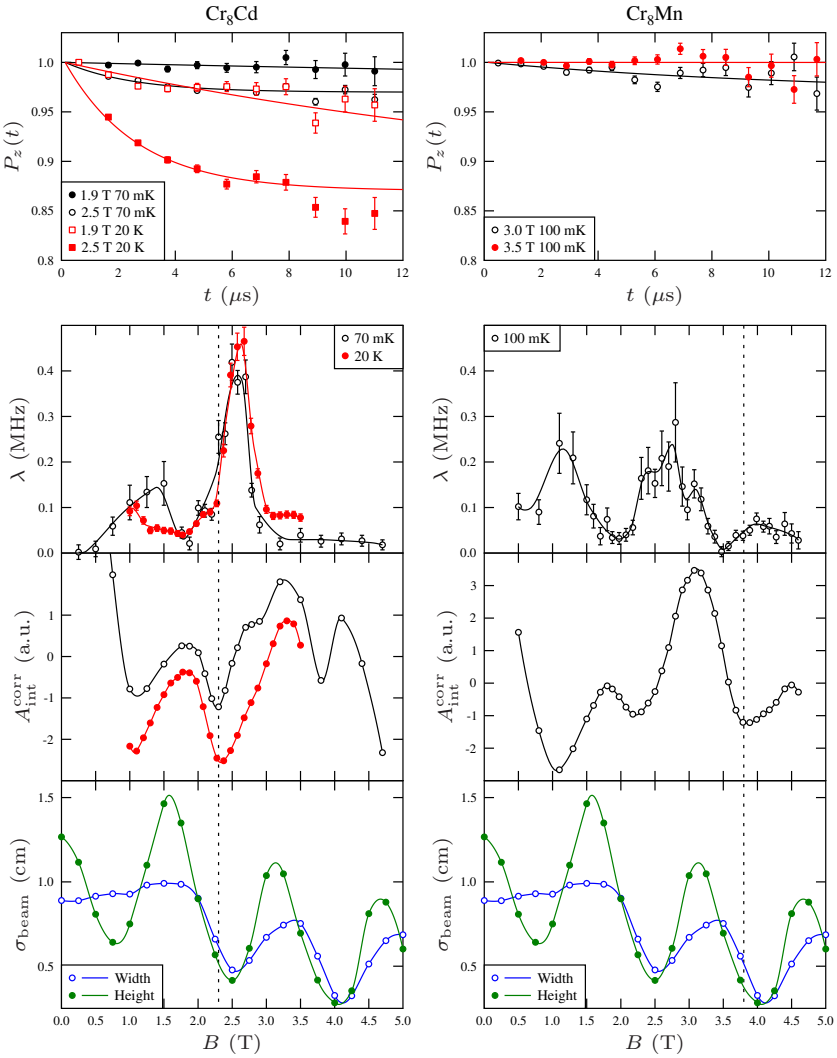

Figure 6.12: LF μ^+SR data for Cr_8Cd (left) and Cr_8Mn (right). From top to bottom: normalised experimental asymmetry, relaxation rate λ versus field, corrected integrated asymmetry, beam width and height adapted from Ref. [182]. Except for the asymmetry, solid lines are a guide to the eye. The dotted line indicates the location of the level crossings [208; 212].

MNMs [215]. Since the magnetic state of Cr_8Mn does not change between these two peaks, this is likely to be an indirect signature of the magnetic state in Cr_8Cd changing substantially between about 1 T and 2.5 T, though it cannot be ruled out that small differences in sample size, shape, and position contribute to this difference (which is supported by the absence of a peak in λ around 4 T in Cr_8Cd, although a dip in the asymmetry is present). Similarly the third peak in Cr_8Mn, located above the level crossing, is smaller than the first two peaks, which may allude to a change in the magnetic state between 2.5 T and 4.0 T.

In conclusion, while the LF μ^+SR signal in the two MNMs Cr_8Cd and Cr_8Mn is dominated by a previously uncharacterised instrument background, LF μ^+SR provides indirect evidence of the magnetic level crossings. The detailed understanding of the instrument background will be crucial for any future LF study on the HiFi instrument.

Bibliography

[1] M. Tamura, Y. Nakazawa, D. Shiomi, K. Nozawa, Y. Hosokoshi, M. Ishikawa, M. Takahashi, and M. Kinoshita, Chem. Phys. Letts. **186**, 401 (1991).

[2] S. J. Blundell and F. L. Pratt, J. Phys. Condens. Matter **16**, R771 (2004).

[3] R. M. Bozorth, H. J. Williams, and D. E. Walsh, Phys. Rev. **103**, 572 (1956).

[4] A. Ito, M. Suenaga, and K. Ono, J. Chem. Phys. **48**, 3597 (1968).

[5] S. Ferlay, T. Mallah, R. Ouahes, P. Veillet, and M. Verdaguer, Nature **378**, 701 (1995).

[6] T. Lancaster, S. J. Blundell, and F. L. Pratt, Physica Scripta **88**, 068506 (2013).

[7] N. D. Mermin and H. Wagner, Phys. Rev. Lett. **17**, 1133 (1966).

[8] P. C. Hohenberg, Phys. Rev. **158**, 383 (1967).

[9] V. Berezinsky, Sov.Phys.JETP **32**, 493 (1971).

[10] V. Berezinsky, Zh. Eksp. Teor. Fiz. **61**, 1144 (1971).

[11] S. Coleman, Comm. Math. Phys. **31**, 259 (1973).

[12] J. M. Kosterlitz and D. J. Thouless, J. Phys. C: Solid State Phys. **5**, L124 (1972).

[13] J. M. Kosterlitz and D. J. Thouless, J. Phys. C: Solid State Phys. **6**, 1181 (1973).

[14] P. Sengupta, C. D. Batista, R. D. McDonald, S. Cox, J. Singleton, L. Huang, T. P. Papageorgiou, O. Ignatchik, T. Herrmannsdörfer, J. L. Manson, *et al.*, Phys. Rev. B **79**, 060409 (2009).

[15] G. E. Volovik, *The Universe in a Helium Droplet* (Oxford University Press, 2003).

[16] N. Romming, C. Hanneken, M. Menzel, J. E. Bickel, B. Wolter, K. von Bergmann, A. Kubetzka, and R. Wiesendanger, Science **341**, 636 (2013).

[17] T. Giamarchi, *Quantum physics in one dimension* (Oxford University Press, 2003).

[18] T. Giamarchi and A. M. Tsvelik, Phys. Rev. B **59**, 11398 (1999).

[19] S. Sachdev, *Quantum phase transitions* (Cambridge University Press, 1999).

[20] T. Sakai and M. Takahashi, Phys. Rev. B **42**, 4537 (1990).

[21] A. Altland and B. D. Simons, *Condensed Matter Field Theory* (Cambridge University Press, 2010).

[22] F. Haldane, Phys. Lett. **93**, 464 (1983).

[23] F. D. M. Haldane, Phys. Rev. Lett. **50**, 1153 (1983).

[24] P. A. Lee, N. Nagaosa, and X.-G. Wen, Rev. Mod. Phys. **78**, 17 (2006).

[25] E. Manousakis, Rev. Mod. Phys. **63**, 1 (1991).

[26] J. A. Hertz, Phys. Rev. B **14**, 1165 (1976).

[27] P. Coleman and A. J. Schofield, Nature **433**, 226 (2005).

[28] L. Balents, Nature **464**, 199 (2010).

[29] C. Rüegg, K. Kiefer, B. Thielemann, D. F. McMorrow, V. Zapf, B. Normand, M. B. Zvonarev, P. Bouillot, C. Kollath, T. Giamarchi, *et al.*, Phys. Rev. Lett. **101**, 247202 (2008).

[30] E. Dagotto and T. M. Rice, Science **271**, 618 (1996).

[31] T. Giamarchi, C. Ruegg, and O. Tchernyshyov, Nature Phys. **4**, 198 (2008).

[32] A. Ardavan, O. Rival, J. J. L. Morton, S. J. Blundell, A. M. Tyryshkin, G. A. Timco, and R. E. P. Winpenny, Phys. Rev. Lett. **98**, 057201 (2007).

[33] F. L. Pratt, P. J. Baker, S. J. Blundell, T. Lancaster, S. Ohira-Kawamura, C. Baines, Y. Shimizu, K. Kanoda, I. Watanabe, and G. Saito, Nature **471**, 612 (2011).

[34] F. Zhang, Tech. Rep., iHS iSuppli Storage Space Market Brief (2013), URL `www.isuppli.com/memory-and-storage/news/pages/hard-disk-drive-market-revenue-set-for-double-digit-decline-this-year.aspx`.

[35] A. A. Penzias and R. W. Wilson, Astrophys. J. **142**, 419 (1965).

[36] B. Rosenberg, L. van Camp, and T. Krigas, Nature **205**, 698 (1965).

[37] C. S. Wu, E. Ambler, R. W. Hayward, D. D. Hoppes, and R. P. Hudson, Phys. Rev. **105**, 1413 (1957).

[38] D. Lindorff, *Pauli and Jung: The Meeting of Two Great Minds* (Quest Books, 2004).

[39] R. L. Garwin, L. M. Lederman, and M. Weinrich, Phys. Rev. **105**, 1415 (1957).

[40] J. Beringer, J. F. Arguin, R. M. Barnett, K. Copic, O. Dahl, D. E. Groom, C. J. Lin, J. Lys, H. Murayama, C. G. Wohl, *et al.* (Particle Data Group), Phys. Rev. D **86**, 010001 (2012).

[41] *2010 codata recommended values*, URL `http://physics.nist.gov`.

[42] ISIS Facility, *Emu user guide*, URL `http://www.isis.stfc.ac.uk/instruments/emu/documents/mcs-manual6627.pdf`.

[43] V. Storchak, S. F. J. Cox, S. P. Cottrell, J. H. Brewer, G. D. Morris, D. J. Arseneau, and B. Hitti, Phys. Rev. Lett. **78**, 2835 (1997).

[44] T. Prokscha, E. Morenzoni, D. G. Eshchenko, N. Garifianov, H. Glückler, R. Khasanov, H. Luetkens, and A. Suter, Phys. Rev. Lett. **98**, 227401 (2007).

[45] G. Eaton and S. Kilcoyne, in *Muon Science: Muons In Physics, Chemistry and Materials*, edited by Lee, SL and Kilcoyne, SH and Cywinski, R (1999), vol. 51 of *SUSSP PROCEEDINGS*, pp. 11–37.

[46] B. D. Patterson, Rev. Mod. Phys. **60**, 69 (1988).

[47] J. Chappert, *Muons and pions in Materials Research* (Amsterdam: Elsevier, 1984).

[48] A. Yaouanc and P. D. D. Réotier, *Muon Rotation, Relaxation, and Resonance* (Oxford University Press, 2011).

[49] T. Lancaster, D.Phil. thesis, University of Oxford (2004).

[50] ISIS Facility, *Hifi user guide*, URL `http://www.isis.stfc.ac.uk/instruments/hifi/documents/hifi-instrument-manual12522.pdf`.

[51] P. D. de Reotier and A. Yaouanc, J. Phys. Condens. Matter **9**, 9113 (1997).

[52] S. F. J. Cox, J. Phys. C: Solid State Phys. **20**, 3187 (1987).

[53] S. F. J. Cox, Rep. Prog. Phys. **72**, 116501 (2009).

[54] S. F. J. Cox, J. Phys. Condens. Matter **15**, R1727 (2003).

[55] J. M. Gil, H. V. Alberto, R. C. Vilão, J. Piroto Duarte, P. J. Mendes, L. P. Ferreira, N. Ayres de Campos, A. Weidinger, J. Krauser, C. Niedermayer, *et al.*, Phys. Rev. Lett. **83**, 5294 (1999).

[56] S. F. J. Cox, E. A. Davis, S. P. Cottrell, P. J. C. King, J. S. Lord, J. M. Gil, H. V. Alberto, R. C. Vilão, J. Piroto Duarte, N. Ayres de Campos, *et al.*, Phys. Rev. Lett. **86**, 2601 (2001).

[57] A. Abragam, *Principles of nuclear magnetism* (Oxford University Press, 1961).

[58] R. Kubo and T. Toyabe, in *Magnetic Resonance and Relaxation*, edited by R. Blinc (North Holland, 1967).

[59] R. S. Hayano, Y. J. Uemura, J. Imazato, N. Nishida, T. Yamazaki, and R. Kubo, Phys. Rev. B **20**, 850 (1979).

[60] J. J. Sakurai, *Modern Quantum Mechanics* (Addison-Wesley, 1994).

[61] P. J. Baker, J. S. Möller, F. L. Pratt, W. Hayes, S. J. Blundell, T. Lancaster, T. F. Qi, and G. Cao, Phys. Rev. B **87**, 180409 (2013).

[62] P. Sengupta, A. W. Sandvik, and R. R. P. Singh, Phys. Rev. B **68**, 094423 (2003).

[63] T. Lancaster, S. J. Blundell, M. L. Brooks, P. J. Baker, F. L. Pratt, J. L. Manson, C. P. Landee, and C. Baines, Phys. Rev. B **73**, 020410 (2006).

[64] G. Mennenga, L. de Jongh, W. Huiskamp, and J. Reedijk, J. Magn. Magn. Mater. **44**, 89 (1984).

[65] Y. J. Uemura, G. M. Luke, B. J. Sternlieb, J. H. Brewer, J. F. Carolan, W. N. Hardy, R. Kadono, J. R. Kempton, R. F. Kiefl, S. R. Kreitzman, *et al.*, Phys. Rev. Lett. **62**, 2317 (1989).

[66] J. D. Wright, T. Lancaster, I. Franke, A. J. Steele, J. S. Möller, M. J. Pitcher, A. J. Corkett, D. R. Parker, D. G. Free, F. L. Pratt, *et al.*, Phys. Rev. B **85**, 054503 (2012).

[67] T. Lancaster, S. R. Giblin, G. Allodi, S. Bordignon, M. Mazzani, R. D. Renzi, P. G. Freeman, P. J. Baker, F. L. Pratt, P. Babkevich, *et al.*, arxiv:1301.5124 (2013).

[68] W. Kohn, Rev. Mod. Phys. **71**, 1253 (1999).

[69] R. M. Martin, *Electronic structure* (Cambridge University Press, 2004).

[70] H. M. James and A. S. Coolidge, J. Chem. Phys. **1**, 825 (1933).

[71] P. Hohenberg and W. Kohn, Phys. Rev. **136**, B864 (1964).

[72] W. Kohn and L. J. Sham, Phys. Rev. **140**, A1133 (1965).

[73] D. M. Ceperley and B. J. Alder, Phys. Rev. Lett. **45**, 566 (1980).

[74] J. P. Perdew, K. Burke, and M. Ernzerhof, Phys. Rev. Lett. **77**, 3865 (1996).

[75] A. D. Becke, Phys. Rev. A **38**, 3098 (1988).

[76] C. Lee, W. Yang, and R. G. Parr, Phys. Rev. B **37**, 785 (1988).

[77] H. Hellmann, *Einführung in die Quantenchemie* (Deutike, Leipzig, 1937).

[78] R. P. Feynman, Phys. Rev. **56**, 340 (1939).

[79] S. Baroni, S. de Gironcoli, A. Dal Corso, and P. Giannozzi, Rev. Mod. Phys. **73**, 515 (2001).

[80] H. J. Monkhorst and J. D. Pack, Phys. Rev. B **13**, 5188 (1976).

[81] D. R. Hamann, M. Schlüter, and C. Chiang, Phys. Rev. Lett. **43**, 1494 (1979).

[82] D. Vanderbilt, Phys. Rev. B **41**, 7892 (1990).

[83] P. E. Blöchl, Phys. Rev. B **50**, 17953 (1994).

[84] C. J. Pickard and F. Mauri, Phys. Rev. B **63**, 245101 (2001).

[85] P. Giannozzi *et al.*, J. Phys.: Condens. Matter **21**, 395502 (2009).

[86] J. S. Möller, D. Ceresoli, T. Lancaster, N. Marzari, and S. J. Blundell, Phys. Rev. B **87**, 121108 (2013).

[87] J. S. Möller, P. Bonfà, D. Ceresoli, F. Bernardini, S. J. Blundell, T. Lancaster, R. D. Renzi, N. Marzari, I. Watanabe, S. Sulaiman, *et al.*, Physica Scripta **88**, 068510 (2013).

[88] K. Kojima, A. Keren, G. M. Luke, B. Nachumi, W. D. Wu, Y. J. Uemura, M. Azuma, and M. Takano, Phys. Rev. Lett. **74**, 2812 (1995).

[89] S. J. Blundell, F. L. Pratt, P. A. Pattenden, M. Kurmoo, K. H. Chow, S. Takagi, T. Jestädt, and W. Hayes, J. Phys.: Condens. Matter **9**, L119 (1997).

[90] E. Amit and A. Keren, Phys. Rev. B **82**, 172509 (2010).

[91] G. M. Luke *et al.*, Phys. Rev. B **42**, 7981 (1990).

[92] R. De Renzi, G. Guidi, P. Podini, R. Tedeschi, C. Bucci, and S. F. J. Cox, Phys. Rev. B **30**, 186 (1984).

[93] R. F. Kiefl, M. Celio, T. L. Estle, S. R. Kreitzman, G. M. Luke, T. M. Riseman, and E. J. Ansaldo, Phys. Rev. Lett. **60**, 224 (1988).

[94] J. Brewer, R. Kiefl, J. Carolan, P. Dosanjh, W. Hardy, S. Kreitzman, Q. Li, T. Riseman, P. Schleger, H. Zhou, *et al.*, Hyperfine Interact. **63**, 177 (1991). 10.1007/BF02396001.

[95] M. Camani, F. N. Gygax, W. Rüegg, A. Schenck, and H. Schilling, Phys. Rev. Lett. **39**, 836 (1977).

[96] K. Chow, R. Lichti, R. Kiefl, S. Dunsiger, T. Estle, B. Hitti, R. Kadono, W. MacFarlane, J. Schneider, D. Schumann, *et al.*, Phys. Rev. B **50**, 8918 (1994).

[97] J. H. Brewer, S. R. Kreitzman, D. R. Noakes, E. J. Ansaldo, D. R. Harshman, and R. Keitel, Phys. Rev. B **33**, 7813 (1986).

[98] T. Lancaster, S. J. Blundell, P. J. Baker, M. L. Brooks, W. Hayes, F. L. Pratt, J. L. Manson, M. M. Conner, and J. A. Schlueter, Phys. Rev. Lett. **99**, 267601 (2007).

[99] C. G. Van de Walle, Phys. Rev. Lett. **64**, 669 (1990).

[100] C. G. Van de Walle, P. J. H. Denteneer, Y. Bar-Yam, and S. T. Pantelides, Phys. Rev. B **39**, 10791 (1989).

[101] C. G. Van de Walle, Phys. Rev. Lett. **85**, 1012 (2000).

[102] R. Ramírez and C. P. Herrero, Phys. Rev. Lett. **73**, 126 (1994).

[103] R. H. Luchsinger, Y. Zhou, and P. F. Meier, Phys. Rev. B **55**, 6927 (1997).

[104] T. Miyake, T. Ogitsu, and S. Tsuneyuki, Phys. Rev. Lett. **81**, 1873 (1998).

[105] A. R. Porter, M. D. Towler, and R. J. Needs, Phys. Rev. B **60**, 13534 (1999).

[106] T. Miyake, T. Ogitsu, and S. Tsuneyuki, Phys. Rev. B **60**, 14197 (1999).

[107] C. P. Herrero and R. Ramírez, Phys. Rev. Lett. **99**, 205504 (2007).

[108] I. McKenzie, J.-C. Brodovitch, P. W. Percival, T. Ramnial, and J. A. C. Clyburne, J. Am. Chem. Soc. **125**, 11565 (2003).

[109] E. Roduner and H. Fischer, Chem. Phys. **54**, 261 (1981).

[110] R. De Renzi, G. Guidi, P. Podini, R. Tedeschi, C. Bucci, and S. F. J. Cox, Phys. Rev. B **30**, 197 (1984).

[111] J. S. Möller, *jfit: a general purpose fitting program in the Matlab® programming language.*

[112] W. Jauch, M. Reehuis, and A. J. Schultz, Acta Crystallogr A **60**, 51 (2004).

[113] J. Strempfer, U. Rütt, S. P. Bayrakci, T. Brückel, and W. Jauch, Phys. Rev. B **69**, 014417 (2004).

[114] P. Dufek, P. Blaha, V. Sliwko, and K. Schwarz, Phys. Rev. B **49**, 10170 (1994).

[115] S. J. Blundell, J. S. Möller, T. Lancaster, P. J. Baker, F. L. Pratt, G. Seber, and P. M. Lahti, Phys. Rev. B **88**, 064423 (2013).

[116] K. Kawaguchi and E. Hirota, J. Chem. Phys. **87**, 6838 (1987).

[117] R. D. Hunt and L. Andrews, J. Chem. Phys. **87**, 6819 (1987).

[118] C. Swalina and S. Hammes-Schiffer, J. Phys. Chem. A **109**, 10410 (2005).

[119] W. Hayes and A. M. Stoneham, *Defects and Defect Processes in Nonmetallic Solids* (Dover, New York, 2004).

[120] G. A. Geoffrey, *An Introduction to Hydrogen Bonding* (Oxford University Press, 1997).

[121] P. Atkins, T. Overton, J. Rourke, M. Well, and F. Armstrong, *Inorganic chemistry* (Oxford University Press, 2010).

[122] G. D. Carney and R. N. Porter, J. Chem. Phys. **65**, 3547 (1976).

[123] A. Kerridge, A. H. Harker, and A. M. Stoneham, J. Phys. Condens. Matter **16**, 8743 (2004).

[124] D. Marx and M. Parrinello, J. Chem. Phys. **104**, 4077 (1996).

[125] M. Ceriotti, G. Bussi, and M. Parrinello, Phys. Rev. Lett. **103**, 030603 (2009).

[126] F. Bernardini, P. Bonfà, S. Massidda, and R. De Renzi, Phys. Rev. B **87**, 115148 (2013).

[127] H. Baumeler *et al.*, Hyperfine Interact. **32**, 659 (1986).

[128] T. Kamikawa, Phys. Status Solidi B **99**, 721 (1980).

[129] C. Hoentzsch and J. Spaeth, Solid State Commun. **29**, 577 (1979).

[130] R. F. Kiefl, E. Holzschuh, H. Keller, W. Kündig, P. F. Meier, B. D. Patterson, J. W. Schneider, K. W. Blazey, S. L. Rudaz, and A. B. Denison, Phys. Rev. Lett. **53**, 90 (1984).

[131] R. E. Shamu, W. M. Hartmann, and E. L. Yasaitis, Phys. Rev. **170**, 822 (1968).

[132] J. L. Hall and R. T. Schumacher, Phys. Rev. **127**, 1892 (1962).

[133] J. W. Hodby, J. Phys. C: Solid State **2**, 404 (1969).

[134] R. F. Kiefl, G. M. Luke, S. R. Kreitzman, M. Celio, R. Keitel, J. H. Brewer, D. R. Noakes, Y. J. Uemura, A. M. Portis, and V. Jaccarino, Phys. Rev. B **35**, 2079 (1987).

[135] K. Momma and F. Izumi, J. Appl. Crystallogr. **44**, 1272 (2011).

[136] H. Luetkens, M. Stingaciu, Y. G. Pashkevich, K. Conder, E. Pomjakushina, A. A. Gusev, K. V. Lamonova, P. Lemmens, and H.-H. Klauss, Phys. Rev. Lett. **101**, 017601 (2008).

[137] H. Maeter *et al.*, Phys. Rev. B **80**, 094524 (2009).

[138] M. Bendele, A. Ichsanow, Y. Pashkevich, L. Keller, T. Strässle, A. Gusev, E. Pomjakushina, K. Conder, R. Khasanov, and H. Keller, Phys. Rev. B **85**, 064517 (2012).

[139] R. De Renzi *et al.*, Supercond. Sci. Technol. **25**, 084009 (2012).

[140] G. Prando *et al.*, Phys. Rev. B **87**, 064401 (2013).

[141] C. G. Van de Walle and J. Neugebauer, Nature **423**, 626 (2003).

[142] R. F. Kiefl, R. Kadono, J. H. Brewer, G. M. Luke, H. K. Yen, M. Celio, and E. J. Ansaldo, Phys. Rev. Lett. **62**, 792 (1989).

[143] P. Quémerais, P. McClarty, and R. Moessner, Phys. Rev. Lett. **109**, 127601 (2012).

[144] S. Ghannadzadeh, J. S. Möller, P. A. Goddard, T. Lancaster, F. Xiao, S. J. Blundell, A. Maisuradze, R. Khasanov, J. L. Manson, S. W. Tozer, *et al.*, Phys. Rev. B **87**, 241102 (2013).

[145] R. Khasanov, D. G. Eshchenko, J. Karpinski, S. M. Kazakov, N. D. Zhigadlo, R. Brütsch, D. Gavillet, D. Di Castro, A. Shengelaya, F. La Mattina, *et al.*, Phys. Rev. Lett. **93**, 157004 (2004).

[146] T. Park, F. Ronning, H. Q. Yuan, M. B. Salamon, R. Movshovich, J. L. Sarrao, and J. D. Thompson, Nature **440**, 65 (2006).

[147] H. A. Jahn and E. Teller, Proc. R. Soc. London. Series A - Mathematical and Physical Sciences **161**, 220 (1937).

[148] L. R. Falvello, J. Chem. Soc., Dalton Trans. **23**, 4463 (1997).

[149] P. A. Goddard, J. L. Manson, J. Singleton, I. Franke, T. Lancaster, A. J. Steele, S. J. Blundell, C. Baines, F. L. Pratt, R. D. McDonald, *et al.*, Phys. Rev. Lett. **108**, 077208 (2012).

[150] J. L. Manson, M. M. Conner, J. A. Schlueter, A. C. McConnell, H. I. Southerland, I. Malfant, T. Lancaster, S. J. Blundell, M. L. Brooks, F. L. Pratt, *et al.*, Chem. Mat. **20**, 7408 (2008).

[151] J. L. Musfeldt, Z. Liu, S. Li, J. Kang, C. Lee, P. Jena, J. L. Manson, J. A. Schlueter, G. L. Carr, and M.-H. Whangbo, Inorg. Chem. **50**, 6347 (2011).

[152] P. A. Goddard, J. Singleton, C. Maitland, S. J. Blundell, T. Lancaster, P. J. Baker, R. D. McDonald, S. Cox, P. Sengupta, J. L. Manson, *et al.*, Phys. Rev. B **78**, 052408 (2008).

[153] C. H. Wang, M. D. Lumsden, R. S. Fishman, G. Ehlers, T. Hong, W. Tian, H. Cao, A. Podlesnyak, C. Dunmars, J. A. Schlueter, *et al.*, Phys. Rev. B **86**, 064439 (2012).

[154] G. J. Halder, K. W. Chapman, J. A. Schlueter, and J. L. Manson, Angew. Chem. Int. Ed. **50**, 419 (2011).

[155] A. Prescimone, C. Morien, D. Allan, J. A. Schlueter, S. W. Tozer, J. L. Manson, S. Parsons, E. K. Brechin, and S. Hill, Angew. Chem. Int. Ed. **51**, 7490 (2012).

[156] F. Xiao, F. M. Woodward, C. P. Landee, M. M. Turnbull, C. Mielke, N. Harrison, T. Lancaster, S. J. Blundell, P. J. Baker, P. Babkevich, *et al.*, Phys. Rev. B **79**, 134412 (2009).

[157] C. Gatti and P. Fantucci, J. Phys. Chem. **97**, 11677 (1993).

[158] J. Meister and W. H. E. Schwarz, J. Phys. Chem. **98**, 8245 (1994).

[159] F. Pratt, Physica B: Condensed Matter **289–290**, 710 (2000).

[160] M. D. Lumsden, S. E. Nagler, B. C. Sales, D. A. Tennant, D. F. McMorrow, S.-H. Lee, and S. Park, Phys. Rev. B **74**, 214424 (2006).

[161] N. Tsyrulin, T. Pardini, R. R. P. Singh, F. Xiao, P. Link, A. Schneidewind, A. Hiess, C. P. Landee, M. M. Turnbull, and M. Kenzelmann, Phys. Rev. Lett. **102**, 197201 (2009).

[162] N. Tsyrulin, F. Xiao, A. Schneidewind, P. Link, H. M. Rønnow, J. Gavilano, C. P. Landee, M. M. Turnbull, and M. Kenzelmann, Phys. Rev. B **81**, 134409 (2010).

[163] A. J. Steele, T. Lancaster, S. J. Blundell, P. J. Baker, F. L. Pratt, C. Baines, M. M. Conner, H. I. Southerland, J. L. Manson, and J. A. Schlueter, Phys. Rev. B **84**, 064412 (2011).

[164] Y. Uemura and G. Luke, Physica B: Condensed Matter **186–188**, 223 (1993).

[165] L. P. Le, A. Keren, G. M. Luke, B. J. Sternlieb, W. D. Wu, Y. J. Uemura, J. H. Brewer, T. M. Riseman, R. V. Upasani, L. Y. Chiang, *et al.*, Phys. Rev. B **48**, 7284 (1993).

[166] J. Major, J. Mundy, M. Schmolz, A. Seeger, K.-P. Döring, K. Fürderer, M. Gladisch, D. Herlach, and G. Majer, Hyperfine Interact. **31**, 259 (1986).

[167] A. Amato, Rev. Mod. Phys. **69**, 1119 (1997).

[168] P. A. Goddard, J. Singleton, P. Sengupta, R. D. McDonald, T. Lancaster, S. J. Blundell, F. L. Pratt, S. Cox, N. Harrison, J. L. Manson, *et al.*, New. J. Phys. **10**, 083025 (2008).

[169] C. Yasuda, S. Todo, K. Hukushima, F. Alet, M. Keller, M. Troyer, and H. Takayama, Phys. Rev. Lett. **94**, 217201 (2005).

[170] M. Kurmoo, Chem. Mat. **11**, 3370 (1999).

[171] H. J. Schulz, Phys. Rev. Lett. **77**, 2790 (1996).

[172] C. Pfleiderer, J. Phys. Condens. Matter **17**, S987 (2005).

[173] M. B. Stone, I. Zaliznyak, D. H. Reich, and C. Broholm, Phys. Rev. B **64**, 144405 (2001).

[174] T. Hong, C. Stock, I. Cabrera, C. Broholm, Y. Qiu, J. B. Leao, S. J. Poulton, and J. R. D. Copley, Phys. Rev. B **82**, 184424 (2010).

[175] T. Lancaster, P. A. Goddard, S. J. Blundell, F. R. Foronda, S. Ghannadzadeh, J. S. Möller, P. J. Baker, F. L. Pratt, C. Baines, L. Huang, *et al.*, arXiv: 1311.7614.

[176] D. C. Johnston, R. K. Kremer, M. Troyer, X. Wang, A. Klümper, S. L. Bud'ko, A. F. Panchula, and P. C. Canfield, Phys. Rev. B **61**, 9558 (2000).

[177] A. Keren, L. P. Le, G. M. Luke, B. J. Sternlieb, W. D. Wu, Y. J. Uemura, S. Tajima, and S. Uchida, Phys. Rev. B **48**, 12926 (1993).

[178] T. Ami, M. K. Crawford, R. L. Harlow, Z. R. Wang, D. C. Johnston, Q. Huang, and R. W. Erwin, Phys. Rev. B **51**, 5994 (1995).

[179] F. L. Pratt, S. J. Blundell, T. Lancaster, C. Baines, and S. Takagi, Phys. Rev. Lett. **96**, 247203 (2006).

[180] B. Bleaney and K. D. Bowers, Proc. R. Soc. London. Series A. Mathematical and Physical Sciences **214**, 451 (1952).

[181] B. S. Conner, H. D. Zhou, Y. J. Jo, L. Balicas, C. R. Wiebe, J. P. Carlo, Y. J. Uemura, A. A. Aczel, T. J. Williams, and G. M. Luke, Phys. Rev. B **81**, 132401 (2010).

[182] J. S. Lord, I. McKenzie, P. J. Baker, S. J. Blundell, S. P. Cottrell, S. R. Giblin, J. Good, A. D. Hillier, B. H. Holsman, P. J. C. King, *et al.*, Review of Scientific Instruments **82**, 073904 (2011).

[183] S. Ghannadzadeh, M. Coak, I. Franke, P. A. Goddard, J. Singleton, and J. L. Manson, Rev. Sci. Instrum. **82**, 113902 (2011).

[184] M. Tachiki and T. Yamada, J. Phys. Soc. Japan **28**, 1413 (1970).

[185] M. Azuma, Z. Hiroi, M. Takano, K. Ishida, and Y. Kitaoka, Phys. Rev. Lett. **73**, 3463 (1994).

[186] M. Klanjšek, H. Mayaffre, C. Berthier, M. Horvatić, B. Chiari, O. Piovesana, P. Bouillot, C. Kollath, E. Orignac, R. Citro, *et al.*, Phys. Rev. Lett. **101**, 137207 (2008).

[187] B. Thielemann, C. Rüegg, K. Kiefer, H. M. Rønnow, B. Normand, P. Bouillot, C. Kollath, E. Orignac, R. Citro, T. Giamarchi, *et al.*, Phys. Rev. B **79**, 020408 (2009).

[188] B. Thielemann, C. Rüegg, H. M. Rønnow, A. M. Läuchli, J.-S. Caux, B. Normand, D. Biner, K. W. Krämer, H.-U. Güdel, J. Stahn, *et al.*, Phys. Rev. Lett. **102**, 107204 (2009).

[189] A. Shapiro, C. P. Landee, M. M. Turnbull, J. Jornet, M. Deumal, J. J. Novoa, M. A. Robb, and W. Lewis, J. Am. Chem. Soc. **129**, 952 (2007).

[190] P. W. Anderson, Science **235**, 1196 (1987).

[191] T. Hong *et al.*, Phys. Rev. Lett. **105**, 137207 (2010).

[192] K. Ninios, T. Hong, T. Manabe, C. Hotta, S. N. Herringer, M. M. Turnbull, C. P. Landee, Y. Takano, and H. B. Chan, Phys. Rev. Lett. **108**, 097201 (2012).

[193] D. Schmidiger, P. Bouillot, S. Mühlbauer, S. Gvasaliya, C. Kollath, T. Giamarchi, and A. Zheludev, Phys. Rev. Lett. **108**, 167201 (2012).

[194] J. L. White, C. Lee, O. Günaydin-Şen, L. C. Tung, H. M. Christen, Y. J. Wang, M. M. Turnbull, C. P. Landee, R. D. McDonald, S. A. Crooker, *et al.*, Phys. Rev. B **81**, 052407 (2010).

[195] D. Schmidiger, S. Mühlbauer, A. Zheludev, P. Bouillot, T. Giamarchi, C. Kollath, G. Ehlers, and A. M. Tsvelik, Phys. Rev. B **88**, 094411 (2013).

[196] D. Schmidiger, P. Bouillot, T. Guidi, R. Bewley, C. Kollath, T. Giamarchi, and A. Zheludev, Phys. Rev. Lett. **111**, 107202 (2013).

[197] M. Jeong, H. Mayaffre, C. Berthier, D. Schmidiger, A. Zheludev, and M. Horvatić, Phys. Rev. Lett. **111**, 106404 (2013).

[198] D. Gatteschi, R. Sessoli, and J. Villain, *Molecular Nanomagnets* (Oxford University Press, 2006).

[199] O. Cador, D. Gatteschi, R. Sessoli, F. K. Larsen, J. Overgaard, A.-L. Barra, S. J. Teat, G. A. Timco, and R. E. P. Winpenny, Angew. Chem. Int. Ed. **43**, 5196 (2004).

[200] T. Lancaster, S. J. Blundell, F. L. Pratt, M. L. Brooks, J. L. Manson, E. K. Brechin, C. Cadiou, D. Low, E. J. L. McInnes, and R. E. P. Winpenny, J. Phys. Condens. Matter **16**, S4563 (2004).

[201] M. J. Graf, J. Lago, A. Lascialfari, A. Amato, C. Baines, S. R. Giblin, J. S. Lord, A. M. Tkachuk, and B. Barbara, Phys. Rev. Lett. **99**, 267203 (2007).

[202] M. Corti, M. Filibian, P. Carretta, L. Zhao, and L. K. Thompson, Phys. Rev. B **72**, 064402 (2005).

[203] K. L. Taft, C. D. Delfs, G. C. Papaefthymiou, S. Foner, D. Gatteschi, and S. J. Lippard, J. Am. Chem. Soc. **116**, 823 (1994).

[204] J. R. Friedman, M. P. Sarachik, J. Tejada, and R. Ziolo, Phys. Rev. Lett. **76**, 3830 (1996).

[205] L. Thomas, F. Lionti, R. Ballou, D. Gatteschi, R. Sessoli, and B. Barbara, Nature **383**, 145 (1996).

[206] G. A. Timco, A. S. Batsanov, F. K. Larsen, C. A. Muryn, J. Overgaard, S. J. Teat, and R. E. P. Winpenny, Chem. Commun. pp. 3649–3651 (2005),

[207] J. van Slageren, R. Sessoli, D. Gatteschi, A. A. Smith, M. Helliwell, R. E. P. Winpenny, A. Cornia, A.-L. Barra, A. G. M. Jansen, E. Rentschler, *et al.*, Chem. Eur. J. **8**, 277 (2002).

[208] Y. Furukawa, K. Kiuchi, K.-i. Kumagai, Y. Ajiro, Y. Narumi, M. Iwaki, K. Kindo, A. Bianchi, S. Carretta, G. A. Timco, *et al.*, Phys. Rev. B **78**, 092402 (2008).

[209] O. Cador, D. Gatteschi, R. Sessoli, A.-L. Barra, G. A. Timco, and R. E. Winpenny, Journal of Magnetism and Magnetic Materials **290-291**, 55 (2005). Proceedings of the Joint European Magnetic Symposia (JEMS' 04).

[210] Y. Furukawa, K. Kiuchi, K.-i. Kumagai, Y. Ajiro, Y. Narumi, M. Iwaki, K. Kindo, A. Bianchi, S. Carretta, P. Santini, *et al.*, Phys. Rev. B **79**, 134416 (2009).

[211] M. L. Baker, O. Waldmann, S. Piligkos, R. Bircher, O. Cador, S. Carretta, D. Collison, F. Fernandez-Alonso, E. J. L. McInnes, H. Mutka, *et al.*, Phys. Rev. B **86**, 064405 (2012).

[212] M. L. Baker *et al.*, in preparation.

[213] J. Schnack and M. Luban, Phys. Rev. B **63**, 014418 (2000).

[214] T. Lancaster, J. S. Möller, S. J. Blundell, F. L. Pratt, P. J. Baker, T. Guidi, G. A. Timco, and R. E. P. Winpenny, J. Phys. Condens. Matter **23**, 242201 (2011).

[215] T. Lancaster, S. J. Blundell, F. L. Pratt, I. Franke, A. J. Steele, P. J. Baker, Z. Salman, C. Baines, I. Watanabe, S. Carretta, *et al.*, Phys. Rev. B **81**, 140409 (2010).

List of publications

- J. S. Möller, P. Bonfá, D. Ceresoli, F. Bernardini, S. J. Blundell, T. Lancaster, R. De Renzi, N. Marzari, I. Watanabe, S. Sulaiman, and M. I. Mohamed-Ibrahim, *Playing quantum hide-and-seek with the muon: localizing muon stopping sites*, Physica Scripta **88**, 68510 (2013).

- F. Xiao , T. Lancaster, P. J. Baker, F. L. Pratt, S. J. Blundell, J. S. Möller, N. Z. Ali, M. Jansen *Magnetic transition and spin dynamics in the triangular Heisenberg antiferromagnet* α*-*$KCrO_2$, Phys. Rev. B **88**, 180401 (2013).

- S. J. Blundell, J. S. Möller, T. Lancaster, P. J. Baker, F. L. Pratt, G. Seber, and P. M. Lahti, μ^+*SR study of magnetic order in the organic quasi-one-dimensional ferromagnet F4BImNN*, Phys. Rev. B **88**, 064423 (2013).

- S. Ghannadzadeh, J. S. Möller, P. A. Goddard, T. Lancaster, F. Xiao, S. J. Blundell, A. Maisuradze, R. Khasanov, J. L. Manson, S. W. Tozer, D. Graf, and J. A. Schlueter, *Evolution of magnetic interactions in a pressure-induced Jahn-Teller driven magnetic dimensionality switch*, Phys. Rev. B **87**, 241102(R) (2013).

- P. J. Baker, J. S. Möller, F. L. Pratt, W. Hayes, S. J. Blundell, T. Lancaster, T. F. Qi, and G. Cao, *Weak magnetic transitions in pyrochlore* $Bi_2Ir_2O_7$, Phys. Rev. B **87**, 180409(R) (2013).

- J. S. Möller, D. Ceresoli, T. Lancaster, N. Marzari, and S. J. Blundell, *Quantum states of muons in fluorides*, Phys. Rev. B **87**, 121108(R) (2013).

- S. H. Lapidus, J. L. Manson, H. Park, A. J. Clement, S. Ghannadzadeh, P. Goddard, T. Lancaster, J. S. Möller, S. J. Blundell, M. T. F. Telling, J. Kang, M.-H. Whangbo, and J. A. Schlueter, *Antiferromagnetic ordering through a hydrogen-bonded network in the molecular solid* $CuF_2(H_2O)_2$*(3-chloropyridine)*, Chem. Commun. **49**, 499 (2013).

- J. L. Manson, A. G. Baldwin, B. L. Scott, J. Bendix, R. E. Del Sesto, P. A. Goddard, Y. Kohama, H. E. Tran, S. Ghannadzadeh, J. Singleton, T. Lancaster, J. S. Möller, S. J. Blundell, F. L. Pratt, V. S. Zapf, J. Kang,

C. Lee, M.H. Whangbo, and C. Baines, *[Ni(HF_2)(3-Clpy)$_4$]BF_4 (py = pyridine): Evidence for Spin Exchange Along Strongly Distorted F$\cdots$H$\cdots$F$^-$ Bridges in a One-Dimensional Polymeric Chain*, Inorg. Chem. **51**, 7520 (2012).

- J. L. Manson, K. E. Carreiro, S. H. Lapidus, P. W. Stephens, P. A. Goddard, R. E. Del Sesto, J. Bendix, S. Ghannadzadeh, I. Franke, J. Singleton, T. Lancaster, J. S. Möller, P. J. Baker, F. L. Pratt, S. J. Blundell, J. Kang, C. Lee, and M.H. Whangbo, *Influence of HF_2^- geometry on magnetic interactions elucidated from polymorphs of the metal-organic framework [Ni(HF_2)(pyz)$_2$]PF_6 (pyz = pyrazine)*, Dalton Trans. **41**, 7235 (2012).

- J. D. Wright, T. Lancaster, I. Franke, A. J. Steele, J. S. Möller, M. J. Pitcher, A. J. Corkett, D. R. Parker, D. G. Free, F. L. Pratt, P. J. Baker, S. J. Clarke, and S. J. Blundell, *Gradual destruction of magnetism in the superconducting family $NaFe_{1-x}Co_xAs$*, Phys. Rev. B **85**, 054503 (2012).

- T. Lancaster, J. S. Möller, S. J. Blundell, F. L. Pratt, P. J. Baker, T. Guidi, G. A. Timco, and R. E. P. Winpenny, *Observation of a level crossing in a molecular nanomagnet using implanted muons*, J. Phys. Condens. Matter **23**, 242201 (2011).